NOTE TO USERS

Rotational dynamics of Mars

Using magnetic anomalies modeling to estimate Mars polar motion

Daniel Boutin

Departement of earth and Planetary Sciences
McGill University , Montreal, Canada

October 2004

A thesis submitted to the faculty of Graduate Studies and Research in partial fulfilment of the requirements of the degree of Master of Science

Your file Votre référence
ISBN: 0-494-12405-9
Our file Notre référence
ISBN: 0-494-12405-9

Abstract

The possible polar wandering of the planet Mars is investigated by modeling some of the many surface magnetic anomalies discovered by Mars Global Surveyor (MGS). First I describe the physics of polar wandering by exposing the theory developed by *Ricard et al.* [1993] and *Spada et al.* [1996]. I derive the linear form of the equation of polar motion in the time domain valid for polar motion of up to 10 deg. The long-term polar motion of a non-rigid planet is also discussed via the rotational number first defined by *Spada et al.* [1996]. It is found that the theory is mathematically correct but that the *Ricard et al.* [1993] formulation used to get to the long-term interpretation of the rotational number is unnecessary and add to the complexity of an already difficult subject. The main conclusion of *Spada et al.* [1996] can be reached by using the simpler linear equation of polar motion. The physics behind polar motion hints that Mars has probably undergone polar motion because of the many important topographical loads on its surface.

The modeling of nine isolated magnetic anomalies by two different methods shows that none of the paleomagnetic pole positions found correspond to the actual rotation axis. Moreover, clustering of the poles in the Tharsis region and core field reversal are supported by the results. This is consistent with results obtained in other studies by using different methods. Clustering, however is not as tight as the one found in *Arkani-Hamed* [2001]. The actual pole position found for most anomalies changes according to the method employed and must be considered as preliminary until an accepted way of removing external and nearby sources contamination is found and tested on synthetic data. One anomaly, A5, yields about the same paleomagnetic pole position in the two studies indicating that this anomaly may be better isolated than the rest. The paleomagnetic pole position found for A5 indicate that Mars has probably undergone polar motion of up to 40 deg and that Tharsis is probably responsible. This result supports the argument that the actual equatorial location of Tharsis is not a coincidence but is more likely a natural consequence of polar wandering.

Résumé

Cette thèse présente une étude du mouvement des pôles de la planète Mars obtenue par l'analyse et la modélisation de certaines anomalies magnétiques découvertes par Mars Global Surveyor (MGS). Dans un premier temps je présente la théorie de la dynamique de rotation des planètes non rigides développées par *Ricard et al.* [1993] et *Spada et al.* [1996]. Je dérive la forme linéaire de l'équation du mouvement des pôles en fonction du temps valable pour un mouvement d'au plus 10°. Une équation plus générale est aussi présentée à l'aide du nombre de rotation définie par *Spada et al.* [1996]. Les dérivations effectuées montrent que la théorie est mathématiquement correcte mais la façon dont elle est présentée par *Ricard et al.* [1993] introduit des complexités inutiles dans une théorie déjà fort complexe. Le même résultat peut être obtenu à partir de la forme linéaire de l'équation du mouvement. La physique derrière le phénomène du mouvement des pôles suggère que Mars a probablement subie ce phénomène dans le passé due à la présence de nombreux reliefs topographiques à la surface de la planète.

La modélisation des anomalies magnétique isolées a été effectuée de deux façons différentes. Les résultats montrent qu'aucun des anciens pôles déterminés par l'analyse ne correspond au pôle de rotation actuel de la planète. Plus encore, les différents pôles semblent se groupés dans la région de Tharsis. Le regroupement n'est cependant pas aussi fermé que celui déterminé par *Arkani-Hamed* [2001]. Les résultats indiquent également que l'ancien champ magnétique martien a probablement changé d'orientation au cours de son histoire. Les anciens pôles déterminés dans cette étude doivent êtres considérés comme préliminaires tant que l'on aura pas trouvé une méthode acceptable pour éliminer les différentes sources de contamination. Cependant l'anomalie A5 donne approximativement le même pôle lorsque modélisée par les deux méthodes employées dans cette étude. Le pôle déterminé pour cette anomalie indique que Mars a peut-être changé l'orientation de son axe de rotation de 40° et que Tharsis en est probablement responsable. Cette étude supporte la proposition à l'effet que la position équatoriale actuelle de Tharsis est une conséquence du mouvement des pôles de Mars.

Acknowledgements

This thesis would be quite incomplete without mentioning those who, in one way or the other, have helped me make this become a reality. First, I would like to thank my thesis supervisor, professor Jafar Arkani-Hamed for giving me a chance three years ago to work on Mars and develop my knowledge about this fascinating subject. It has been a pleasure to work with someone as dedicated and as interested to planetary science as he is. With him, I have learned a lot more than technical facts about the magnetic field of Mars but also a critical approach to science that I just did not have when I came to him in 2001.

I would also like to thank Professor L.L.A. Vermeesen of the Delft University of Technology in the Netherlands for some important discussions on rotational dynamics and for helping me correct errors in some of the references I used to produce this thesis. Also, my gratitude goes to professor Yanick Ricard of Le laboratoire des Sciences de la Terre in Lyon, France for helping me with some difficult derivations in rotational dynamics. Finally, thanks to Dr. Benoit Langlais of Nasa's Goddard Space Flight Center for providing me with its surface magnetization model.

Last, but certainly not least, I would like to express my deepest gratitude to my family. Louise, Gabrielle and Justine-Emmanuelle, thank you for your patience and understanding. I will be back to Earth very soon !!!!

Daniel Boutin
EPS, McGill
Montreal, Canada

Table of Contents

Abstract (English)..... I
Abstract (French)..... II
Acknowledgements..... III
Table of Contents..... IV
List of Figures..... VII
List of Tables..... IX

Preface..... 1

1. **Rotational dynamics**
   - 1.1 **Introduction**..... 5
     - 1.1.1 TPW on Mars and Past Work..... 8
   - 1.2 **Basic physics of Polar motion**..... 11
     - 1.2.1 Angular momentum of a non-rigid body..... 12
     - 1.2.2 The inertia tensor..... 13
     - 1.2.3 Euler-Liouville equation..... 15
     - 1.2.4 Stability of free rotation..... 17
   - 1.3 **Linear formulation of the Euler-Liouville equation**..... 19
   - 1.4 **Application of the Euler-Liouville equation for a rigid body**..... 24
     - 1.4.1 Rigid body with no surface load..... 24
     - 1.4.2 Rigid body with an instantaneous surface load..... 26
   - 1.5 **Long term polar motion of a deformable body rotation**..... 29
     - 1.5.1 Love number and the Laplace domain..... 29
     - 1.5.2 Fluid and secular Love numbers..... 32
     - 1.5.3 Expressing polar motion in term of Love numbers..... 33
     - 1.5.4 Change in the inertia tensor due to rotational deformation..... 38
     - 1.5.5 Change in the inertia tensor due to surface loading..... 41
   - 1.6 **Quasi-fluid approximation and the rotational number**..... 42
   - 1.7 **Long term limits of the rotational number**..... 47
     - 1.7.1 Ro >> 1..... 47
     - 1.7.2 Ro << 1..... 49
     - 1.7.3 Offset between spin axis and maximum inertia axis..... 50
   - 1.8 **Influence of internal structure parameters**..... 51
     - 1.8.1 Influence of load compensation..... 51
     - 1.8.2 Influence of lithospheric thickness..... 53
     - 1.8.3 Influence of the internal viscosity profile..... 55
     - 1.8.4 Influence of rigidity on polar wandering..... 55

2. **The magnetic field of Mars**
   - 2.1 **Introduction**..... 60

2.2 **The MGS data**..... 62
2.3 **The Martian magnetic field**..... 64
2.4 **Modeling the Martian magnetic field**..... 66

3. Paleomagnetic poles of Mars revisited

3.1 **Abstract**..... 78
3.2 **Introduction**..... 78
3.3 **Paleomagnetic poles of Mars**..... 80
3.4 **Discussion**..... 82
3.5 **Conclusions**..... 86
3.6 **Appendix**..... 87
3.6.1 Spherical coordinate..... 88
3.6.2 Rectangular coordinate..... 89
3.6.3 Modeling..... 90
3.7 **References**..... 92

4: High altitude data modeling

4.1 Introduction..... 103
4.2 Method..... 104
4.3 Quality of the models..... 106
4.4 Validating the method..... 107
4.5 Results and analysis..... 107
4.5.1 A4 and A5: two well isolated anomalies..... 108
4.5.2 A6 and A7, two badly isolated anomalies..... 109

4.6 **Global analysis**..... 109

4.7 **Conclusion**..... 112

5. Conclusion and future research

5.1 **Conclusion**..... 127
5.2 **Suggestions for future research**..... 129
5.2.1 Rotational dynamics..... 129
5.2.2 Magnetic anomalies modeling..... 130

Appendix A: Derivation of the polar motion equation 133

A.1 **The Liouville equation**..... 134
A.2 **Replacing the inertia tensor into the Liouville equation**..... 136
A.3 **Conclusion**..... 139

Appendix B: More on long term polar motion 141

B.1 **Evaluation of the equatorial bulge realignment time**..... 141
B.2 **Long term interpretation of the rotational number from the linear Euler-Liouville equation**..... 143

Appendix C: Supplementary comments on anomaly isolation 147

Appendix D: Magnetic anomalies and topography 155

Appendix E: Magnetic field calculation 156

References..... 163

List of figures

Note: All figures are at the end of their respective chapter.

Chapter 1

Fig 1.1	High resolution view of the topography of the north pole of Mars	57
Fig 1.2	Calculation of the angular momentum of a mass element.....	58
Fig 1.3	Chapter 1 summary. Description of polar motion theory.....	59

Chapter 2

Fig 2.1	Comparison between the magnetic field produced by an elliptical prism, a circular prism and a dipole.....	72
Fig 2.2	Global view of the Martian magnetic field.....	73
Fig 2.3	Example of high altitude data contamination	74
Fig 2.4	External contamination in track data.....	75
Fig 2.5	Numerical experiment with 20 dipole sources.....	76
Fig 2.6	The nine magnetic anomalies used in this study.....	77

Chapter 3

Fig 3.1	Location of the magnetic anomalies and their respective paleomagnetic pole positions.....	96
Fig 3.2	Magnetization vectors of three original elliptical prisms and their equivalent circular models.....	97
Fig 3.3	Altitude of Mars Global Surveyor over anomaly 5.....	98
Fig 3.4	Normalized descending minimum misfit value ε versus the semi-major axis of the source body of anomaly 5.....	99
Fig 3.5	Observed high-altitude magnetic data over anomaly 5 and the model magnetic field at 400 km elevation.....	100
Fig 3.6	Observed low-altitude magnetic data and the model magnetic field along an orbit track passing almost over the center of anomaly 5....	101
Fig 3.7	Paleomagnetic pole positions determined from all models of anomaly 5 with misfit values within 1.5 times the absolute minimum misfit value.....	102

Chapter 4

Fig 4.1	Position of the magnetic anomalies on the surface of Mars.....	118
Fig 4.2	The 13 pole positions of table 2 for anomaly A5 and A6.....	119
Fig 4.3	Comparison between data and model for the Z models of the A5 anomaly.....	120
Fig 4.4	Scatter diagrams of the data and models presented in figure 4.3.....	121
Fig 4.5	Comparison between data and model for the Z models of the A7	

anomaly..... 122
Fig 4.6 Scatter diagrams for the Z models of the A7 anomaly..... 123
Fig 4.7 Pole positions obtained by using all the high altitude radial models obtained in this study..... 124
Fig 4.8 Combined radial component magnetic field of the two test prisms of table 4.3..... 125
Fig 4.9 The 12 high altitude A5 pole positions obtained by using different prisms..... 126

Appendix C

Fig C.1 Global magnetic field at 400 km altitude generated by the *Langlais et al.* [2003] magnetization model 152
Fig C.2 The A5 anomaly according to the *Langlais et al.* [2003] model..... 153
Fig C.3 The A7 anomaly according to the *Langlais et al.* [2003] model..... 154

Appendix D

Fig D.1 High resolution topography..... 155

Appendix E

Fig E.1 Calculation of the z component of the magnetic field of a circular prism..... 162

List of tables

Table 3.1	Major characteristics of small isolated anomalies and their source bodies.	95
Table 4.1	Test results of the space domain algorithm.....	114
Table 4.2	13 paleopoles obtained for anomalies A4 to A7.....	115
Table 4.3	Parameters of the two test prisms.....	116
Table 4.4	Pole positions obtained by modeling the two test prisms of table 4.3 at different altitudes.....	117
Table C.1	Pole positions obtained by modeling data generated by the *Langlais et al.* [2003] surface magnetization model.....	151
Table E.1	Z component of the magnetic field of a circular prism.....	161

Preface

This thesis examine the possibility that the planet Mars has experienced polar wandering based on the analysis and modeling of some of the numerous surface magnetic anomalies observed by Mars Global Surveyor (MGS) since it's orbit inception in 1997. MGS is equipped with an onboard magnetometer and has relayed to Earth a considerable amount of magnetic field measurements taken at both low (100 to 200 km) and high (average 400km) altitudes. MGS has demonstrated conclusively that Mars does not have a global magnetic field and we therefore have a much more direct access to any crustal field that is present at the surface. An ancient core field, now extinct, is probably responsible for the creation of the observed magnetic anomalies.

Polar wandering or polar motion is the ability of a planetary body to move its surface relative to its axis of rotation in response to internal structure changes. On Earth polar wandering has already been recognized as a major contributor to the overall geophysical history of the planet. The fundamental assumption in using magnetic in polar wandering studies is that the dipole core field axis (present or ancient) shows reasonable alignment with the rotational axis and that this alignment is maintained in any shifting of the rotation axis. This is the case for Earth and this fundamental assumption will be retained for Mars. Below, I introduce each chapter of this thesis and give a short description of their content.

Chapter 1 : The physics of polar motion

The understanding of the rotational behavior of a planetary body is a very complex subject and is related to rotational dynamics, the part of mechanic that study the forces that make an object rotate. For a geophysicist the study of rotational dynamics of planets is both a blessing and a curse. A curse because of the incredible mathematical load involved and a blessing because the rotational behavior of a planet is intimately related to it's internal structure. Therefore a study of the rotation of Mars can help in constraining the internal structure of the planet which is poorly known at the time of this writing.

Since rotational dynamics is so important the basic definitions and formulation of rotational dynamics as applied to non-rigid bodies will be presented in chapter 1. I will explain how a body can shift it's surface relative to a fixed axis of rotation giving the impression to an observer on the surface that the axis of rotation (and therefore the poles) are moving on the surface of the planet. First a description of the basic physics involved in polar motion is presented. The simple case of the rotational dynamics of a rigid body is also discussed. Although rigid body theory is inadequate to correctly represent polar motion of an actual non-rigid planet it can be used as a first order approximation to predict general polar motion patterns. Following that, the theory will be used to present a linear formulation of the polar motion equation for non-rigid bodies. This formulation will be adequate for polar motion less than 10^{o}. However, it is likely that on Mars, as on Earth, polar motion has been much larger than 10^{o} and it is highly desirable to have a theory that gives us a long term portrait of polar motion. In order to get a better idea of long term polar motion I will expose the theory developed by *Ricard et al.* [1993] and *Spada et al.* [1996]. I will present the mathematics involved in the theory, derive the most important equations, and discuss the weaknesses and strengths of the theory. I will conclude this chapter by discussing the influence of different internal structure parameters on polar motion. A short description of our knowledge of those parameters for Mars is included.

Chapter 2 : The magnetic field of Mars

In chapter 2 the use of paleomagnetism in polar wandering studies is described and some of the work done for Mars by different investigators is presented. This chapter also includes a discussion of our state of knowledge of the magnetic field of Mars. I present the most important spherical harmonic models of the magnetic field. The different methods used in the modeling of the magnetic field in general and magnetic anomalies in particular are presented and compared. This chapter includes an analysis of the treatment of magnetic data from MGS. This analysis describes the problems associated with working in a noisy magnetic environnement and examines the even more fundamental problem of working with anomalies that are not perfectly isolated.

Chapter 3 : First modeling results

Chapter 3 will present the method and results obtained during the first round of modeling. In this part of the work I modeled 9 relatively isolated magnetic anomalies with an elliptical prism of varying shape, position and magnetization. Both the low and high altitude data are used. For the low altitude data, selected tracks are used over each anomaly of interest. The tracks are detrended by removing a quadratic fit of each track. High altitude data are binned and smoothed in the Fourier domain to reduce remaining external contribution. The goal of this modeling effort is to find the orientation of the ancient core field (paleomagnetic pole position) that created each anomaly and discuss the geophysical implication of the results.

Chapter 4 : Second round of modeling

Chapter 4 presents the result of a new round of modeling with high altitude data only. Again elliptical prisms are used. I calculate the paleomagnetic pole position for the same 9 anomalies of chapter 3 but in a very different way. The huge high altitude data set is separated into two subsets and anomaly data is extracted from each subsets. As in chapter 3 the data is smoothed in the Fourier domain. The unsmoothed and smoothed data is then modeled for each component of the magnetic field. The low altitude radial data is also modeled for comparison purposes. In total, for each anomaly, 13 data sets are modeled giving 13 paleopole positions. In theory, if we were working with absolutely clean and isolated anomalies all 13 paleopole positions would coincide perfectly. Of course, in practice, that's not what we get and how close the different paleopoles are is a great test of the confidence we can have in the paleopole positions found.

Chapter 5 : Conclusion and future research

Finally chapter 5 makes a global resume of the work done and describes areas where future research should concentrate. I will point out the enormous lack of standardization in data manipulation and cleaning between the different investigators and emphasize that this problem should be looked into before going on any further (just that would make for some good PhD work

here !!!). The fundamental problem of non-uniqueness is discussed in the context of the Martian magnetic field. A short discussion on the applicability of the results to constrain the internal structure of Mars concludes the thesis.

Chapter 1: Rotational dynamics

1.1 Introduction

The rotational behavior of most objects is in appearance very simple. If one considers the Earth for example, our planet makes one rotation every 24 hours and for most people that's the end of it. However physicists, geophysicists and astronomers have known for quite some time that there is a lot more to this story than a simple alternance between night and day. The Earth is subjected to forces that influence its rotation. The rotation period is not constant and the axis of rotation itself changes its alignment with respect to the stars and to the surface of the Earth. Over a long period of time these changes have a profound effect on the geology and climate of our planet [*Evans*, 2001]. Polar wander can also affect sea level and change it in the ten's of meters proportion [*Mound and Mitrovica*, 1998] As a consequence, changing climate and geology will have serious consequences on the different ecosystems that make up the Earth. It is not exaggerated to say that the development of life on Earth has been affected by the rotational behavior of our planet.

Changes in the rotational behavior of a planet can be divided basically in two groups. First there are the changes in the alignment of the axis of rotation with respect to the fixed background of the celestial sphere. In the case of our planet these changes are mainly due to the forces exerted by the sun and the moon on the equatorial bulge of the Earth. The best-known rotational change in this group is the lunisolar precession. It corresponds to a slow circular motion of the Earth's rotation axis with respect to the fixed star background. The period of the lunisolar precession is about 26,000 years. Because of precession the seasons will be inverted and 13,000 years from now it will be winter in July in the northern hemisphere and summer in the southern hemisphere, the exact opposite of what we have today. This is an obvious example of the effect of changing rotation behavior on climate.

The changes of the axis of rotation with respect to the stars are very interesting subjects but they do not represent the focus of this thesis because of their limited geophysical effects on the Earth and other terrestrial planets. In this thesis I am more concerned with a second group of rotational changes, that is those changes of the rotational axis alignment with respect to the body's surface. In this group the axis of rotation is fixed by angular momentum conservation and it is the planet's surface that move with respect to the axis of rotation. An outside observer would see the shifting of the Earth with respect to the axis, while an observer on the surface would see the axis move and therefore the poles of rotation would change position with time. These changes are the ones geophysicists are most interested in because they are greatly dependant on the internal structure of the rotating body.

These changes are called polar motion or polar wandering. The two terms are synonymous. On a planet, the angular distance a given point at the surface has moved relative to the axis of rotation measures polar motion. Polar motion is created by internal mass anomalies and surface loads that affect the inertia tensor of the planet. The inertia tensor is a fundamental characteristic of the rotational behavior of a planet and is dependant on the internal distribution of mass. As such, knowing the inertia tensor of an object gives one a very good constraint on its internal structure. Any changes in the mass distribution inside or at the surface of a planet will change the inertia tensor and affect the rotation of the body. On short time scales movement of air and water masses will affect the rotation of the Earth. On longer time scales, the movement of plates at the surface and of internal mass anomalies due to mantle convection will have a durable effect on Earth's rotation. The notion of inertia tensor will be discussed in the next section of this chapter. On Mars the atmospheric winds and the seasonal mass exchange (in the form of CO_2 sublimation and condensation) between the ice caps and atmosphere affect the planet's rotation and the length of day. [*Defraigne et al.*, 2000]

On Earth two major elements combine to move surface objects relative to the axis of rotation: Polar motion and plate tectonic. These are two very different phenomena. Plate tectonic is produced by convection inside the mantle. If one takes into account the combined effect of the two phenomena we have apparent polar wander (APW). If we remove the displacement due to

plate tectonics and define the position of the axis of rotation with respect to a fixed position on the lithosphere then we are dealing with true polar wander (TPW). On Earth, hotspots in the mantle move very slowly and are considered good reference points. Astronomical measurements have indicated a polar motion rate of about 10cm/year mostly associated with postglacial rebound [*Vermeersen and Sabadini*, 1999]. On other planets a fixed reference point has not yet been identified.

It is now well accepted that the Earth has experienced some polar motion episodes. This, combined with plate tectonics, has dramatically changed the surface aspect of the Earth. For example one period of Earth history, which has seen major changes, is the Cambrian period that went from 540 Ma to 490 Ma ago. The speed at which continents moved at that time could have been as high as 20 to 40 cm/y [*Mert*,1999]. That period also saw important changes in the biological mass, seawater chemistry and possibly a major change in climate going from severe icehouse to green house climate. One theory that has been proposed to explain this high rate of plate motion is inertial interchange true polar wander (IITPW) . This is a special and extreme case of TPW where the Earth's intermediate inertial axis and maximum axis interchange requiring a 90 deg shift of the surface relative to the axis of rotation. This hypothesis initially proposed by *Kirschvink et al.* [1997] would require a huge variation in the earth's internal mass distribution in a relatively short geological time.

The IITPW hypothesis has been disputed by *Mert* [1999] on the basis of paleomagnetic studies that indicate that the rate of polar motion seems to change from continent to continent and that in most cases the amount of polar motion is well below the 90 deg required by the IITPW hypothesis. He suggested that the high rate of APW in the Cambrian period would be caused by a combination of TPW and increased plate motion due to lower mantle thermal anomalies. However he assumed in his analysis that the rate of plate motions is lower than the IITPW rate therefore indicating that the low total polar motion signal observed is from IITPW only. One could also assume, however, that in some cases at least, the plate motion is opposite to the polar motion therefore reducing artificially the total signal. No matter how you look at it, however TPW seems to be part of the solution for this very tectonically active period of Earth's history.

1.1.1 TPW of Mars : Past work

Given the physical nature of terrestrial planets it is highly unlikely that the Earth would be the only planet to experience TPW. Before going into the physical details of polar motion theory I discuss in this section the general geology of Mars and point out the different aspects of that geology that makes us think that TPW might have been a very important part of Martian history.

Although considered to be closest to Earth as far as physical characteristics are concerned, Mars is still a very different planet than Earth. It lacks plate tectonics and is now considered a one-plate planet [*Wieczorek and Zuber*, 2004]. Mars does not have continents but its topography is dominated by two very long wavelength features. The first one is the crustal dichotomy between the northern and southern hemisphere. Most of the northern hemisphere is at a lower elevation than the southern hemisphere. The terrain in the north is also much smoother than the heavily cratered south indicating possibly a difference in age. However that difference in age has been disputed, some investigators arguing that only the top few kilometers of the northern plains are actually younger [*Frey et al.*, 2001 ; *Wieczorek and Zuber*, 2004].

The second long wavelength feature is the Tharsis plateau. Tharsis is an enormous volcanic construct at the surface of Mars. It includes to the east the Valles Marineris canyon system and to the west the huge Olympus Mons volcano. Tharsis acts as an immense surface load on Mars and should be considered a prime suspect for the cause of TPW on Mars. As we will see in the theory, exposed in the next sections of this chapter, any surface load can drive polar motion. However the state of compensation of Tharsis must also be evaluated in order to determine it's exact influence on TPW. As we will see later, compensation can severely diminish the effect of a load on TPW.

The Tharsis plateau is itself dominated by huge volcanoes that are now extinct. With Olympus Mons mentioned above there are the Tharis Montes, a string of 3 large volcanoes aligned along a southwest northeast line right in the middle of Tharsis. Again these volcanoes can be considered

as surface loads and might drive polar motion. The mere presence of these volcanoes is indicative of an early Mars that is very different than what it is today. The surface of Mars shows numerous signs of large liquid movement . That liquid was most probably water and may even have created some of the observed magnetic anomalies. Very recent discoveries by the Mars exploration rovers Spirit and Opportunity seems to indicate that very large body of water once existed on Mars implying that the temperature and general atmosphere of the planet was very different early in Martian history than it is today.

However, on Mars, polar wandering has been first suspected for geological reasons. *Murray and Malin* [1973] hypothesized polar wandering on Mars based on observation of quasi-circular, laminated features in the polar region that are similar to regions at the actual poles. See figure 1.1. They proposed polar motion of up to 15 deg based on that observation and used that argument to propose that convection is still active inside Mars. Geological evidence for polar wandering has also been proposed by *Schultz & Lutz* [1988] who pointed out resemblances between the actual polar deposits and deposits near the equator. They also hypothesized that some special craters named 'pedestal craters' can only have been formed in polar regions. They predicted polar wandering of up to 120 deg, implying major mass redistribution early in Martian history.

In my view such a high value for polar motion is very unlikely in the case of Mars due to the fact that Tharsis is such a dominant load at the surface of Mars. One load alone, no matter how important, cannot drive polar motion over 90^{o} (see section 1.4.2). To obtain polar motion higher than 90^{o} one would need to invoke many similar loads acting on different time scales. Tharsis is so huge that the effect on polar motion of other surface loads when compared to an uncompensated Tharsis must be small, therefore polar motion greater than 90^{o} is unlikely. Polar motion on Mars is more likely due to surface loading while polar motion on Earth is due to convection and movement of internal loads [*Spada et al.*, 1996] (see section 1.7). An actively convecting planet, like the Earth, would, on the other hand, be more likely to experience huge polar motion, even one higher then 90^{o}, because of movement on internal mass anomalies. In the case of Mars, geological interpretation of surface features is less constrained and the physics of

polar motion outlined in the next few sections, when applied to Mars, does not support extremely high polar motion values.

Although surface expressions of polar motion are likely to exist [*Melosh*, 1980] the interpretation of such surface features is very difficult and highly subjective. Any polar motion theory of Mars must also be based on much stronger geophysical evidence. Unfortunately such evidence is scarce since the internal structure of Mars is only very loosely constrained. It is however well accepted that most significant geophysical events like the formation of the Tharsis rise and the topographic dichotomy happened early in Martian history, most probably within the first 500 My to 1 Gyr in the planet's history [*Spohn et al.*, 2001]. So major episodes of polar wandering on Mars, if any, are probably very ancient. The actual age of Tharsis, however, is still a matter of debate (see section 1.8.2).

The Tharsis rise on Mars is the biggest known topography anomaly in the solar system and has long been suspected to be the main cause of polar wandering on Mars. *Melosh* [1980] predicted polar wandering of up to 25 deg by removing the Tharsis rise from the gravity model. He removed the mass of Tharsis in 10 steps while keeping the total mass of the planet constant. Each time he recalculated the new pole positions by diagonalizing the inertia tensor. He then attempted to predict the tectonic pattern that would result by such reorientation of the rotation axis. Such pattern has yet to be recognized. *Willeman* [1984] challenged this interpretation by suggesting that compensation of the Tharsis rise would limit the amount of polar motion. He suggested a 3 to 9 deg only reorientation by modeling the response of loads on a hydrostatic planet with an elastic lithosphere.

The two very different interpretations by Melosh and Willemann bring to light a fundamental concept in the study of polar wandering : The non-rigidity of the rotating body. *Ricard et al.* [1992] strongly argue for taking into consideration the chemical and viscosity structure of the mantle when modeling the effect of an internal mass anomaly on the amount and direction of polar wandering. The depth and compensation state of the anomalous mass are of prime importance. For example, an anomalous mass near a chemical interface could have no long time

effect on polar wandering due to complete compensation. Since compensation is a factor, a rigid model is incorrect in predicting changes to the inertia tensor and polar motion due to the presence of an anomalous mass at depth. *Ricard at al.* [1992] (see also *Spada et al.* [1994]) go one step further and actually argue that the apparent polar motion path observed here on Earth would only be possible by assuming a viscosity stratification of the mantle, the lower mantle being as much as 30 times more viscous than the upper mantle. They point out that polar wandering could then constrain the viscosity structure of the mantle.

Spada et al. [1996] devised a rotational number Ro that place terrestrial bodies in two possible categories depending on the value of that number. This theory try to predict long term polar motion behavior of terrestrial planets from the extreme values of the rotational number. This rotational number is interesting because it adds another internal structure parameter that can be adapted with improved knowledge of the planet. The following sections of this chapter are an introduction to, and critic of, the mathematical theory of *Spada et al.* [1996]. But, first, the next section discuss the basic physics behind polar motion and set the stage for a more elaborate discussion of the linear and long term formulation of polar motion theory in the remaining sections of this chapter.

1.2 Basic physics of polar motion

Rotational dynamic is the part of physics that try to understand the rotational behavior of objects submitted to forces and loads. It is the basic physical tool that is needed to study polar wandering of terrestrial planets. Rotational dynamics of non-rigid bodies is a very complex subject. This section introduce the most fundamental equations and parameters of rotational dynamics as they are used and applied to the rotation of non-rigid bodies. I start by explaining the concepts of angular momentum and inertia tensor for non-rigid bodies. This will lead to the Euler-Liouville equation that is fundamental in the study of polar motion of a non-rigid body.

1.2.1 Angular momentum of a non rigid body

A non-rigid body is a body for which the parts move relative to one another, therefore, for such a body, the angular momentum and the inertia tensor will change with time. Let's consider a body of mass M and density distribution $\rho(x_1, x_2, x_3)$ rotating with rotational velocity $\vec{\omega}$ as shown in figure 1.2. I have used the notation 1,2,3 to describe the 3 coordinates axes instead of the more traditional x,y and z. This notation is easier to use with complex formulas and will be used throughout this thesis. In figure 1.2 , let point A be the origin of a suitable inertial reference frame and point O the origin of a body frame that rotates with the body. The element angular momentum associated with the mass element dm is given by

$$d\vec{H} = \vec{R} \times \dot{\vec{R}}\, dm \qquad \textbf{1.1}$$

By integrating equation 1-1 we get the total angular momentum, that is

$$\vec{H}_{total} = \iiint_{Volume} \vec{R} \times \dot{\vec{R}}\, dm \qquad \textbf{1.2}$$

Where the integral is carried out over the entire volume of the body. For a non-rigid body, the deformational and rotational part of the total angular momentum can be written as [*Morritz and Muller*, 1987]

$$\vec{H} = \iiint_{Volume} \vec{r} \times \vec{V}_{def}\, dm + \iiint_{Volume} \vec{r} \times (\vec{\omega} \times \vec{r}) dm \qquad \textbf{1.3}$$

where the first integral is the portion of the angular momentum related to the deformation of the body. The second part is related the rotation of the body. The vector $\vec{V}_{def}$ is the average deformation velocity defined as

$$\vec{V}_{def} = \frac{1}{M} \iiint_{Volume} \frac{d\vec{r}}{dt} dm \qquad \textbf{1.4}$$

If one consider the body frame to be geocentric (that is a reference frame with the origin at the center of mass of the body) then in such a frame of reference the average deformation velocity is 0 and the body remain, on average, undeformed [*Morritz and Muller*, 1987]. We put

$$\vec{h} = \iiint_{Volume} \vec{r} \times \vec{V}_{def} \, dm \qquad \textbf{1.5}$$

This term is 0 for a rigid body and is often neglected even in the case of a non-rigid body. We now express the rotational part of the angular momentum in term of the inertia tensor as in

$$[I]\vec{\omega} = \iiint_{Volume} \vec{r} \times (\vec{\omega} \times \vec{r}) dm \qquad \textbf{1.6}$$

and finally rewrite the expression of the angular momentum of a rotating non-rigid body as [*Morritz and Muller* 1987]

$$\vec{H} = [I]\vec{\omega} + \vec{h} \qquad \textbf{1.7}$$

This angular momentum equation is, with equation 1.12 below, the starting point for deriving the polar motion equation of section 1.2.3.

1.2.2 The inertia tensor

The inertia tensor $[I]$ introduced in equation 1.6 is a 3x3 matrix whose components are

$$[I]=\begin{bmatrix} I_{11} & I_{12} & I_{13} \\ I_{21} & I_{22} & I_{23} \\ I_{31} & I_{32} & I_{33} \end{bmatrix} \qquad \textbf{1.8}$$

The diagonal elements are called the moments of inertia (I_{11}, I_{22}, I_{33}) . The off diagonal elements are the products of inertia. The inertia tensor is a symmetrical matrix with $I_{12} = I_{21}$, $I_{23} = I_{32}$ and $I_{13} = I_{31}$. So in total we have six different moments and products of inertia, they are

$$\begin{aligned} I_{11} &= \iiint_{volume}(x_2^2 + x_3^2)dm \\ I_{22} &= \iiint_{volume}(x_1^2 + x_3^2)dm \\ I_{33} &= \iiint_{volume}(x_1^2 + x_2^2)dm \\ I_{12} = I_{21} &= -\iiint_{volume} x_1 x_2\, dm \\ I_{13} = I_{31} &= -\iiint_{volume} x_1 x_3\, dm \\ I_{23} = I_{32} &= -\iiint_{volume} x_3 x_2\, dm \end{aligned} \qquad \textbf{1.9}$$

One will recall that $dm = \rho dV$ where ρ is the density distribution inside the body and dV the volume element containing dm. In the most general case the density distribution is a function of all three coordinates. It is also generally possible, by choosing a suitable choice of coordinates axes, to make the products of inertia equal to 0 so that the inertia tensor can be written as

$$[I]=\begin{bmatrix} A & 0 & 0 \\ 0 & B & 0 \\ 0 & 0 & C \end{bmatrix} \qquad \textbf{1.10}$$

Where we have put $I_{11} = A$, $I_{22} = B$ and $I_{33} = C$. These are called the principal moments of inertia. This situation can arise when one aligns the coordinates axes of the local reference frame in such a way that the mass of the body is evenly distributed relative to the axes. The equation $\vec{H} = [I]\vec{\omega}$ usually means that the angular momentum vector is not in the same direction as the angular velocity vector. If the direction of angular momentum keeps changing, it develops a torque, which forces the axis of rotation to move. But, if both vectors are in the same direction then we can replace the inertia tensor by a scalar moment of inertia I, that is

$$\vec{H} = [I]\vec{\omega} = I\vec{\omega} \qquad \textbf{1.11}$$

I is the equivalent scalar moment of inertia of the body about the given axis of rotation. Any axis that verify equation 1.11 is a principal axis. This equation says that the inertia tensor can be replaced with a single scalar moment of inertia when the axis of rotation is a principal axis. In the case of the rotation of a planet in hydrostatic equilibrium we can write $A = B \neq C$ with $A < C$.

1.2.3 Euler-Liouville equation

From basic physics we know that the time derivative of angular momentum $\dot{\vec{H}}$ is equal to applied torque $\vec{L}$

$$\dot{\vec{H}} = \vec{L} \qquad \textbf{1.12}$$

This also holds for a deformable body. Now expressing the time derivative $\dot{\vec{H}}$ in the body fixed coordinate system with origin O (see figure 1.2) we can write

$$\dot{\vec{H}} = \frac{d\vec{H}}{dt} + \vec{\omega} \times \vec{H} = \vec{L} \qquad \textbf{1.13}$$

Where $\frac{d\vec{H}}{dt}$ is the time derivative of $\vec{H}$ in the body fixed frame and $\vec{\omega}$ the rotational velocity. Replacing the value of $\vec{H}$ (equation 1.7) in this last equation we get [*Lambeck*, 1980]

$$\frac{d}{dt}\left[[I]\vec{\omega} + \vec{h}\right] + \vec{\omega} \times \left[[I]\vec{\omega} + \vec{h}\right] = \vec{L} \qquad \textbf{1.14}$$

This is the Euler-Liouville equation and is the starting point for the study of polar motion for a non-rigid body. One must also keep in mind that the inertia tensor $[I]$ for a non-rigid body is itself time varying since each part of the body move relative to the body fixed reference frame. At this point it is also useful to mention that in the case of a rigid body ($\vec{h} = 0$, see section 1.4) the preceding equation simply becomes

$$\frac{d}{dt}\left[[I]\vec{\omega}\right] + \vec{\omega} \times \left[[I]\vec{\omega}\right] = \vec{L} \qquad \textbf{1.15}$$

If one consider that the body is rotating along the principal axis of inertia (A,B and C) then the preceding equation can be written as a set of 3 equations, that is

$$\begin{aligned} A\dot{\omega}_1 + (C-B)\omega_2\omega_3 &= L_1 \\ B\dot{\omega}_2 + (A-C)\omega_3\omega_1 &= L_2 \\ C\dot{\omega}_3 + (B-A)\omega_2\omega_1 &= L_3 \end{aligned} \qquad \textbf{1.16}$$

1.2.4 Stability of free rotation

One important aspect of the rotational behavior of a planet is the stability of its rotation. A planet rotating with respect to the axis of maximum or minimum inertia will be rotationally stable. In the same manner a planet rotating with respect to it's intermediate moment of inertia will be unstable. To illustrate this consider the Euler-Liouville equation in 1.16 for the case where A < B < C and $\omega_1, \omega_2 \langle\langle \omega_3$. Also assume that the planet is free of external torque (this is free rotation) so that $\vec{L} = 0$. We then have

$$\begin{aligned} A\dot{\omega}_1 + (C-B)\omega_2\omega_3 &= 0 \\ B\dot{\omega}_2 + (A-C)\omega_3\omega_1 &= 0 \\ C\dot{\omega}_3 &= 0 \end{aligned} \qquad \textbf{1.17}$$

From the last equation we immediately get ω_3 = constant = Ω and the first two equations can be written as

$$\begin{aligned} \dot{\omega}_1 + \frac{(C-B)}{A}\omega_2\Omega &= 0 \\ \dot{\omega}_2 + \frac{(A-C)}{B}\omega_1\Omega &= 0 \end{aligned} \qquad \textbf{1.18}$$

Let's take the time derivative of the last equation in 1.18, we find

$$\ddot{\omega}_2 + \frac{(A-C)}{B}\Omega\dot{\omega}_1 = 0 \qquad \textbf{1.19}$$

Substituting $\dot{\omega}_1$ from the first equation in 1.18 we get

$$\ddot{\omega}_2 - \frac{(A-C)}{B}\frac{(C-B)}{A}\Omega^2\omega_2 = 0 \qquad \textbf{1.20}$$

The solution is a simple harmonic motion $\omega_2 = C_1\cos(\sqrt{k}t) + C_2\sin(\sqrt{k}t)$ where k is a constant given by

$$k = -\frac{(A-C)}{B}\frac{(C-B)}{A}\Omega^2 \qquad \textbf{1.21}$$

This constant is positive given A < B < C so that $\sqrt{k}$ is real and the rotation is stable. A similar solution exists for ω_1 and we have exactly the same situation if the rotation is about the axis of lowest inertia. On the other hand if the rotation is about the axis of intermediate inertia equation 1.16 becomes

$$\begin{aligned} A\dot{\omega}_1 + (C-B)\omega_2\omega_3 &= 0 \\ B\dot{\omega}_2 &= 0 \\ C\dot{\omega}_3 + (B-A)\omega_2\omega_1 &= 0 \end{aligned} \qquad \textbf{1.22}$$

So that ω_2 = constant = Ω and by doing a similar derivation as the one described above we get the following differential equation for the ω_3 component of the angular velocity vector

$$\ddot{\omega}_3 - \frac{(C-B)(B-A)}{AC}\Omega^2\omega_3 = 0 \qquad \textbf{1.23}$$

The constant k define by $k = -\frac{(C-B)(B-A)}{AC}\Omega^2$ is always negative leading to a complex exponential solution that is rotationally unstable. A rotating object disturbed by a change in inertia will always try to reach rotational equilibrium by aligning its rotational axis with the axis of maximum inertia. This situation is stable because it correspond to a state of minimal energy.

1.3 Linear formulation of the Euler-Liouville equation

In this section I will give a linear formulation of the Euler-Liouville equation. This formulation simplify the mathematics involved by assuming that one can write the time varying inertia tensor as a sum of two tensors. Also assumed in the linear approximation is that the variations in the inertia tensor and angular velocity are small. This limit the applicability of the linear approximation to about 10^{o}. A rotating deformable body subjected to centrifugal forcing alone will deformed and take the shape of a rotating fluid. This is hydrostatic equilibrium [*Munk and Mcdonald*, 1960]. In this situation the rotation will flatten the body at the poles and create a rotational bulge at the equator. In this case the two principal moments of inertia along the equatorial axis will be equal and called A. The principal moment of inertia along the x_3 rotation axis is called C. The off diagonal product of inertia of the inertia tensor will be 0. We will see later the important role played by this rotational bulge in the amount of polar wandering experienced by a deformable body. With this in mind, I begin the linear formulation of the Euler equation by expressing the time varying inertia tensor of the deformable body as a sum of 2 components. They are

$$[I]=[I_o]+[\Delta I] \qquad \textbf{1.24}$$

where $[I_o]$ represent the inertia tensor of a planet whose principal axis corresponds to the coordinate axis. For a planet in hydrostatic equilibrium the value of $[I_o]$ is

$$[I]=\begin{bmatrix} A & 0 & 0 \\ 0 & A & 0 \\ 0 & 0 & C \end{bmatrix} \qquad \textbf{1.25}$$

The tensor $[\Delta I]$ in equation 1.24 is the variation of the inertia tensor due to load forcing. Since the action of the load is usually time dependant, this tensor will also be time dependant. Let's again identify the 3 axes of the body frame by x_1, x_2 and x_3 where x_1 and x_2 are the equatorial axes and x_3 is the polar axis. The value of $[\Delta I]$ is

$$[\Delta I] = \begin{bmatrix} \Delta I_{11} & \Delta I_{12} & \Delta I_{13} \\ \Delta I_{21} & \Delta I_{22} & \Delta I_{23} \\ \Delta I_{31} & \Delta I_{32} & \Delta I_{33} \end{bmatrix} \qquad \textbf{1.26}$$

So that

$$[I] = \begin{bmatrix} A + \Delta I_{11} & \Delta I_{12} & \Delta I_{13} \\ \Delta I_{21} & A + \Delta I_{22} & \Delta I_{23} \\ \Delta I_{31} & \Delta I_{32} & C + \Delta I_{33} \end{bmatrix} \qquad \textbf{1.27}$$

The rotation vector $\vec{\omega}$ can likewise be expressed as a sum of two terms

$$\vec{\omega} = \vec{\omega}_o + \Delta\vec{\omega} \qquad \textbf{1.28}$$

where $\vec{\omega}_o$ is

$$\vec{\omega}_o = \begin{bmatrix} 0 \\ 0 \\ \Omega \end{bmatrix} \qquad \textbf{1.29}$$

and represent the constant rotation velocity of the body around the axes x_3. The variation in rotational velocity $\Delta\vec{\omega}$ that will produce actual polar motion is given by [*Lambeck*, 1980]

$$\Delta\vec{\omega} = \begin{bmatrix} m_1 \\ m_2 \\ m_3 \end{bmatrix} \Omega \qquad \textbf{1.30}$$

where m_1 and m_2 expressed the deviation of the rotation axis with respect from the initial axis x_3 and m_3 the variation of the rotational period. Now if we use the linear approximation and assume that both $[\Delta I]$ and $\Delta\vec{\omega}$ are small quantities whose squares, products and higher powers can be neglected we can build the linear version of the Euler-Liouville equations by substituting $[I]$ and $\vec{\omega}$ in equation 1.14. After a lengthy algebra work we get [*Morritz and Muller*, 1987)]

$$A\dot{m}_1\Omega + \Delta\dot{I}_{13}\Omega + \dot{h}_1 + (C-A)m_2\Omega^2 - \Delta I_{23}\Omega^2 - h_2\Omega = L_1 \qquad \textbf{1.31}$$

$$A\dot{m}_2\Omega + \Delta\dot{I}_{23}\Omega + \dot{h}_2 - (C-A)m_1\Omega^2 + \Delta I_{13}\Omega^2 + h_1\Omega = L_2 \qquad \textbf{1.32}$$

$$C\dot{m}_3\Omega + \Delta\dot{I}_{33}\Omega + \dot{h}_3 = L_3 \qquad \textbf{1.33}$$

Equations 1.31, 1.32 and 1.33 are the linear form of Euler-Liouville equation 1.14. We need to solve this system of differentials equations for the parameters m_1, m_2 and m_3. We can combine equations 1.31 and 1.32 by defining the following complex variables

$$\begin{aligned} m &= m_1 + i m_2 \\ L &= L_1 + i L_2 \\ h &= h_1 + i h_2 \end{aligned} \qquad \textbf{1.34}$$

$$c = \Delta I_{13} + i\Delta I_{23}$$

By substituting equation 1.34 into equations 1.31 and 1.32 we get [*Morritz and Muller*, 1987]

$$A\Omega\dot{m} + \dot{h} + ih\Omega + c\Omega + i\Omega^2 c - \Omega^2 m(C - A) = L \qquad \textbf{1.35}$$

This last equation can then be solved for m (that is m_1 and m_2) characterizing the deviation of the rotation axis from the original x_3 axis, that is polar motion. One must keep in mind however that, because of the conservation of angular momentum, the rotational axis is fixed for an outside observer and that it is the surface that is moving with respect to rotational axis. *Lambeck* [1980] gives the linear Euler-Liouville equations 1.31 to 1.33 in term of excitation functions Ψ. In his formalism the Euler-Liouville equation 1.31 to 1.33 becomes

$$\begin{aligned} \frac{\dot{m}_1}{\sigma_r} + m_2 &= \Psi_2 \\ \frac{\dot{m}_2}{\sigma_r} - m_1 &= -\Psi_1 \\ \dot{m}_3 &= \dot{\Psi}_3 \end{aligned} \qquad \textbf{1.36}$$

where the term σ_r is the frequency of free nutation of a rigid body (see next section). The value of σ_r is

$$\sigma_r = \Omega\frac{(C - A)}{A} \qquad \textbf{1.37}$$

The excitation functions are given by

$$\Psi_1 = \frac{\left|\Omega^2\Delta I_{13} + \Omega\Delta\dot{I}_{23} + \Omega h_1 + \dot{h}_2 - L_2\right|}{\Omega^2(C - A)} \qquad \textbf{1.38}$$

$$\Psi_2 = \frac{\left[\Omega^2 \Delta I_{23} - \Omega \Delta \dot{I}_{13} + \Omega h_2 + \dot{h}_1 + L_1\right]}{\Omega^2 (C - A)}$$

$$\Psi_3 = \frac{-\Omega^2 \Delta I_{33} - \Omega h_3 + \Omega \int_0^t L_3 dt}{\Omega^2 C}$$

The excitation functions include all the factors that perturb the rotational motion from the one defined from a rigid body. One can now use the Lambeck formalism (equations 1.36 and 1.38) to express the Euler-Liouville equations and related excitation functions in complex form. Let's define the following complex variables [*Lambeck*, 1980]

$$\begin{aligned}
\Psi(t) &= \Psi_1(t) + i\Psi_2(t) \\
\Delta I(t) &= \Delta I_{13}(t) + i\Delta I_{23}(t) \\
m(t) &= m_1(t) + i m_2(t) \\
h(t) &= h_1(t) + i h_2(t) \\
L(t) &= L_1(t) + i L_2(t)
\end{aligned} \qquad \textbf{1.39}$$

Where i is the imaginary unit. Introducing equation 1.39 into equations 1.36 and 1.38 and combining we get for the Euler-Liouville equation in complex form

$$i\frac{\dot{m}(t)}{\sigma_r} + m(t) = \Psi(t) \qquad \textbf{1.40}$$

where σ_r is given by equation 1.37. The complex form of the excitation function is

$$\Psi(t) = \frac{1}{\Omega^2 [C - A]}\left[\Omega^2 \Delta I(t) - i\Delta \dot{I}(t) + \Omega h(t) - i\dot{h}(t) + iL(t)\right] \qquad \textbf{1.41}$$

1.4 Application of the Euler-Liouville equation for a rigid body

It is interesting to apply the Euler-Liouville equation to the simple case of a rigid body. This tells us a lot about the fundamental behavior of planets submitted to inertia changes. A rigid body will exhibit as a crude first approximation the basic rotational behavior of the planets. I will use this section to illustrate some simple but important geophysical situations present on Mars and the Earth. However, one must keep in mind that there are important differences between the rotation of a rigid body and the actual rotation of the planets, so that, in the end a rigid body is not adequate to explain correctly the rotational behavior of the planets. I will justify this affirmation at the end of this section.

1.4.1 Rigid body with no surface load

Let's first imagine the simplest of cases of a rigid body with equatorial moment of inertia A and polar moment of inertia C. In this first case we will consider no load at the surface. In this situation we have

$$\vec{h} = 0 \; ; \; \dot{\vec{h}} = 0 \; ; \; \Delta I = 0 \; ; \; \Delta \dot{I} = 0 \qquad \textbf{1.42}$$

If we also assume that external torque is 0 then the Euler-Liouville equation 1.16 becomes

$$\begin{aligned} A\dot{m}_1\Omega + (C-A)m_2\Omega^2 &= 0 \\ A\dot{m}_2\Omega - (C-A)m_1\Omega^2 &= 0 \\ C\dot{m}_3\Omega &= 0 \end{aligned} \qquad \textbf{1.43}$$

Let's put

$$\sigma_r = \left[\frac{C-A}{A}\right]\Omega \qquad \textbf{1.44}$$

So that we can rewrite equation 1.43 as

$$\begin{aligned} \dot{m}_1 + \sigma_r m_2 &= 0 \\ \dot{m}_2 - \sigma_r m_1 &= 0 \\ \dot{m}_3 &= 0 \end{aligned} \qquad \textbf{1.45}$$

The solution to the last equation is simply m_3 = cte so that $\omega_3 = \Omega$ and the period of rotation of the body is not affected. One can also quickly realized that in the case of a spherical rigid body (A = C) one have also m_1 =0 and m_2 = 0 so that there is no polar motion at all in this situation. From the second equation in 1.45 one get

$$m_1 = \frac{\dot{m}_2}{\sigma_r} \Rightarrow \dot{m}_1 = \frac{\ddot{m}_2}{\sigma_r} \qquad \textbf{1.46}$$

Replacing in the first equation of 1.45 we find

$$\ddot{m}_2 + \sigma_r^2 m_2 = 0 \qquad \textbf{1.47}$$

Which is a simple harmonic motion equation. The equation for m_1 will be similar so that solution m_1 and m_2 which give polar motion are

$$\begin{aligned} m_1 &= m_o \cos[\sigma_r t + \gamma] \\ m_2 &= m_o \sin[\sigma_r t + \gamma] \end{aligned} \qquad \textbf{1.48}$$

This situation is completely analog to the rotation of a top. The axis of rotation will make a circular motion of amplitude m_o and period $T = 2\pi/\sigma_r$. On Earth this periodic polar motion is called Chandler Wobble. The Chandler Wobble period for a rigid Earth is 305 days much lower than the measured period of 435 days [*Lambeck*, 1980]. This is due to the non-rigidity of the

Earth. The Chandler Wobble period of a rigid Mars as been estimated to be 190.6 days and the non-rigid period to be 201.8 days [*Hoolst et al.*, 2000].

1.4.2 Rigid body with an instantaneous surface load

A slightly more realistic situation arise when a load is put at the surface of the rotating body. Let's imagine that a load is instantaneously put at the surface at time t =0 and that the load remain constant in time. In this situation we have

$$\vec{h} = 0 \; ; \; \dot{\vec{h}} = 0 \; ; \; \Delta\dot{I} = 0 \qquad \textbf{1.49}$$

One must now take into account the perturbation to the inertia tensor so that $\Delta I \neq 0$. Again assuming that there is no external torque the Euler-Liouville equation 1.16 becomes

$$\begin{aligned} A\dot{m}_1\Omega + (C-A)m_2\Omega^2 - \Delta I_{23}\Omega^2 &= 0 \\ A\dot{m}_2\Omega - (C-A)m_1\Omega^2 + \Delta I_{13}\Omega^2 &= 0 \\ C\dot{m}_3\Omega &= 0 \end{aligned} \qquad \textbf{1.50}$$

Again the last equation in 1.50 yield the solution m_3 = constant so that the period of rotation does not change. By using equation 1.44 in equation 1.50 we find

$$\begin{aligned} \dot{m}_1 + \sigma_r m_2 &= \frac{\Delta I_{23}\Omega}{A} \\ \dot{m}_2 - \sigma_r m_1 &= -\frac{\Delta I_{13}\Omega}{A} \end{aligned} \qquad \textbf{1.51}$$

In the same manner as in the preceding section, the two equations in 1.51 can be combined to give

$$\ddot{m}_2 + \sigma_r^2 m_2 = \frac{\Delta I_{23}\Omega\sigma_r}{A} \qquad \textbf{1.52}$$

This is a non-homogenous harmonic equation, the solution is

$$m_2 = m_o \cos[\sigma_r t + \gamma] + \frac{\Delta I_{23}}{(C-A)} \qquad \textbf{1.53}$$

A similar solution exist for m_1. One can see that if $\Delta I_{23} > 0$, that is if there is a mass excess then

$$\frac{\Delta I_{23}}{(C-A)} > 0 \qquad \textbf{1.54}$$

since C > A and m_2 is a positive value. The mass excess is brought to the equator. If the inertia perturbation is a mass deficit ($\Delta I_{23} < 0$) then m_2 is negative value and the perturbation is brought to the pole. If one considers a mass excess, then once it is at the equator we have $\Delta I_{23} = 0$ and polar motion stop. This simple example is important because it describes the most fundamental rotational behavior of any planet, rigid or not, submitted to a surface load. It tells us that in theory any uncompensated load, no matter how big or small, added to the surface or removed from the surface of a planet will induce polar motion. This means that any mountains, volcanoes or other excess mass will make the axis of rotation of a planet change with time in a way that depends on the time evolution of the inertia perturbation. This last factor is one of the greatest unknown in any attempt to model polar motion of a planet. In the case of Mars the Tharsis volcanoes are surface loads. Tharsis itself can be considered as an immense load on the surface. Polar motion has likely been induced by these loads.

However one must keep in mind the fact that planets are non-rigid bodies on geological time scales. Any load at the surface will try to sink into the lithosphere until compensated. This is especially true for long wavelength loads like Tharsis. Compensation, as we will see later, reduces polar motion by bringing the load closer to the axis of rotation thus reducing the effect of

the change in inertia due to the load itself. To determine if Tharsis can be truly responsible of polar motion on Mars we must investigate it's state of compensation.

Later in this thesis I will make a short presentation on our state of knowledge of the compensation of Tharsis. If long wavelength loads are more likely to be compensated the opposite is true for smaller loads like mountains and volcanoes. For a planet like Mars, thought to have a very strong lithosphere, surface loads of small wavelength will be more difficult to compensate and may, in the end, contribute more to polar motion than Tharsis itself. *Arkani-Hamed* [2001] has hypothesized that some mass excess must exist underneath the Tharsis volcanoes based on gravity modeling. These sub surface loads would make the contribution of volcanoes to polar motion even more important.

One other aspect of polar motion worth mentioning is the fact that even slow changes to the total moment of inertia can bring very quick polar motion. *Goldreich and Tomre* [1969] have demonstrated that by expanding the classical example of *Gold* [1955] who has studied the rotational impact of a small beetle moving at the surface of a planet. In the case of *Goldreich and Tomre* [1969], a colony of beetles moved slowly in random directions at the surface of the planet. The resulting changes in the inertia tensor of the planet produced rapid movement of the axis of rotation.

1.5 Long term polar motion of a deformable body rotation

A non-rigid body will deform under stress and outside forces. The force deforming the body can be a surface or internal load, a tidal force or a centrifugal force. The best example of such deformation is the flattened shape a non-rigid planet takes due to it's own rotation. In the long term the planet will take the shape of a fluid with comparable density stratification. The deformation of the planet, whatever the cause, will influence polar motion because it will change the inertia tensor of the planet. As a first approximation the deformation can be made to be proportional to the perturbing force. This is similar to the well-known Hooke law of elasticity. However the deformed object will change the potential around it and therefore the perturbing force will in the end change the gravitational potential of the body. The force acting on the body can be represented by a potential V_{pert} and the deformation of the body resulting from this potential will give rise to a variation in the gravitational potential of the body ΔV_{grav}. The two potentials can be connected together by a number called the Love number that describe in one number the elastic properties of the body and it's capacity to respond to a perturbing potential [*Love*, 1927]. The relationship is

$$\Delta V_{grav} = k V_{pert} \qquad \textbf{1.55}$$

Love numbers are expressed relative to a given harmonic degree and are dependant on the internal structure of the body and are also time dependant in most situations.

1.5.1 Love number and the Laplace domain

The time dependence of Love number is generally expressed in the Laplace domain as [*Ricard et al.*, 1992]

$$k(s) = k_e + \sum_{i=1}^{M} \frac{k_i}{s - s_i} \qquad \textbf{1.56}$$

where k_i are representative of each visco-elastic mode. The number of mode M depends on the stratification model used to describe the body. A simple model consisting of a mantle and a core would give 2 modes, one for the deformation of the surface, the other for the deformation of the core mantle boundary. The relaxation time τ_i for a given mode is [*Ricard at al.*, 1992]

$$\tau_i = -\frac{1}{s_i} \qquad \textbf{1.57}$$

This is the time it takes a layer to reach a stress free state after the forcing has been applied. I feel it is now worth digressing a bit from our logical train of thought to better explain the significance of the last two equations. Love numbers are completely analogous to the rigidity constant of the familiar Hooke law relating stress and strain in a linear solid. The Hooke law is simply

$$\sigma = k\varepsilon \qquad \textbf{1.58}$$

where σ is the stress, k the rigidity constant and ε the resulting strain. Viscous behavior, that is friction of the molecules of a given material, is expressed as a linear relationship between stress and strain rate, that is

$$\sigma = \eta\dot{\varepsilon} \qquad \textbf{1.59}$$

where η is the viscosity of the material. The relaxation time τ is defined as the ratio of viscosity over rigidity

$$\tau = \frac{\eta}{k} \qquad \textbf{1.60}$$

A solid that respond linearly to stress (Maxwell solid) can be modeled by a series connection between a linear spring representing rigidity and a dashpot representing viscosity. In this case the total strain on the system will be the sum of the strain of each element

$$\varepsilon = \varepsilon_S + \varepsilon_D \qquad \textbf{1.61}$$

Taking the time derivative of this last expression and knowing that $\dot{\varepsilon}_D = \sigma/\eta$ and $\dot{\varepsilon}_S = \dot{\sigma}/k$ the last equation becomes

$$\dot{\varepsilon} = \frac{\dot{\sigma}}{k} + \frac{\sigma}{\eta} \qquad \textbf{1.62}$$

Rearranging and using the relaxation time τ we have

$$k\dot{\varepsilon} = \dot{\sigma} + \frac{\sigma}{\tau} \qquad \textbf{1.63}$$

This last equation relate stress and strain in a linear viscous solid. It can be put into a much simpler form by making the transformation from the time domain to the Laplace domain. Let's take the Laplace transform of the last equation. We have

$$ks\varepsilon(s) = s\sigma(s) + \frac{\sigma(s)}{\tau} \qquad \textbf{1.64}$$

where *s* is the Laplace variable. We can rearrange this last expression to get a relationship between stress and strain for a linear Maxwell solid in the Laplace domain. We get

$$\sigma(s) = \left[\frac{ks}{s + \frac{1}{\tau}}\right]\varepsilon(s) \qquad \textbf{1.65}$$

Which is similar to Hooke law in the time domain. By taking the problem into the Laplace domain we have transformed a viscoelastic problem into an elastic one. This is the correspondence principle. Another useful property of the Laplace transform is its capacity to transform a differential equation into a simpler algebraic one. By taking the polar motion equation from the time to the Laplace domain we will then get a simpler equation to solve. Once the solution is found in the Laplace domain one has only to inverse Laplace transform it to obtain the solution in the time domain.

1.5.2 Fluid and secular Love numbers

Love numbers are given for a given harmonic degree. In the case of rotational deformation this is degree 2 since, as we will see later, the degree 2 expansion of the gravitational potential is related to the different products of inertia of the rotating body. If one consider an infinite time span the Love number k(s) becomes the fluid Love number k_f given by [*Spada et al.*, 1996]

$$k_f = k_e - \sum_{i=1}^{M} \frac{k_i}{s_i} \qquad \textbf{1.66}$$

which is obtained for a body in hydrostatic equilibrium. Another Love number of interest is the secular Love number given by [*Munk and Macdonald*, 1960]

$$k_o = 3G\left[\frac{C-A}{a^5\Omega^2}\right] \qquad \textbf{1.67}$$

where G is the universal gravitational constant, a is the equatorial radius and Ω the angular velocity. I will derive this formula in section 1.5.4. This Love number represent the resistance a body offer to rotational deformation. The difference between the two Love numbers described above is very small and can usually be neglected. The logic behind the use of Love numbers is interesting because it adds a new internal structure parameter in the description of the rotational behavior of non-rigid bodies. A parameter

that can be adapted as a given model becomes more precise. So far only the equatorial and polar moment of inertia A and C were related to the internal structure of the body. It is therefore important to express the polar motion equation in term of the appropriate Love number. That's what we will do in this section. Essentially what this mean is that we have to express the changes in the product of inertia appearing in the polar motion equation 1.40 as a function of the appropriate Love number.

1.5.3 Expressing polar motion in term of Love numbers

One of the most fundamental perturbing potential comes from the deformation imposed by the body's own rotation. The change in the shape of the body will create a change in the gravitational potential that is directly related to the perturbing potential. In this case the perturbing potential is the centrifugal potential that comes from the centrifugal force. This potential is responsible for the hydrostatic shape of a rotating non-rigid planet. This potential at a point P if given by [*Lambeck*, 1980]

$$V_{cent} = \frac{1}{2}\omega^2(t)L^2 \qquad \textbf{1.68}$$

Where ω is the rotational velocity vector and L is the distance of point P to the axis of rotation represented by the $\vec{\omega}$ vector. This potential can be divided into a radial contribution, which has no consequence on the shape of the body, and a centrifugal contribution that is responsible for the hydrostatic shape

$$V_{cent} = \frac{1}{3}\omega^2(t)x^2 + \Delta V_{cent} \qquad \textbf{1.69}$$

Where the perturbing potential ΔV_{cent} can be expressed in term of the three components of the rotational velocity and the three components of the position vector of point P. We get [*Lambeck*, 1980]

$$\Delta V_{cent} = \frac{1}{6}\omega_1^2\left[x_2^2 + x_3^2 - 2x_1^2\right] + \frac{1}{6}\omega_2^2\left[x_1^2 + x_3^2 - 2x_2^2\right] + \frac{1}{6}\omega_3^2\left[x_1^2 + x_2^2 - 2x_3^2\right] \\ - \omega_1\omega_2 x_1 x_2 - \omega_1\omega_3 x_1 x_3 - \omega_2\omega_3 x_2 x_3 \qquad \textbf{1.70}$$

Using the appropriate associated Legendre function of degree 2 one can write the last equation as

$$\Delta V_{cent}(\theta,\varphi,t) = \frac{1}{6}r^2\left[\omega_1^2 + \omega_2^2 - 2\omega_3^2\right]P_{20}(\cos(\theta)) - \frac{1}{3}\left[\omega_2\omega_3\sin(\varphi) + \omega_3\omega_2\cos(\varphi)\right]P_{21}(\cos(\theta)) \\ + \frac{1}{12}\left[\left(\omega_2^2 - \omega_1^2\right)\cos(2\varphi) - 2\omega_1\omega_2\sin(2\varphi)\right]P_{22}(\cos(\theta)) \qquad \textbf{1.71}$$

Where r, θ and φ are the usual spherical coordinates. That deforming potential changes the gravitational potential by an amount ΔV_{grav} proportional to ΔV_{cent}. The proportionality constant being the tidal Love number $k^T(t)$ as explained in the last section. Therefore we have

$$\Delta V_{grav} = k^T(t)\Delta V_{cent} \qquad \textbf{1.72}$$

It is general practice to express the gravitational potential of a complex body by a spherical harmonic expansion of the form [*Geodynamics : course notes* , 2001]

$$V_{grav}(r,\theta,\varphi) = \frac{GM}{r} + \frac{GM}{r}\left[\sum_{n=0}^{\infty}\sum_{m=0}^{n}\left[\frac{a}{r}\right]^2\left[C_{nm}\cos(m\varphi) + S_{nm}\sin(m\varphi)\right]P_{nm}(\cos(\theta))\right] \qquad \textbf{1.73}$$

where a is the equatorial radius of the body. This expression is essentially the sum of the potential created by a sphere of mass M and radius r plus a second term which is the change in potential caused by body deformation and non radial density distribution. Taking out, from the second term to the right of the last expression, the n = 2 part that influence rotation we have for a point at the surface of the body (r = a)

$$\Delta V_{grav} = \frac{GM}{a}\left[C_{20}P_{20}(\cos(\theta)) + \left[C_{21}\cos(\varphi) + S_{21}\sin(\varphi)\right]P_{21}(\cos(\theta))\right] + \qquad \textbf{1.74}$$

$$\frac{GM}{a}[C_{22}\cos(2\varphi)+S_{22}\sin(2\varphi)]P_{22}(\cos(\theta))$$

Now comparing this last expression with equations 1.71 and 1.72 for ΔV_{cent} one can express the 5 degree 2 coefficients in term of the tidal Love number and the different components of the velocity vector $\vec{\omega}$. By equating the terms that are expressed with the same Legendre associated function we find

$$C_{20}=\frac{k^T a^3}{6GM}\left[\omega_1^2+\omega_2^2-2\omega_3^2\right]$$

$$C_{21}=-\frac{1}{3}\frac{a^3 k^T}{GM}\omega_1\omega_3$$

$$S_{21}=-\frac{1}{3}\frac{a^3 k^T}{GM}\omega_2\omega_3 \qquad \textbf{1.75}$$

$$C_{22}=\frac{1}{12}\frac{a^3 k^T}{GM}\left[\omega_2^2-\omega_1^2\right]$$

$$S_{22}=-\frac{1}{6}\frac{a^3 k^T}{GM}\omega_1\omega_2$$

These coefficients can also be written in term of the moments and products of inertia obtained from the expansion in spherical harmonics of the gravitational potential (equation 1.73). One obtain

$$C_{20}=-\frac{1}{2Ma^2}\left[\Delta I_{11}+\Delta I_{22}-2\Delta I_{33}\right] \qquad \textbf{1.76}$$

$$C_{21}=-\frac{\Delta I_{13}}{Ma^2}\ ,\quad C_{22}=\frac{\Delta I_{11}-\Delta I_{22}}{4Ma^2}$$

$$S_{21} = -\frac{\Delta I_{23}}{Ma^2} \quad , \quad S_{22} = -\frac{\Delta I_{12}}{2Ma^2}$$

Now comparing coefficient by coefficient in 1.75 and 1.76 one can get the following values for the important ΔI_{13} and ΔI_{23} terms of the polar motion equations 1.40 and 1.41

$$\Delta I_{13} = -Ma^2 C_{21} = \frac{k^T a^5}{3G}\omega_1\omega_3$$

$$\Delta I_{23} = -Ma^2 S_{21} = \frac{k^T a^5}{3G}\omega_2\omega_3 \qquad \textbf{1.77}$$

Now assuming a linear approximation for the angular velocity, similar to the one used in the preceding section

$$\vec{\omega}(t) = \begin{bmatrix} m_1(t) \\ m_2(t) \\ 1 + m_3(t) \end{bmatrix} \Omega \qquad \textbf{1.78}$$

We can write the variation term $\Delta I_{13}(t)$ and $\Delta I_{23}(t)$ in term of the coefficients m. We find

$$\Delta I_{13}(t) = \frac{K^T(t) a^5 \Omega^2}{3G} m_1(t)[1 + m_3(t)]$$

$$\Delta I_{23}(t) = \frac{K^T(t) a^5 \Omega^2}{3G} m_2(t)[1 + m_3(t)] \qquad \textbf{1.79}$$

These are the changes induced in the product of inertia tensor $\Delta I_{13}(t)$ and $\Delta I_{23}(t)$ by the rotational deformation of the body. These change will be added to any changes due to surface or internal loads. We can now express the excitation function 1.41 in term of the different Love numbers. Assuming that $\vec{h} = 0$; $\dot{\vec{h}} = 0$; $\Delta\dot{I} = 0$ and a torque free situation the resulting excitation function due to rotational deformation will then be

$$\Psi^R(t) = \frac{\Delta I_{13}}{C-A} + i\frac{\Delta I_{23}}{C-A} = \frac{k^T(t)}{k_o} m(t) \qquad \textbf{1.80}$$

Where k_o is the secular Love number given by

$$k_o = 3G\frac{(C-A)}{a^5\Omega^2} \qquad \textbf{1.81}$$

and $m(t) = m_1(t) + im_2(t)$. The equation 1.40 of polar motion will then read

$$i\frac{\dot{m}(t)}{\sigma_r} + m(t) = \frac{k^T(t)}{k_o} m(t) \qquad \textbf{1.82}$$

To add the effect of a surface load, one would only need to add the excitation function of that load $\Psi^L(t)$, so that

$$i\frac{\dot{m}(t)}{\sigma_r} + m(t) = \frac{k^T(t)}{k_o} m(t) + \Psi^L(t) \qquad \textbf{1.83}$$

$$i\frac{\dot{m}(t)}{\sigma_r} + m(t)\left[1 - \frac{k^T(t)}{k_o}\right] = \Psi^L(t) \qquad \textbf{1.84}$$

This last equation is the polar motion equation in the time domain. Polar motion is thus a function of the tidal Love number, secular Love number and the excitation function of the

load. This form is convenient because all that is related to the load effect on rotation is contained uniquely inside the excitation function $\Psi^L(t)$. The situation, for any given load, can then be modeled more easily.

1.5.4 Changes in the inertia tensor due to rotational deformation

In this section we will look at the changes in the inertia tensor of a rotating planet due to rotational deformation. If we limit ourselves to degree 2 of the spherical harmonics expansion of the potential we can write the gravitational potential as follow [*Munk and Macdonald*, 1960]

$$V = \frac{GM}{r} + \Delta V_{gr} \qquad \textbf{1.85}$$

where ΔV_{gr} is given by

$$\Delta V_{gr} = \frac{G}{2r^5}\left[I_{11}\left(x_2^2 + x_3^2 - 2x_1^2\right) + I_{22}\left(x_3^2 + x_1^2 - 2x_2^2\right) + I_{33}\left(x_1^2 + x_2^2 - 2x_3^2\right) - 6I_{12}x_1x_2 - 6I_{13}x_1x_3 - 6I_{23}x_2x_3\right] \qquad \textbf{1.86}$$

The change in the gravitational potential ΔV_{gr} is equal to the product of the tidal Love number by the non-radial part of the centrifugal potential. The change in gravitational potential due to rotational deformation expressed in the last formula is equal to

$$\Delta V_{gr} = k^T\left[\frac{1}{6}\omega_1^2\left(x_2^2 + x_3^2 - 2x_1^2\right) + \frac{1}{6}\omega_2^2\left(x_1^2 + x_3^2 - 2x_2^2\right) + \frac{1}{6}\omega_3^2\left(x_1^2 + x_2^2 - 2x_3^2\right) - \omega_1\omega_2x_1x_2 - \omega_1\omega_3x_1x_3 - \omega_3\omega_2x_3x_2\right] \qquad \textbf{1.87}$$

Let's simplify immediately the last two formulas by placing the rotation vector along the x_3 axis, so that $\omega_1 = 0$, $\omega_2 = 0$ and $\omega_3 = \Omega$. Let's also assume that the planet is rotating

along it's principal axis, so that $I_{11} = A$, $I_{22} = B$ and $I_{33} = C$. The off diagonal moment of inertias (the product of inertia) will be 0 in this situation. By taking into account the simplifications of the last paragraph and equating the last two equations we get

$$\frac{G}{2r^5}\left[A\left(x_2^2 + x_3^2 - 2x_1^2\right) + B\left(x_3^2 + x_1^2 - 2x_2^2\right) + C\left(x_1^2 + x_2^2 - 2x_3^2\right)\right] = \frac{K^T}{6}\Omega\left(x_1^2 + x_2^2 - 2x_3^2\right) \qquad \textbf{1.88}$$

Dividing both sides of the last equation by the factor $G/2r^5$ and equating the terms of like coefficients in x_i^2 we get the following system of 3 equations with 3 unknowns

$$\begin{aligned} -2A + B + C &= M \\ A - 2B + C &= M \\ A + B - 2C &= M \end{aligned} \qquad \textbf{1.89}$$

where M is given by

$$M = k^T \frac{r^5\Omega^2}{3G} \qquad \textbf{1.90}$$

From the first two equations in 1.88 one immediately get $A = B$. With this information the third equation yield

$$C - A = M \qquad \textbf{1.91}$$

Let's add 3A on each side of the last equation, we get

$$C + 2A = M + 3A \qquad \textbf{1.92}$$

Let's define $I = \frac{A+B+C}{3} = \frac{2A+C}{3}$, the isotropic inertia value. Substituting in the last relation yield

$$3I = M + 3A$$

$$A = I - \frac{M}{3} = I - k^T \frac{r^5\Omega^2}{9G} \qquad \textbf{1.93}$$

We get a similar formula for the value of C in term of I. We get

$$C = I + k^T \frac{2r^5\Omega^2}{9G} \qquad \textbf{1.94}$$

In the long term limit the tidal Love number will be equal to the secular Love number k_o. If we now consider a point at the surface of the planet so that r = a, we finally get for A and C

$$A = I - k_o \frac{a^5\Omega^2}{9G}$$

$$\textbf{1.95}$$

$$C = I + k_o \frac{2a^5\Omega^2}{9G}$$

From these two formulas we can extract the value of the secular Love number k_o by subtracting A from C. We get

$$k_o = 3G\left[\frac{C-A}{a^5\Omega^2}\right] \qquad \textbf{1.96}$$

In the general case where the rotation vector is arbitrary, the inertia tensor of a rotationally deformed planet is [*Munck and Macdonald*, 1960]

$$I_{ij} = I\delta_{ij} + \frac{k^T a^5}{3G}\left[\omega_i\omega_j - \frac{1}{3}\omega^2\delta_{ij}\right] \qquad \textbf{1.97}$$

where a is the radius of the planet and δ_{ij} is the delta function which is equal to 1 if i = j and equal to 0 if i ≠ j. The expressions we have obtained for A and C can be readily derived from the last expression. The isotropic inertia tensor is defined as [*Lambeck* , 1980]

$$I = \frac{1}{3}\sum_{i=1}^{3} I_{ii} \qquad \textbf{1.98}$$

1.5.5 Change in the inertia tensor due to surface loading

The presence of internal or surface loads will also change the inertia tensor. If a mass load m appear suddenly at position x_1,x_2,x_3 the change in the inertia tensor of the planet will simply be the inertia tensor of the point mass. If one take compensation of the load into account, it can be described by a Dirac-Delta function $\delta(t)$ given by [*Ricard et al.*, 1993]

$$\int_{-\infty}^{+\infty}\delta(t)dt = 1 \text{ with } \delta(t) = 0 \text{ if } t \neq 0 \qquad \textbf{1.99}$$

The actual change in the inertia tensor will be [*Ricard et al.*, 1993]

$$J_{ij}(t) = \left(\delta(t) + k^L(t)\right)\Delta I_{ij}(t) \qquad \textbf{1.100}$$

Where $k^L(t)$ is the isostatic Love number of harmonic degree 2 and represent the effect of the compensation of the load. Consequently the total inertia tensor due to both rotational and load deformation will be

$$I_{ij} = I\delta_{ij} + \frac{k^T a^5}{3G}\left[\omega_i\omega_j - \frac{1}{3}\omega^2\delta_{ij}\right] + \left(\delta(t) + k^L(t)\right)\Delta I_{ij}(t) \qquad \textbf{1.101}$$

1.6 Quasi fluid approximation and the rotational number

One of the main disadvantages of the linear form of the Euler-Liouville equation of polar motion is that it is valid for only a small displacement of about 10 deg. Polar motion in terrestrial planets is likely to be much more important. To get a better portrait of long-term polar motion one must solve the non-linear Euler-Liouville equation, which is not an easy task. It is however possible to get a first order approximation of the long-term rotational behavior. As mentioned earlier, *Spada et al.* [1996] have devised a rotational number Ro that they claim can give a pretty good picture of long term polar motion based on the limit values (Ro >> 1 or Ro << 1) of that number. In the following section I will use some of the material developed above to introduce the rotational number Ro and discuss some of the implications of the value of that number for the long term polar motion of terrestrial planets. We have seen that the inertia tensor of a planet is dependant on the tidal and load Love numbers. In the Laplace domain the long-term values of those Love numbers are given by [*Ricard et al.*, 1993]

$$k^L(s) = k_f^L \qquad \textbf{1.102}$$

and

$$k^T(s) = k_f^T[1 - T_l s] \qquad \textbf{1.103}$$

Where T_l is a time constant define as

$$T_l = \frac{1}{k_f^T}\sum_{i=1}^{N}\frac{k_i^T}{s_i^2} \qquad \textbf{1.104}$$

T_l represent the time necessary for the equatorial bulge to readjust itself following a change in the rotation axis vector. See appendix B for a more detailed mathematical derivation of the last two expressions. This readjustment is necessary for polar motion to actually happen. This time is very sensitive to the viscosity stratification of the planet. On the other hand T_l is less sensitive to the density stratification [*SteifelHagen*, 2002]. Substituting the long term values of the Love numbers in the Laplace transform of the inertia tensor and then inverse transforming the relation to get back into the time domain one get the long term expression of the inertia tensor [*Ricard et al.* , 1993]

$$I_{ij} = I\delta_{ij} + \frac{k_f^T a^5}{3G}\left[\omega_i\omega_j - \frac{1}{3}\omega^2\delta_{ij}\right] - \frac{k_f^T T_l a^5}{3G}\left[\dot{\omega}_i\omega_j + \omega_i\dot{\omega}_j - \frac{2}{3}\omega\dot{\omega}\delta_{ij}\right] + \left(1 + k_f^L\right)\Delta I_{ij} \qquad \textbf{1.105}$$

Where the contribution from each term from left to right is of decreasing amplitude [*Ricard et al.*, 1993]. Substituting this last expression in the Euler-Liouville equation and assuming no external torque and that second derivatives and squares of derivatives are small we can express the different components of the rotation vector in a convenient matrix form [*Ricard et al.*, 1993]

$$A_{ij}(\omega,t)\dot{\omega}_j(t) + B_{ij}(\omega,t)\omega_j(t) = 0 \qquad \textbf{1.106}$$

Where A_{ij} and B_{ij} are matrices given by

$$A_{ij}(\omega,t) = \left[\frac{k_f^T T_l a^5}{3G}\right]\begin{bmatrix} \frac{3GI}{k_f^T T_l a^5} & \omega^2\omega_3 & -\omega^2\omega_2 \\ -\omega^2\omega_3 & \frac{3GI}{k_f^T T_l a^5} & \omega^2\omega_1 \\ \omega^2\omega_2 & -\omega^2\omega_1 & \frac{3GI}{k_f^T T_l a^5} \end{bmatrix} \qquad \textbf{1.107}$$

$$B_{ij}(\omega,t)=\left[1+k_f^L\right]\begin{bmatrix}\Delta\dot{I}_{11} & \sum_3(t) & -\sum_2(t)\\ -\sum_3(t) & \Delta\dot{I}_{22} & \sum_1(t)\\ \sum_2(t) & -\sum_1(t) & \Delta\dot{I}_{33}\end{bmatrix} \qquad \textbf{1.108}$$

where

$$\sum_k(t)=\sum_{i=1}^{3}\Delta I_{ki}\omega_i \qquad \textbf{1.109}$$

This is the Ricard matrix formulation. Now let's assume that the planet is initially rotating with a rotation vector aligned with the x_3 axis that is $\vec{\omega}=(0,0,\Omega)$. This is basically a description of the situation at t = 0. The last two matrices becomes

$$A_{ij}=\begin{bmatrix}I & (C-A)\Gamma_1\Omega & 0\\ -(C-A)\Gamma_1\Omega & I & 0\\ 0 & 0 & I\end{bmatrix} \qquad \textbf{1.110}$$

$$B_{ij}=\left[1+k_f^L\right]\begin{bmatrix}\Delta\dot{I}_{11} & \Delta I_{33}\Omega & -\Delta I_{23}\Omega\\ -\Delta I_{33}\Omega & \Delta\dot{I}_{22} & \Delta I_{13}\Omega\\ \Delta I_{23}\Omega & -\Delta I_{13}\Omega & \Delta\dot{I}_{33}\end{bmatrix} \qquad \textbf{1.111}$$

where (C-A) is given by equations 1.90 and 1.91. If we make the approximation that $k_f^T \approx k_o$ and replacing equations 1.110 and 1.111 in equation 1.106 we get three equations that will describe polar motion at t = 0. They are

$$
\begin{aligned}
&I\dot{\omega}_1 + (C-A)\Omega T_1\dot{\omega}_2 + \left(1+k_f^L\right)\left(\Delta\dot{I}_{11}\omega_1 + \Delta I_{33}\Omega\omega_2 - \Delta I_{23}\Omega^2\right) = 0 \\
&I\dot{\omega}_2 - (C-A)\Omega T_1\dot{\omega}_1 + \left(1+k_f^L\right)\left(-\Delta I_{33}\Omega\omega_1 + \Delta\dot{I}_{22}\omega_2 + \Delta I_{13}\Omega^2\right) = 0 \\
&I\dot{\omega}_3 + \left(1+k_f^L\right)\left(\Delta I_{23}\Omega\omega_1 - \Delta I_{13}\Omega\omega_2 + \Delta\dot{I}_{33}\Omega\right) = 0
\end{aligned}
\qquad \textbf{1.112}
$$

Now let's again consider the case where $\vec{\omega} = (0,0,\Omega)$. We define the complex number $\vartheta = \omega_1 + i\omega_2$ and consider the first two equations of 1.112. If we multiply the second one by the complex factor *i* and add the result to the first equation we get

$$
\dot{\vartheta} = \frac{\left(1+k_f^L\right)\Omega^2\left[\Delta I_{23} - i\Delta I_{13}\right]}{\left[I - i(C-A)T_1\Omega\right]} \qquad \textbf{1.113}
$$

A few more algebraic steps will transform this last equation to the following form

$$
\dot{\vartheta} = \frac{\Omega}{1+\left[\frac{Ii}{(C-A)T_1\Omega}\right]} \frac{\left(1+k_f^L\right)\left[\Delta I_{13} + i\Delta I_{23}\right]}{(C-A)T_1} \qquad \textbf{1.114}
$$

This is the polar motion equation. Now following *Spada et al.* [1996], we define the rotational number R_o as

$$
R_o = \Omega\frac{T_1 J_2}{I^*} \qquad \textbf{1.115}
$$

Where J_2 is the dynamical flatness and I* is the normalized mean moment of inertia given by

$$
J_2 = \frac{(C-A)}{Ma^2} \qquad \textbf{1.116}
$$

$$I^* = \frac{I}{Ma^2}$$

so that

$$R_0 = \Omega \frac{T_1(C-A)}{I} \rightarrow R_0 I = T_1(C-A)\Omega \qquad \textbf{1.117}$$

Now substituting this into the polar motion equation 1.113 and integrating we finally get

$$\vartheta = \frac{\Omega}{1+\left[\frac{i}{R_0}\right]} \frac{\left(1+k_f^L\right)}{(C-A)T_1} \int_0^t [\Delta I_{13} + i\Delta I_{23}]dt \qquad \textbf{1.118}$$

This last expression is basically equation 1 of *Spada et al.* [1996]. Transforming the first term of the last expression as to express it in the form $a+ib$ to clearly separate the real and imaginary part we get

$$\vartheta = \Omega\left(\frac{R_o^2}{R_o^2+1} - i\frac{R_o}{R_o^2+1}\right) \frac{\left(1+k_f^L\right)}{(C-A)T_1} \int_0^t (\Delta I_{13} + i\Delta I_{23})dt \qquad \textbf{1.119}$$

One can immediately see in this last equation that if the inertia perturbation is in the equatorial plane ($x_3 = 0$) or at the pole ($x_1 = 0$, $x_2 = 0$), that is on the axis of rotation, then no polar motion will be created by the perturbation. Note that the situation is perfectly symmetrical and one would only have to change ΔI_{13} for ΔI_{23} to get identical result if the inertia perturbation was in the x_1x_3 plane instead of the x_2x_3 plane [*L.L.A Vermeeseen, personal communication*]. It is also quite clear from the last equation that if the load is completely compensated, that is if $1+k_f^L = 0$ then there is no polar motion possible. Other reasonable assumptions not mentioned in *Ricard et al.* [1993] and *Spada et al.* [1996] are needed to obtain the last result.

One of the main problem with the rotational number R_o is that it cannot be precisely evaluated because most planetary interior structures are poorly known. A more rigorous derivation of this last equation, bypassing the Ricard formulation used above, and using directly the Euler-Liouville equation will be given in appendix A. This appendix will show that the Ricard formulation is merely a more convenient way of presenting the mathematics leading to the polar motion equation and is not needed to describe the physics of polar motion. Appendix B will go a step further and show a much simpler derivation of the last equation using the linear polar motion equation in the Laplace domain. Appendix A and B clearly shows the overall correctness of the long-term behavior of the rotational number as described by *Spada et al.* [1996] but the complex mathematical derivation outlined in the previous sections and in *Ricard et al.* [1993] and *SteifelHagen* [2002] are simply not necessary and in many ways too complex with a tendency to hide some simple physical characteristics of the phenomenon behind a mountain of mathematics.

1.7 Long-term limits of the rotational number

One of the main interest of the rotational number R_o is what it tell us for extreme values. Two cases can be considered.

1.7.1 Ro >> 1

First let's consider a constant inertia perturbation in the x_2x_3 plane (the situation is symmetrical for the x_1x_3 plane) then the integral in the polar motion equation becomes

$$\int_0^t (\Delta I_{13} + i\Delta I_{23})dt = i\,\Delta I_{23} \qquad \textbf{1.120}$$

so that the polar motion equation 1.119 becomes

$$\vartheta = \Omega\left(\frac{R_o}{R_o^2+1} + \frac{iR_o^2}{R_o^2+1}\right)\frac{\left(1+k_f^L\right)}{(C-A)T_l}\Delta I_{23} \qquad \textbf{1.121}$$

In the case where $R_o >> 1$ we have

$$\frac{R_o}{R_o^2+1} \approx 0$$
$$\frac{R_o^2}{R_o^2+1} \approx 1 \qquad \textbf{1.122}$$

We see that in this case there is only a component of $\vec{\omega}$ in the x_2 plane, therefore the inertia perturbation will go directly to the pole in the case where $\Delta I_{23} < 0$ and to the equator if $\Delta I_{23} > 0$. This result is consistent with the simple rigid body behavior example given earlier in this thesis. *Spada* [1992] has proposed the following analytical solution for the simple case described in this section. The change in colatitude of the axis of rotation for a load placed in the x_2x_3 plane is given by

$$\tan(\theta(t)) = \frac{2\tan(\alpha)\sinh(\beta t)}{\left(1-\tan^2(\alpha)\right)\sinh(\beta t) - \left(1+\tan^2(\alpha)\right)\cosh(\beta t)} \qquad \textbf{1.123}$$

where α is the initial colatitude of the load and β is given by

$$\beta = \frac{3Gm(a-d)^2\left(1+k_f^L\right)}{2k_f^T T_l a^5 \Omega^2} \qquad \textbf{1.124}$$

where *m* is the mass of the load, *a* the radius of the planet and *d* the depth of the load. Now if we consider a load at the surface (d = 0) and express the factor β in term of the rotational number R_o we get

$$\beta = \frac{m\left(1+k_f^L\right)\Omega}{2R_o I^* M} \qquad 1.125$$

where M is the mass of the planet and I* the moment of inertia factor.

1.7.2 Ro << 1

Now if we consider the case where $R_o << 1$ we have a situation that is basically the opposite of what we obtained above, that is

$$\frac{R_o}{R_o^2+1} \approx R_o$$
$$\frac{R_o^2}{R_o^2+1} \approx 0 \qquad 1.126$$

In this case the x_1 component of $\vec{\omega}$ is non-zero indicating that the inertia perturbation will start to move at right angle with the x_2x_3 plane. This will result in what *Spada et al.* [1996] call a mega wobble. In this situation the inertia perturbation will reach the pole (or the equator) in a spiraling movement of decreasing amplitude. However, to verify this affirmation and compute a complete polar motion path one must solve the full set of equations 1.106 to 1.108, not the simplified version exposed in this section which basically represent only the situation at t = 0.

Spada et al. [1996] have evaluated approximate values for the rotational number for the Earth, Mars and Venus based on models of the interior structure of the three planets. They concluded that the Earth and Mars must have a high value of Ro for most reasonable models. On the other hand, Venus with it's small angular velocity and flattening has a low value of Ro. Earth and Mars belong to the same rotational category where True polar wander (TPW) is possible and that Venus would belong to another

category where the load would go to the equator (or pole for a mass deficit) via mega wobble.

Despite the fact that the Earth and Mars belong to the same category, the mechanism responsible for polar motion in the two planets is very different. In the case of Mars surface loading would be mainly responsible for polar motion. This would make Mars much closer to the simple rigid body model discussed earlier and would constitute an argument for a much more rigid Martian interior. In the case of the Earth, the changes in internal density distribution due to convection have a more important contribution than surface loading.

1.7.3 Offset between spin axis and maximum inertia axis

In section 1.2 I have shown that a body will be rotationally stable if it's rotation axis align with the axis of maximum inertia. This will be the case if the I_{13} and I_{23} components of the inertia tensor are 0 in equation 1.105 [*Spada et al. 1996b*]. If not, there will be a non-zero angle (offset) between the two axes. This offset can be evaluated in term of the rotational number Ro. First by using equations 1.105 and 1.118 one can get a relationship between I_{13}, I_{23} and Ro. We find

$$I_{13} = \frac{R_o\left(1+k_f^L\right)}{R_o^2+1}\left[\frac{\Delta I_{13}}{R_o} - \Delta I_{23}\right]$$
$$I_{23} = \frac{R_o\left(1+k_f^L\right)}{R_o^2+1}\left[\frac{\Delta I_{23}}{R_o} + \Delta I_{13}\right] \qquad \textbf{1.127}$$

One can see from the last equation that if Ro >> 1 than I_{13} and I_{23} will be small and therefore the axis of rotation will almost coincide with the axis of main inertia. The opposite is true for Ro << 1. Using 1.127 *Spada et al.* [*1996b*] have proposed the following value for the offset between the two axes

$$\tan(\varepsilon) = \frac{\left(1 + k_f^L\right)}{J_2 Ma^2} \sqrt{\frac{\Delta I_{13}^2 + \Delta I_{23}^2}{R_o^2 + 1}} \qquad 1.128$$

In the case of Venus, a planet with low R_o value, the offset between the two axes was first reported after preliminary analysis of the gravity field. However, the amplitude of the offset has decreased with every increase in the resolution of the gravity field. A robust measure of this offset would go a long way into making *Spada et al.*, [1996] rotational number theory more acceptable, since, as shown above, a low Ro value imply a non zero offset value.

Figure 1.3 is a diagram that summaries the different calculations made in this chapter and in appendix A and B. It present graphically the most important equations of this chapter.

1.8 Influence of internal structure parameters

In this section I want to discuss the general influence on polar motion of some important internal structure parameters. These parameters include lithospheric thickness, rigidity and viscosity profiles of both the lithosphere and the mantle. The general effect of compensation is also discussed.

1.8.1 Influence of load compensation

For non-rigid bodies the possibility of load compensation is one of the most fundamental difference with rigid bodies. A load put at the surface of such non-rigid body will try to sink into the lithosphere until compensated. This situation is perfectly analogous to the one observed for an iceberg at the surface of the ocean. Compensation will reduce the contribution of a load to polar motion by bringing the load closer to the axis of rotation. This will reduce the effect of the load on the change in the inertia tensor due to the load itself. *Ricard et al.* [1992] strongly argue for taking into consideration the chemical and viscosity structure of the mantle when modeling the effect of an internal mass anomaly

on the amount and direction of polar motion. The depth and compensation state of the anomalous mass are of prime importance. For example an anomalous mass near a chemical interface could have no long time effect on polar wandering due to complete compensation. It is clear that to truly evaluate the influence of a load to polar motion one must know the state of compensation of that load.

Since compensation plays such crucial role it is worth investigating the general state of compensation of Martian topography and Tharsis in particular. Any mass excess or deficit at the surface can, in theory, drive polar motion. Due to the fact that surface topography of a terrestrial planet is supported by forces in the outer layers of the body, short wavelength topography is less likely to be compensated than long wavelength one [*Mackenzie et al.*, 2002]. Topographic features that do not correlate with geoid anomalies are thought to be old and compensated. This could mean that, young, short wavelength topography like volcanoes which shows big gravity anomalies have more influence on polar wandering than Tharsis as a whole if Tharsis is compensated. *Sphon et al.* [2001] argues that gravity high over the Tharsis and Elysium volcanoes indicate that these constructs are not compensated and would therefore continue to drive polar wandering even to this day. In a similar way *Arkani-Hamed* [2000] argue that intermediate scale topography is not significantly compensated. This topography would include most volcanoes and some impact basins. He also argues that significant mass anomalies must exist beneath the shield volcanoes of the Tharsis bulge. His argument is based on the fact that thin shell modeling alone cannot represent adequately the observed topography and gravity signal for those volcanoes. One can conclude from this that the Martian lithosphere must be very strong to support both topography and internal loads.

Large impact basins, however, are thought to be compensated [*Mackenzie et al.*, 2002 ; *Arkani-Hamed*, 2000] and therefore would not be a major factor in polar motion. The same observation can be made for the northern lowlands, which do not display significant geoid or gravity anomalies

It also seems likely that Tharsis is not fully compensated. Many models of Tharsis have been proposed. *Willemann and Turcotte* [1982] modeled the Tharsis rise as a downward load on an elastic lithosphere. They came to the conclusion that Tharsis is only partially compensated and result from surface loading by early volcanic activity. They found no evidence for lithospheric doming that would be the signature of a mantle plume beneath Tharsis. *Zuber at al.* [1998] argue that Tharsis cannot be fully compensated by modeling the COM/COF difference in the extreme cases of full compensation and no compensation at all. A fully compensated Tharsis would make a COM/COF shift minimum, much lower than what is actually observed. This modeling support the hypothesis that Tharsis is not fully compensated and therefore remain a prime contributor to polar motion on Mars.

1.8.2 Influence of lithospheric thickness

It is widely acknowledged that most terrestrial bodies of reasonable size have an outside layer called lithosphere. The lithosphere is the part of the body that can withstand stress for time periods that are consistent with geological evolution [*Arkani-Hamed*, 2000]. The thickness of the lithosphere and its material properties can have a considerable impact on the total amount of polar wandering experienced by a planetary body.

First, let's consider lithospheric thickness. A thick lithosphere will oppose more resistance to the tendency of any surface load to sink into it. That is, a thick lithosphere will be more capable to resist compensation and therefore a load on a thick lithosphere is less likely to be compensated. An uncompensated mass will remain farther away from the axis of rotation and consequently impose a bigger change to the inertia tensor of the planet. Therefore a planet with a thicker lithosphere will experience more polar wandering.

SteifelHagen [2002] has modeled the influence of lithospheric thickness on polar wander by using different surface loads on a given planetary interior model. He found that for

short-term perturbation polar wandering increase linearly with increasing lithospheric thickness. For larger perturbation time a logarithmic relationship seems to be more appropriate and concluded that lithospheric thickness plays a role not only in the total amount of polar motion a planetary body experience but also in the way polar motion evolve with time.

The removal of surface loads will also have an effect on polar motion as the lithosphere and mantle under it are then allowed to rebound to their former position after the removal of the load. The load removal process and the actual movement of the lithosphere are mass movements that influence the inertia tensor of a planet and therefore influence polar motion. On Earth it is thought that the actual observed polar motion is mainly due to postglacial rebound after the removal of the different ice sheets formed during the last ice age. [*Ricard et al.*, 1992].

On Mars, *Zuber et al.* [2000] have studied the global structure of the crust and lithosphere by using the latest topography and gravity data from MGS. They argue that observed Bouguer gravity is best explained by a crust of uniform density and varying thickness. The crust has an average thickness of 50 km and represent 4.4% of the total volume of Mars. They argue that a thicker average crust would not be sustainable over long period of time. To first order, crustal thickness correlate with topography. The crustal structure shows a progressive thinning of the crust from south to north. In the Tharsis province itself the crustal and lithospheric thickness shows some variability but are on average much higher than the Martian average. The changes in the crustal thickness in the Tharsis province support a volcanic origin (surface loading) of the province and the thickness of the lithosphere under Tharsis, a younger age for the construct. all of this is consistent with a non-compensated Tharsis that would be a major contributor to polar motion. The crust is unlikely to have been recycled like here on Earth and is mostly primary crust formed early in Martian history [*Wieczorek and Zuber*, 2004]. See *Wieczorek and Zuber* [2004] for a complete review and critique of the different techniques for crustal thickness estimation.

1.8.3 Influence of the internal viscosity profile

One fundamental property of any deformable material is his viscosity. Viscosity is the resistance of a material to a change in form. This can be seen as internal friction between the different parts of the body. The amount of compensation of a load depend on the viscosity. If viscosity is high then the body will stay closer to the surface. One would then expect a body to experience more polar motion if it has a highly viscous lithosphere. However one must also look at viscosity from another angle to get a more complete picture of the influence of this parameter. The way a planet deform as a whole is also important . When polar motion occurs the new axis of rotation is not perpendicular to the old equatorial bulge of the planet. In order to attain rotational equilibrium the planet will try to realign it's equatorial bulge so that it becomes perpendicular to the new rotation axis. The time it takes to make that realignment is determine by the time T_1 in Spada's notation as defined by equation 1.104. This time is greatly dependant on the viscosity of the mantle. The lower the viscosity, the easier it will be for the planet to realign it's equatorial bulge. In the extreme case of a rigid body where the bulge cannot be realigned there cannot be any polar wander.

We see that the effect of viscosity changes when we consider the effect of this parameter on the state of compensation of a load or when we consider it as a mantle property. The two processes act one against the other and the exact influence of viscosity can only be determined through modeling of realistic values of the parameter. *Steifelhagen* [2002] has found that polar wandering decreases linearly with an increase in viscosity.

1.8.4 Influence of rigidity on polar wandering

Rigidity is another important property of deformable body. It relates stress to strain as in the classical Hooke law of elasticity. However, *SteifelHagen* [2002] has found that the time scale T_1 does not depend much on rigidity and has concluded that for most situations

the rigidity factor has much less influence on polar wandering than the viscosity parameter.

Figure 1.1

A high-resolution view of the topography of the north pole of Mars. A circular, swirling terrain is clearly visible around the present day rotation axis. At 0° longitude there is another formation (shown by the arrow) very similar to the one at the actual pole. This led *Murry and Malin* [1973] to suggest that this formation is an ancient pole of Mars and thus that Mars experienced polar wandering of 10 to 15°. Topography data is from MGS MOLA instrument.

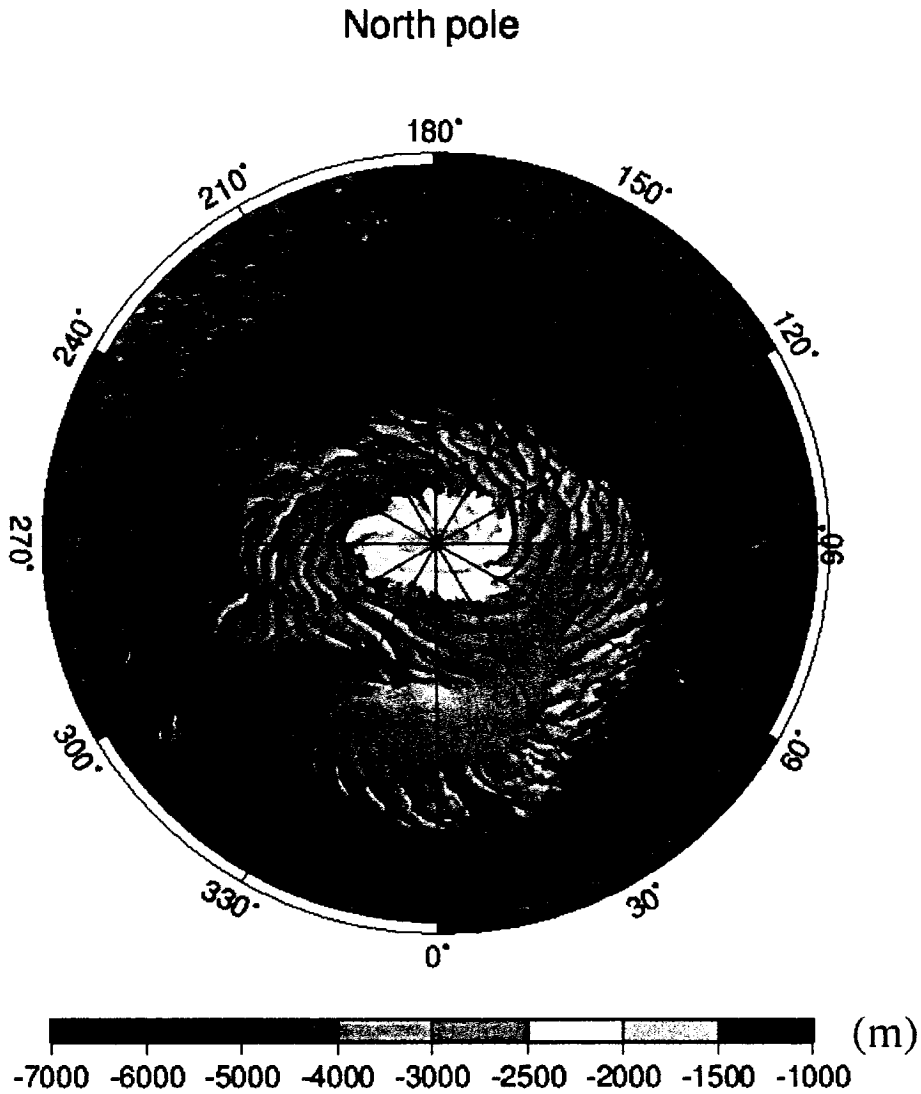
North pole
180°
150°
120°
90°
60°
30°
0°
330°
300°
270°
240°
210°
(m)
-7000 -6000 -5000 -4000 -3000 -2500 -2000 -1500 -1000

Figure 1.1

Figure 1.2

Calculation of the angular momentum of a mass element dm.

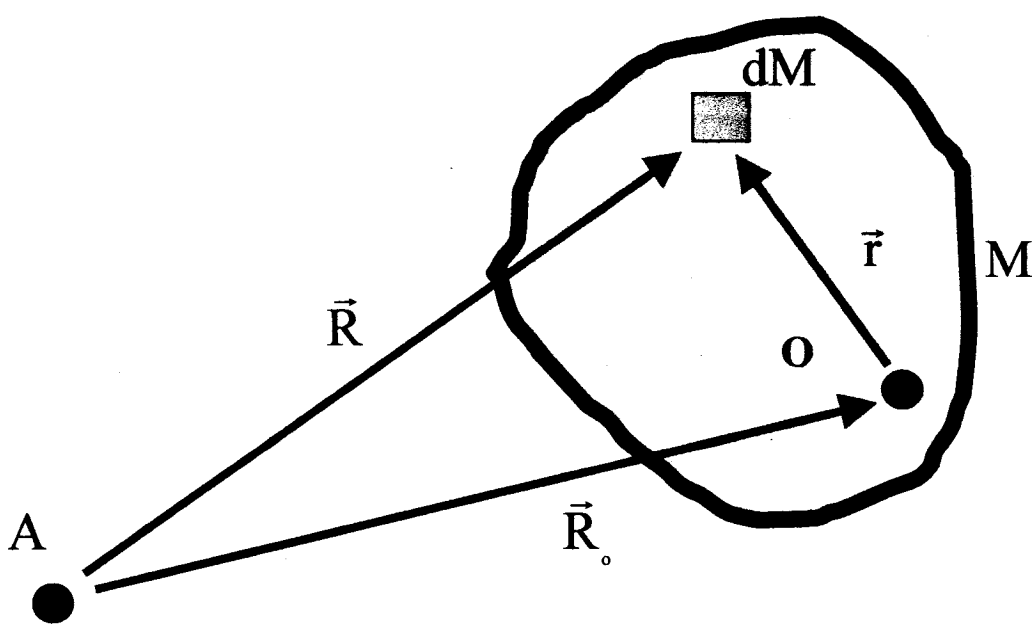

Figure 1.2

Figure 1.3

A summary of this chapter. Arrows indicate the logical path from one formula to the other. Red arrows are concerned with the linear formulation of the Euler-Liouville equation. Blue arrows are concerned with the long-term approximation of the polar motion equation.

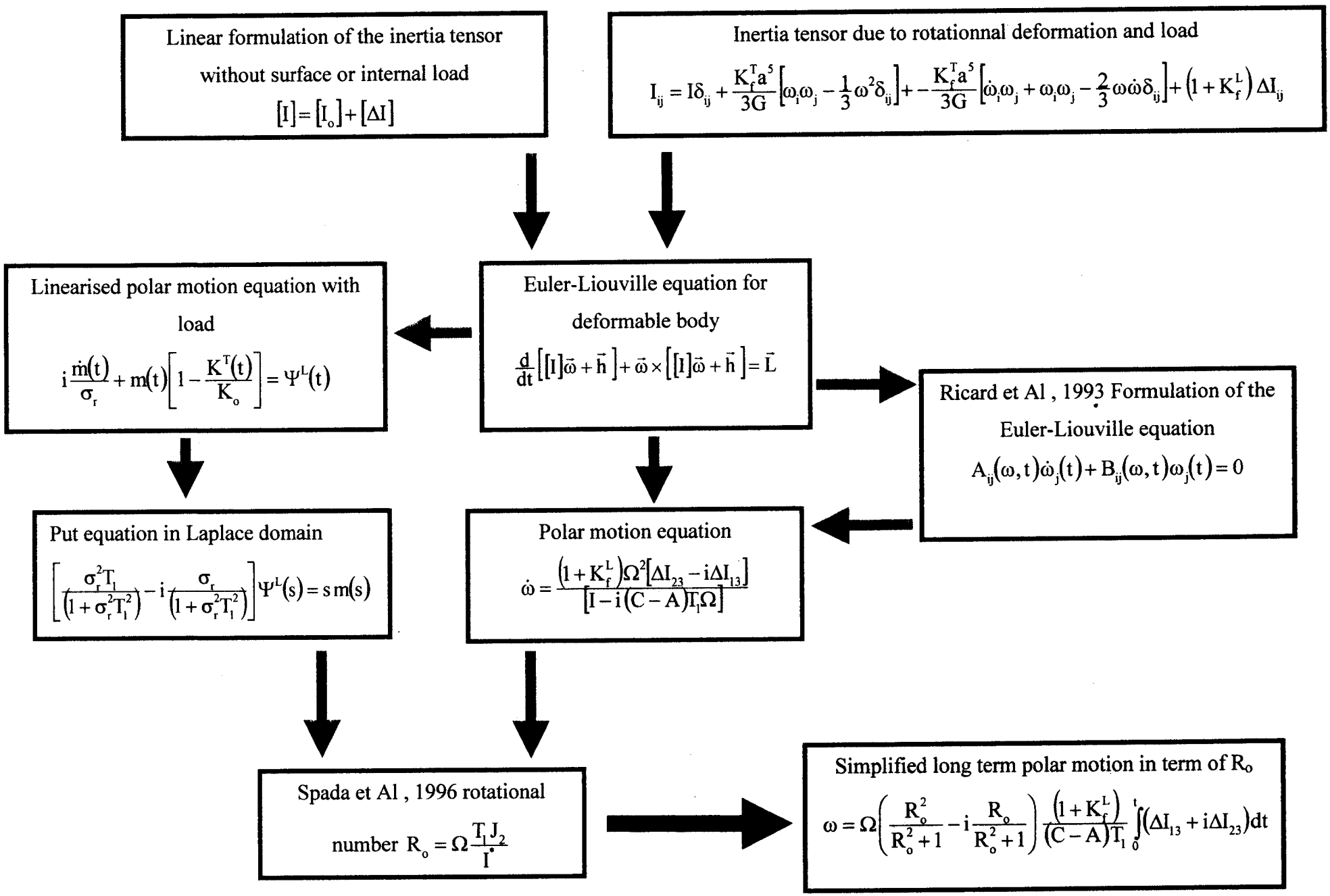
Linear formulation of the inertia tensor without surface or internal load
$[I]=[I_o]+[\Delta I]$
Inertia tensor due to rotationnal deformation and load
$I_{ij}=I\delta_{ij}+\frac{K_f^T a^5}{3G}\left[\omega_i\omega_j-\frac{1}{3}\omega^2\delta_{ij}\right]+-\frac{K_f^T a^5}{3G}\left[\dot{\omega}_i\omega_j+\omega_i\omega_j-\frac{2}{3}\omega\dot{\omega}\delta_{ij}\right]+\left(1+K_f^L\right)\Delta I_{ij}$
Linearised polar motion equation with load
$i\frac{\dot{m}(t)}{\sigma_r}+m(t)\left[1-\frac{K^T(t)}{K_o}\right]=\Psi^L(t)$
Euler-Liouville equation for deformable body
$\frac{d}{dt}\left[[I]\vec{\omega}+\vec{h}\right]+\vec{\omega}\times\left[[I]\vec{\omega}+\vec{h}\right]=\vec{L}$
Ricard et Al , 1993 Formulation of the Euler-Liouville equation
$A_{ij}(\omega,t)\dot{\omega}_j(t)+B_{ij}(\omega,t)\omega_j(t)=0$
Put equation in Laplace domain
$\left[\frac{\sigma_r^2 T_1}{\left(1+\sigma_r^2 T_1^2\right)}-i\frac{\sigma_r}{\left(1+\sigma_r^2 T_1^2\right)}\right]\Psi^L(s)=s\,m(s)$
Polar motion equation
$\dot{\omega}=\frac{\left(1+K_f^L\right)\Omega^2\left[\Delta I_{23}-i\Delta I_{13}\right]}{\left[I-i(C-A)T_1\Omega\right]}$
Spada et Al , 1996 rotational number $R_o=\Omega\frac{T_1 J_2}{I^*}$
Simplified long term polar motion in term of R_o
$\omega=\Omega\left(\frac{R_o^2}{R_o^2+1}-i\frac{R_o}{R_o^2+1}\right)\frac{\left(1+K_f^L\right)}{(C-A)T_1}\int_0^t\left(\Delta I_{13}+i\Delta I_{23}\right)dt$

Chapter 2 : The magnetic field of Mars

2.1 Introduction

Chapter 1 discussed the rotational dynamics of non-rigid planets. Despite the importance of the subject and the extensiveness of our discussion, rotational dynamics is not the main subject of this thesis. Now that the physical basis of polar wandering is set I would like to use paleomagnetism to verify if indeed Mars was ever subjected to polar wandering. More precisely I will use the recently discovered magnetic anomalies on Mars to try to find the orientation of the ancient dipolar core field that is assumed to have created these anomalies. The modeling of the magnetic field will also be discussed. On Earth paleomagnetism seeks to study the intensity and orientation of the Earth's magnetic field throughout history. Paleomagnetic studies are typically used to study the movement of continents with respect to the axis of rotation. A rock can get magnetized either through induced magnetization or remnant magnetization. Induced magnetization is created when an external field acts on a rock. The rock develops a magnetization given by

$$J = \chi H$$

Where H is the external field and χ is the magnetic susceptibility of the rock. For an isotropic rock χ is a scalar and the magnetization vector is parallel to the applied field. For some rocks, however, there is magnetic anisotropy and the magnetization is not in the same direction as the applied field. In this situation χ is a tensor (3 x 3 matrix). In the case of induced magnetization, the magnetization disappears when the applied field disappears.

Other types of rocks have remnant magnetization. Remnant magnetization is basically a permanent recording of an ancient field that acted on the material. In the case of Mars, there is no global, Earth like, field and the observed magnetic field is crustal in origin and is created by remnant magnetization. When a magnetic material temperature goes below a certain point (the

Curie temperature) it will be magnetized by the core field of the Earth. On Mars the most likely candidates minerals to produce the observed magnetization are ferromagnetic minerals like magnetite and hematite that have a high Curie temperature of 580 and 675° C [*Dunlop and Arkani-Hamed*, 2004]. Assuming that the orientation of the dipole core field is the same as the rotation axis then the measured field orientation provide the orientation of the axis of rotation.

The fundamental hypothesis of geomagnetism is the geocentric axial dipole hypothesis (GAD). It is mentioned numerous times in this thesis. In this hypothesis the magnetic field of the Earth is produced by a simple magnetic dipole at the center of the Earth. This dipole is aligned with the axis of rotation and produces the dipolar component of the geomagnetic field. At the present time, the observed geomagnetic field is not exactly aligned with the axis of rotation but is slightly inclined with an angle of 11.5° with respect to axis of rotation. This is the inclined geocentric dipole. It is also possible to model the geomagnetic field with a dipole that is not at the center of the Earth, this is the eccentric dipole. The fit obtained, however, is only marginally better [*Butler*, 1992] and the geocentric dipole hypothesis is retained

The geomagnetic poles produced by the inclined geocentric dipole do not correspond with the actual magnetic poles as would be the case if the field was uniquely dipolar in origin. This is caused by another component of the geomagnetic field ; the non-dipolar component. The total geomagnetic field is thus the sum of the dipolar and non-dipolar component. Modeling of the non-dipolar component suggests an origin in the fluid eddy current in the liquid outer core of the Earth.

The geomagnetic field has not been constant during most of the history of the Earth. The field has changed its intensity and orientation. There is also evidence of complete polarity reversal where the dipole orientation has shifted 180°. During that time both components of the field have changed. The dipolar component changes are long period changes and the non-dipolar component changes more quickly. For the past 2000 years, on average, the geomagnetic pole is close to the axis of rotation This mean that, on geological time scale, The orientation of the dipole field has been, on average, the same as the axis of rotation of the Earth. Clearly the rotation of the Earth

must have an effect on fluid motion in the liquid outer core and it is therefore logical to assume a strong link between rotation and geomagnetic field. This is the most fundamental element of the GAD and the basis of the uses of magnetic anomalies to study polar wandering on Mars. The alignment of the dipolar field with the rotational axis is also observed in the case of Mercury [*Wang* ,1977]. On Earth the situation is complicated by the presence of plate tectonics, which, in addition to polar motion move the position of a given point relative to the axis of rotation of the planet. On Mars the situation is much simpler (although this last comment does not mean at all that the situation is simple !!!!). Mars has no global field and is considered a one-plate planet with no plate tectonic as we know it here on Earth.

The lack of global field is a blessing as the observed field is predominantly crustal in origin [*Purucker*, 2000]. Relatively well-isolated anomalies can be used to infer the orientation of the ancient core field at the time of magnetization and assuming that the field axis was aligned with the axis of rotation we can estimate the movement of the surface relative to the axis of rotation that is polar motion. Loosely defined, a magnetic anomaly is simply a portion of the magnetic map with values that differ significantly from the immediate surrounding. See figure 2.1 for examples of magnetic fields produced by different bodies. The challenges in modeling magnetic anomalies are many, most notably in the choosing of a suitable anomaly and the removing of exterior and nearby contamination. How those problems were handled will be explained in detail in this chapter.

2.2 The MGS data

The data used in the modeling done in this thesis is provided by Mars Global surveyor (MGS). The magnetometer onboard MGS has provided magnetic field measurements at low (from 80 km to about 200km) altitude during the SPO1 (Science Phasing Orbit) and SPO2 phases of the mission. Higher altitude data, at an average 400 km altitude, were provided during the MO (Mapping Orbit) phase of the mission. The high altitude data have very dense coverage on almost the entire surface of the planet but suffer from low resolution due to altitude. The data, as provided by NASA, are along satellite tracks. Each measurement is identified by a time stamp. In

this manner each track can be separated from the global data set. It is thus possible to study the data globally or each track individually or one can also look at a combination of both regional data and track data. Unfortunately the low altitude data are very sparse and one cannot expect more than just a few good tracks over individual anomalies. Data can also be divided into two groups depending if the measurement was made during the day or during the night. This is especially important for any study using magnetic data. See figure 2.2 for a global portrait of the Martian night side high altitude magnetic field.

The major challenge for any study using MGS data is to find an acceptable way to remove noise and other contamination from the data. This study is no exception. The contamination can be globally classified into 2 groups. First there is contamination of the data by external sources. Interaction of the solar wind with the Martian ionosphere produce parasite magnetic fields that contaminate the data. This is especially true for the high altitude data that sits above the ionosphere, which has been conservatively set at 200 km altitude [*Acuna et al.*, 1998]. At altitude higher than that, dayside data is especially vulnerable. Since there is no reliable model of the ionosphere-solar wind interaction, it is extremely difficult to assess the level of contamination of the high altitude dayside data. For this reason only night side data are considered in this thesis. This help reduce, but not eliminate, outside contamination. See figures 2.3 and 2.4 for examples of high altitude data contamination.

Unfortunately low altitude data are dayside and are more likely to be contaminated even though the data are below the ionosphere. The effect of the external sources on low altitude data is likely to be less severe than on the high altitude data because of the strong nature of the crustal anomalies at lower altitude. Once again getting a good portrait of the contamination is extremely difficult and subjective.

For a given anomaly the other source of contamination is simply the presence of other sources nearby. The measured magnetic field is thus the vector sum of all magnetic fields from all the nearby sources. This contamination is by far the most difficult to remove because of the fundamental non-uniqueness associated with this situation. To get a precise pole position out of a

magnetic anomaly model one would need a perfectly isolated source body. Such anomalies simply do not exist. On Mars, the requirement of an isolated magnetic anomaly precludes any use of the southern hemisphere highly magnetic parts. All the anomalies in this study are at diverse degree affected by this contamination. See figure 4.8 and table 4.3 for an example of the effect of contamination by a nearby source. Figure 2.5 gives the result of a numerical experiment where 20 dipole sources were put on sphere and the three components of the magnetic field are calculated over the entire sphere.

2.3 The Martian magnetic field

It has been established that the observed magnetic field is crustal in origin. This is one of the rare observation of Mars that is very robust and has not been seriously challenged. The strongest anomalies are observed over Terra Cimmeria and Terra Sirenum in the southern hemisphere. The northern hemisphere is largely devoid of magnetic anomalies. With the topographic dichotomy this is another major difference between the two hemispheres of the planet.

To explain such a difference one can invoke many scenarios, most of them related to the formation of the hemispheric dichotomy. Many investigators have assumed that the northern plains are younger than the southern highlands because of the almost total absence of large crater in the northern plains. It is then plausible to imagine that the northern plains formed after the cessation of the core field early in Martian history. However the difference in age has been disputed and it has been proposed that the base of the northern plains is about the same age as the southern highlands and that only the first few kilometers of volcanic layers are actually young [*Wieczorek and Zuber*, 2004]. This argument is supported by studies that indicate that the hemispheric dichotomy is not a fundamental feature of the planet's internal structure [*Zuber et al.*, 2000]. It has also been argued that the hemispheric dichotomy does not translate into a crustal thickness dichotomy even thought some studies predict a thinning of the crust under the northern hemisphere [*Zuber et al.*, 2000]. Evolution models have also pointed out that the Martian crust was formed very early in Martian history and is probably primary in origin [*Wieczorek and*

Zuber, 2004]. All these points argue against a difference in magnetization due to a difference in age.

Another plausible scenario is a very different mineralogical composition in the northern hemisphere. But again based on evolution models this is unlikely if one assume about the same age for both the southern highlands and northern plains. Most models of crustal thickness assume a constant density crust implying a more or less similar composition. While this is certainly a very crude first order approximation there is no evidence of a dramatic difference in composition between the northern plains and southern highlands. If the northern plains are contemporary with the southern highlands and the crust on average of the same composition, then they should have been equally magnetized by the ancient core field. Assuming this, then one is put into the unviable position of invoking a mechanism that would explain the demagnetization of the northern lowlands. Again many scenarios are possible. Thermal evolution models have hinted that the northern hemisphere might have been the locus of high heat loss by conduction early in Martian history [*Sphon et al.*, 2001]. The hotter lithosphere would make magnetic material loose their magnetization as they are heated above their curie point. It is however unlikely that any plausible mechanism would demagnetize the crust all the way to the surface. So some magnetization should remain.

Another possible demagnetization scenario is the impact scenario. It has been argued that the topography dichotomy itself might have been formed by the giant impact that created the Utopia basin [*Zuber et al.*, 2000]. Such an impact would have excavated a good portion of the lithosphere and easily heated the impact point and the surroundings well above the Curie point. Big impact basins on Mars do not show significant magnetic anomalies. However it is difficult to imagine how a single impact, even one of the magnitude that created Utopia, can demagnetized most of the northern hemisphere. *Mohit and Arkani-Hamed* [2004] have studied the effect of shock pressure and impact heating on demagnetization. They concluded that the crust is totally demagnetized within 0.8 basin radius of the impact site and partially demagnetized up to 1.4 basin radius of the impact site. Assuming that this value apply to a very big impact it still leave us well short of an entire demagnetized lowlands.

One other observation of interest is that there seems to be no correlation between topography and the observed magnetic anomalies. Recently, *Langlais et al.* [2003] have hinted of a possible correlation between certain craters and some magnetic anomalies but the evidence is not convincing. No such correlation have been observed in this thesis even for well isolated anomalies. See appendix D for topography maps of the regions under the anomalies studied in this thesis. One must remember that, depending on magnetization, the maximum of an anomaly may not appear directly over the source, thus complicating any search for a link between topography and magnetic source. Moreover the observed magnetic field is more likely the vector sum of many fields created by many sources. Add to this the lost of resolution for the high altitude data and the task of finding any correlation is next to impossible with the presently available data. Global low altitude data coverage would help a lot in this situation. Of course, this correlation might not exist in the first place, indicating that source bodies are situated deep in the crust of Mars.

2.4 Modeling the Martian magnetic field

The Martian magnetic field has been extensively modeled. Many spherical harmonics models have been proposed. *Arkani-Hamed* [2001] has shown a 50 degree and order model elaborated by using the three components of the low altitude data from 80 km to 200 km altitude. *Cain et al.* [2003] have used both the low and high altitude data to produce a 90 degree and order model. Higher degree and order is always desirable in a model, however the higher harmonics are more susceptible to noise. Cain's model does represent well only the high altitude data with disagreement with other published models of several hundreds nT for the low altitude data. Moreover the noise in the higher harmonics is amplified when the model is downward continued to lower altitude making this operation very risky. These two models used day side data, which is more susceptible to contamination, especially for the horizontal components of the data.

Purucker et al. [2000] used the equivalent source dipole technique to model the radial component of the low altitude data available at that time. They produced an altitude normalized map of the

radial component at 200 km altitude. From this model they concluded that the magnetic field was crustal in origin. However, some large misfit between data and model remained and were attributed to external field contributions, which were not analyzed or removed in their study. Assuming a 50 km thick magnetic layer they estimated a magnetization range between –12 and +17 A/m. More recently *Langlais et al.* [2003] used basically the same technique to model the three components of both the low and high altitude data. They produced a magnetic field map of all 3 components at 200 km altitude and a magnetization map at the surface of the planet. Downward continuation of the model field to the surface predict field intensities up to 6000 nT. Assuming a 40 km magnetic layer the magnetization components values found range from –12 to + 12 A/m. However they did not remove external contributions from the data and did not provide any estimation of that contamination. *Parker* [2003] specifically calculated the minimum magnetization intensity that would be required for a 50 km thick magnetic layer to best fit the data. He found that the magnetization intensity should be at least 4.76 A/m. Most of the magnetization values obtained in this study are consistent with the results stated above.

It is important to understand the pros and cons of both spherical harmonics modeling and inverse source modeling. Many magnetic anomalies modeling were based on spherical harmonics models rather than directly using observed data [*Arkani-Hamed*, 2001 ; *Phillips*, 2003]. Spherical harmonics modeling of a potential field works well when one hopes to get a global picture of the field. It requires a global, homogeneous data coverage, which is certainly what we have for the high altitude data. However low altitude data coverage is far from homogenous and would introduce errors in the model. As stated earlier spherical harmonics models are sensitive to noise in the higher harmonics. That noise is amplified when downward continuation is performed therefore limiting the value of low altitude or surface estimations of the magnetic field. One more important drawback of spherical harmonics models is that it does not say anything about the physical characteristics of the source. For example the surface magnetization, a very important parameter to constrain the composition and the size of the source body, can not be evaluated without making other assumptions. Since this thesis is concerned with finding the paleopole positions of Mars, magnetization of the source is needed, so spherical harmonics modeling will not be used.

The equivalent dipole technique is less sensitive to geographical data distribution and does not require global coverage. A very good point if low altitude data is to be used. It also provide information on the magnetization of the source but does not constrain in any way the size and shape of the source body. *Langlais et al.* [2003] have produced a magnetization map of the surface of Mars based on their equivalent dipole source modeling. Their map shows a magnetization range of –9/+11.5, -7.8/+11.3 and –6.2/+6.7 A/m for the r, theta and phi component respectively. These values are not, of course, absolute because of the non unique character of the model. If they are representative of what is actually going on at the surface then one can see that the horizontal magnetization component are as important as the radial component and should be considered to get an accurate portrait of the magnetic field. The inverse source technique work also better than the spherical harmonics modeling technique if one is interested in studying the magnetic field locally. In this thesis I model the local fields over selected isolated anomalies so the equivalent source technique is more appropriate.

However I go one step further by replacing the dipole with an elliptical prism of uniform magnetization. The magnetic field created by an elliptical prism has fundamental differences with the one created by a circular prism or a dipole. An example of the magnetic field produced by the three source bodies currently used in equivalent source modeling is presented in figure 2.1. Most anomalies presented in figure 2.6 have an elliptical shape and elliptical prisms are thus more appropriate to model them. This method, initially used by *Arkani-Hamed* [2001], provides information on the location of the source and gives first order approximation of the size and shape of the magnetic source. The extra degrees of freedom provided by an elliptical prism will make the model fit the data better. To be accurate, one of the most fundamental requirement that the method need to meet is the use of magnetic anomalies that are sufficiently isolated from neighboring sources. In practice, however, the ideal fully isolated magnetic anomaly does not exist and some contamination from nearby sources is always present.

Langlais et al. [2003] have estimated that contribution to a given measurement by nearby sources that are more than 1500 km away is negligible. Numerical experiments made for this thesis

support this conclusion. Applying this criteria to Mars, however, is difficult at best. To be isolated this would mean that an anomaly should be alone in a circle of 25° radius. Contribution from neighboring sources will, of course, affect the observed field depending on the location, geometry and magnetization of the sources. All these parameters show considerable non uniqueness. This mean that the three components of the magnetic field of the anomaly under study could be affected differently. If one models the three components of the observed field of a contaminated anomaly separately he would get a different magnetization model for each and therefore a different pole position. So modeling each component of the data separately gives a very good indication of how isolated a given anomaly is and how free of external noise the data really is. Clustering of the poles obtained by modeling separately the three components would indicate that the anomaly is sufficiently well isolated to have confidence in the pole position obtained from the model. If an anomaly is perfectly isolated and the data perfectly clean the space domain algorithm used in this study would give the same pole positions for all three components. I will demonstrate in chapter 4 the effectiveness of the algorithm on synthetic data before using it with actual data. The same space domain algorithm is used in both modeling effort described in chapter 3 and 4.

Using source bodies other than dipoles have been considered in the past. *Arkani-Hamed* [2001] used elliptical prisms to model ten relatively isolated small magnetic anomalies and found that most of them were clustering within a 30° circle centered at 25N, 230E and that both north and south magnetic poles are found in the cluster suggesting pole reversals on Mars. The anomalies were extracted from a spherical harmonics model of the magnetic field [*Arkani-Hamed*, 2000] that was generated using low altitude data alone. Although steps were taken to minimize external contributions to the observed field for each anomaly, this study did not address the issue of data quality. *Hood and Zacharian* [2001] used low altitude data along MGS tracks to model two anomalies in the northern hemisphere with both dipoles and circular prisms. The dipole models yielded sources at depth of about 150 km, which they argued, is unlikely because temperature at such a depth is probably over the Curie point. So the dipole models were discarded. They found paleomagnetic poles in the region north east of Tharsis which is in general agreement with *Arkani-Hamed* [2001]. However using circular prisms alone will not give the optimal fit between

data and model. *Hood and Zacharian* [2001] and *Hood and Richmond* [2002] did not move the prism to optimize the placement of the prism with respect to the center of the anomaly. An horizontally magnetized prism will show it's maximum Z or radial component away from the center of the source body. Therefore any model that do not take that into account will not give the best possible fit between model and data.

Also in *Hood and Zacharian* [2001] as well as in *Hood and Richmond* [2002], certain anomalies were modeled with two circular prisms, which yielded a better fit between observed field and model. Adding sources will easily improved the fit between data and model for a given anomaly. However interpretation of the results, especially as far as calculating the poles of the ancient core field is concerned is difficult. To obtain a reliable pole position one needs a uniformly magnetized source. I have elected, in this study, to model each anomaly with only one elliptical prism source. This source is assumed to be uniformly magnetized and the top of the prism is placed at the surface of the planet. Once a model is obtained, its quality is evaluated and the model is rejected if the fit between data and model is poor.

Arkani-Hamed and Boutin [2004] (see chapter 3 and figure 2.6 in this chapter) used both the low and high altitude data to model 9 relatively isolated anomalies. They smoothed the low altitude tracks by fitting and removing a quadratic polynomial consistent with methods used in other studies. They smoothed high altitude data in the Fourier domain to remove time dependant field contributions. Paleopole positions found are in general agreement with other studies although clustering is not as tight as mentioned by *Arkani-Hamed* [2001]. *Langlais et al.* [2003] also challenged the clustering of the poles based on their equivalent source modeling results. They also found different paleopole positions for most of the anomalies studied by *Arkani-Hamed* [2001]. This difference in results based on two very different modeling technique shows the danger of working with models instead of actual data. Clustering of the poles, if established firmly, could have a great influence on our understanding of the tectonic of Mars. The *Arkani-Hamed and Boutin* [2004] study has shown the much greater importance of low altitude data over high altitude when both are considered simultaneously in a model. The two data sets modeled separately would not give the same pole position. This is an indication that the anomalies are not

fully isolated. None of the previous studies have modeled the three components of a given anomaly separately to check if the pole positions coincide, a key feature of the study in chapter 4.

More recently *Philips* [2004] used the Helbig integral equations theory to estimate crustal magnetization, paleomagnetic pole positions and whether or not the ancient global field had reversed during its history. *Helbig* [1963] has calculated 9 first order moment integrals of the magnetic field components. In theory 5 of them should vanish and the other 4 provide the 3 components of the magnetization. All these integrals are theoretically evaluated from $-\infty$ to $+\infty$ so that in practice one can not fully evaluate the integrals. Phillips numerically evaluated the integrals on finite size windows and removed a planar surface from the data to make the theoretically vanishing integrals as close to 0 as possible. However Phillips did not use the available data directly but calculated the magnetic field at 150 km altitude using *Cain* [2003] spherical harmonic model described earlier. The results he obtained support reversal of core dynamo but clustering of the pole seems to be supported only for sources with a minimum magnetization intensity of 4A/m. Moreover, distribution of equivalent dipole sources shows a strong concentration in places where the measured magnetic field is low like in the northern plains. Sources seem also to concentrate along some lines of longitude. Although technically not impossible the presence of so many sources in the northern hemisphere is highly unlikely. This seems to be indicative, as pointed out by Philips himself, of an important presence of external noise in the data used for the evaluation of the Helbig integrals. One could go one step further and argue that the noise was probably amplified by the downward continuation of the high harmonics of the spherical harmonics model used in the study. Cain's model does not represent low altitude data very well so the altitude chosen here for the downward continuation of the model might be too low and may not be truly representative of the capacity of the model.

Figure 2.1

A simple comparison between the X,Y and Z component of the magnetic field produced by an elliptical prism (top row), a circular prism (middle row) and a dipole (bottom row). The field was calculated at 400 km altitude. Each source has the same magnetic dipole moment. The same color scale is used for all Z components and for all X and Y components. The general behavior of all fields is about the same but subtle and important differences exists. The Z component of the elliptical prism shows a different shape than the one produced by the circular prism while the X and Y components shows little difference. Also visible is the appearance of a small negative lobe in the Z component of the dipole field, which is not present in the other Z components.

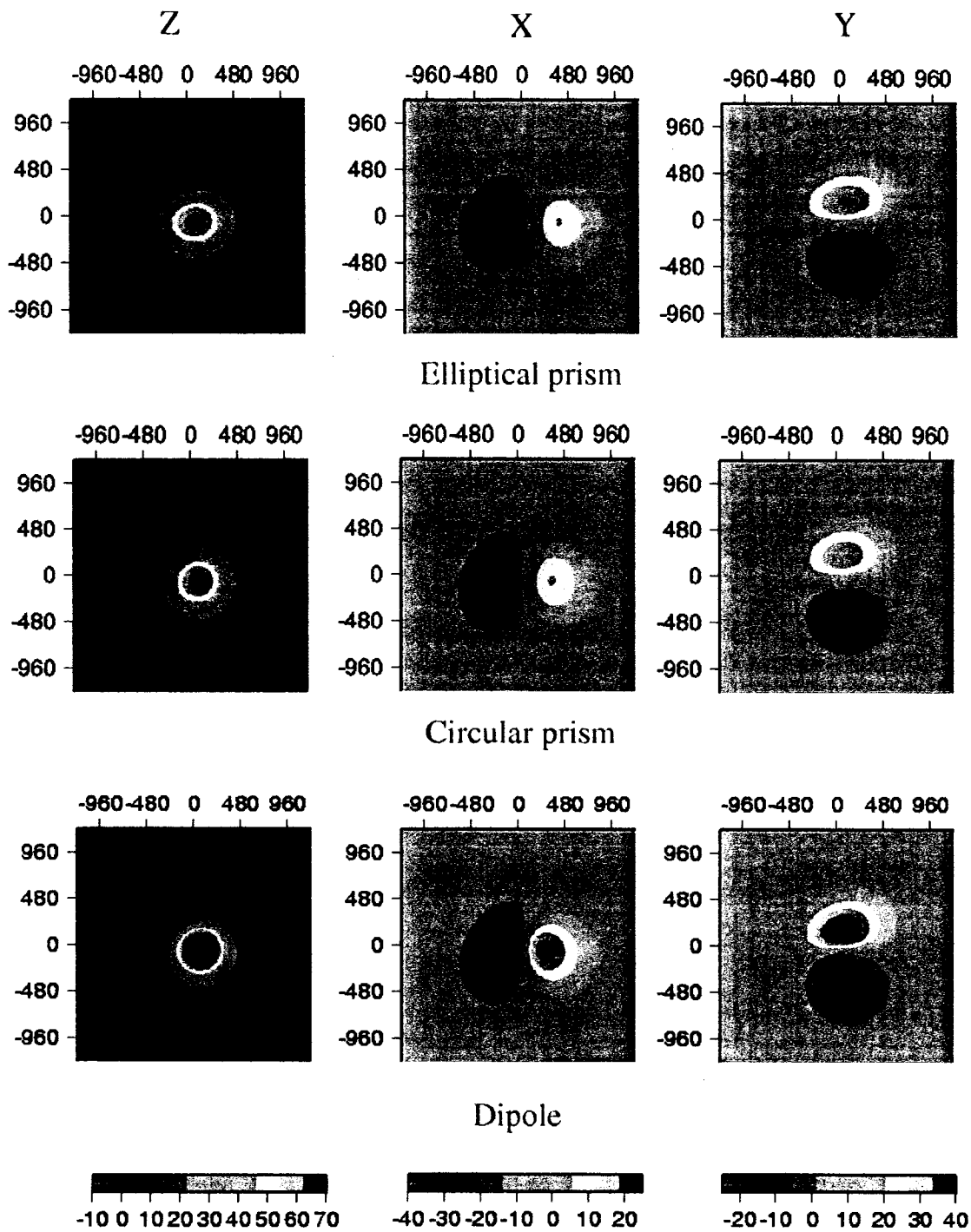
Z
X
Y
-960 -480 0 480 960
960
480
0
-480
-960
Elliptical prism
Circular prism
Dipole
-10 0 10 20 30 40 50 60 70
-40 -30 -20 -10 0 10 20
-20 -10 0 10 20 30 40

Figure 2.1

Figure 2.2

A global view of the Martian magnetic field at an average of 400 km altitude. The top panel is the radial component, the middle panel (noted phi) is the east-west component and the bottom panel (noted theta) is the north-south component. All mapping phase data available from March 1999 to April 2003 were used to build the maps. A total of 28,800,000 data points were binned in 0.5 by 0.5 deg grid. The scale of the maps is limited to values between –60 to +60 nT to better show the magnetic anomalies. The global characteristics of the field are visible in those maps. One can see for example the relative weakness of the field in the northern hemisphere compared to the southern hemisphere. The absence of anomalies in and around the big basins indicates that those were probably demagnetized by the impact.

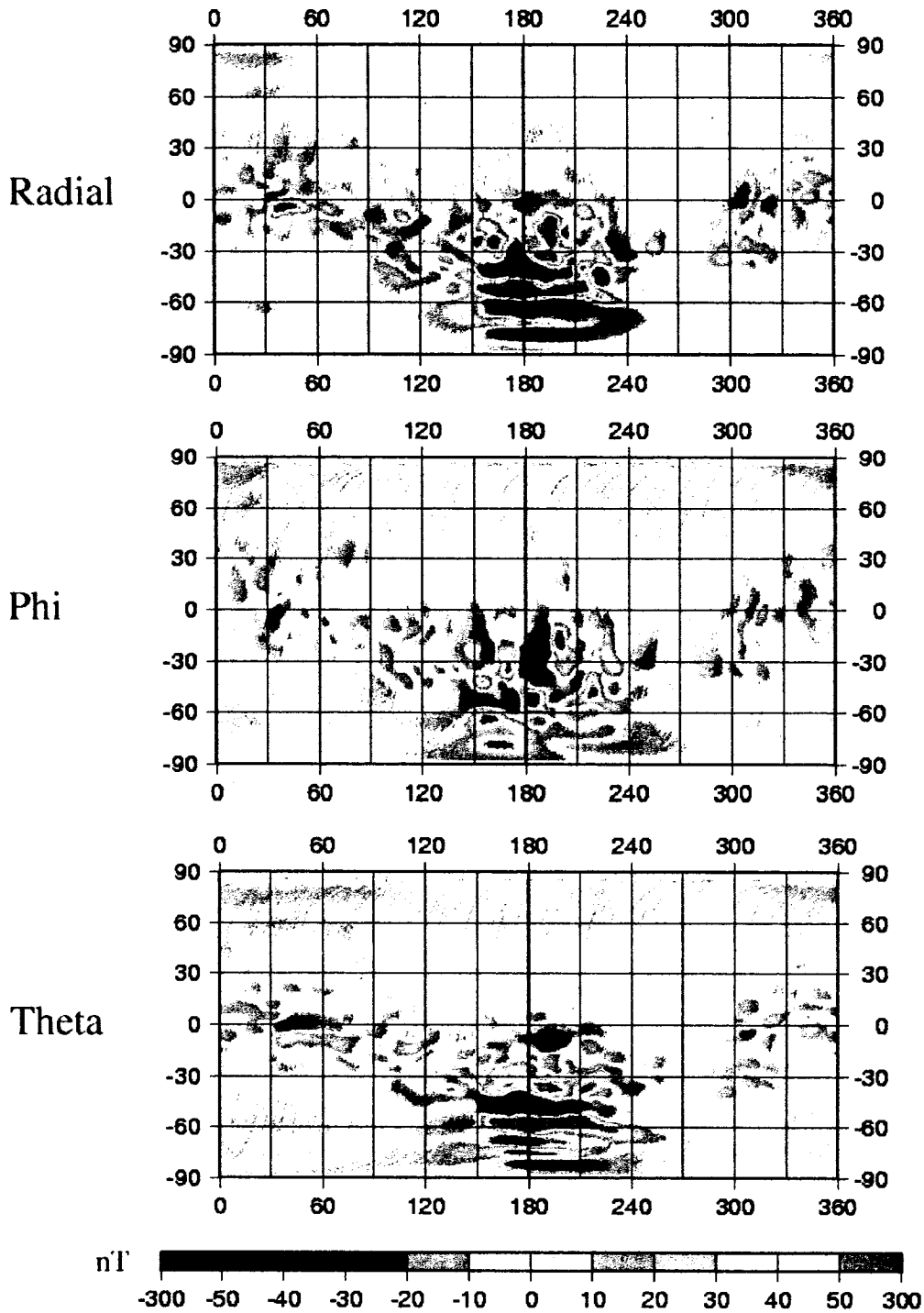
Radial
Phi
Theta
0 60 120 180 240 300 360
90 60 30 0 -30 -60 -90
nT
-300 -50 -40 -30 -20 -10 0 10 20 30 40 50 300

Figure 2.2

Figure 2.3

An example of high altitude data contamination. The two top panels are radial high altitude magnetic data measurements taken at two different times. The data was binned in the same manner as in figure 2.2. If there was no external contamination the two top panels should be perfectly identical. Although they look very similar, the bottom panel, which represent the difference between panel HA1 and panel HA2, shows that there are differences of up to 20 nT .

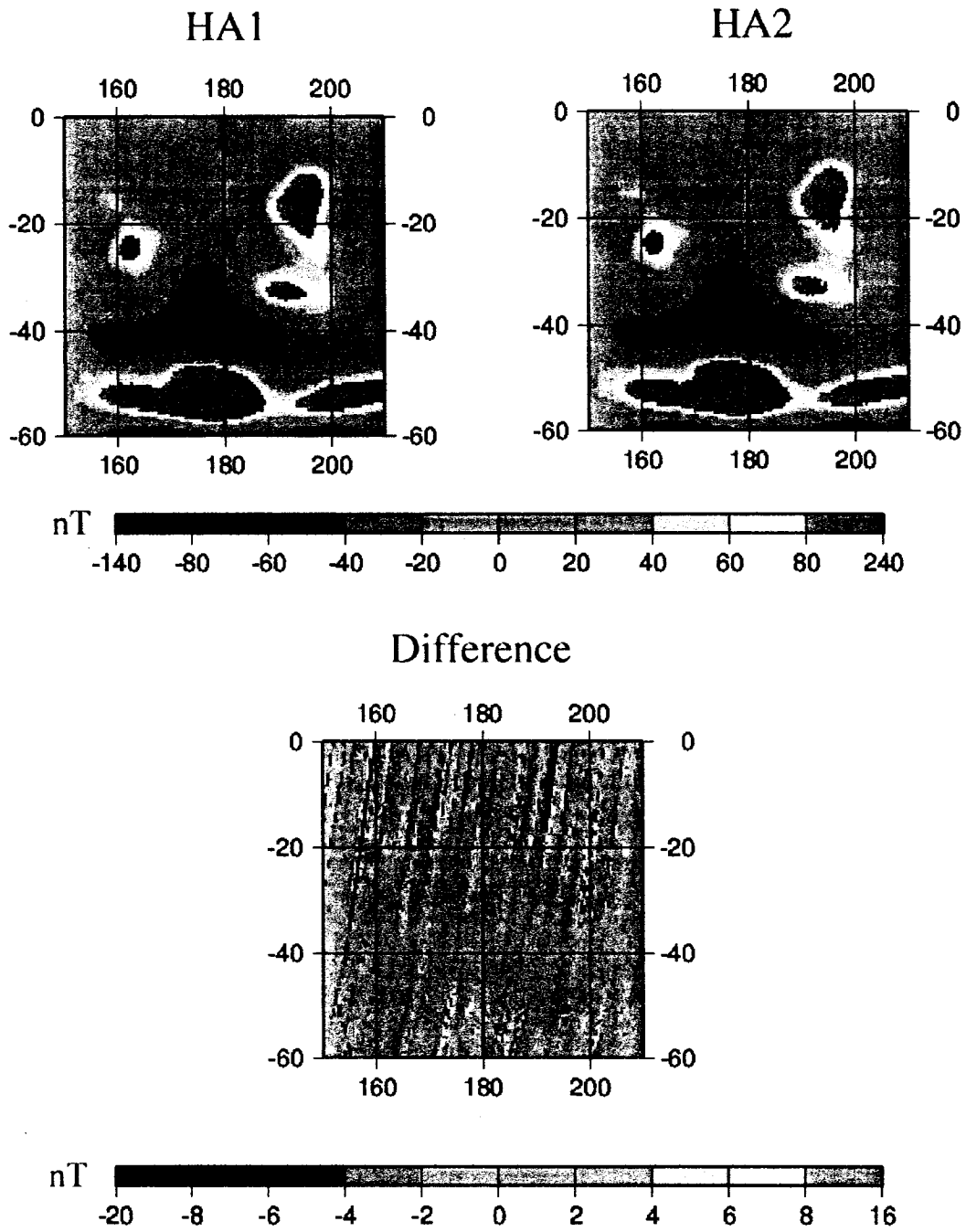
HA1
HA2
160
180
200
0
-20
-40
-60
nT
-140
-80
-60
-40
-20
0
20
40
60
80
240
Difference
-8
-6
-4
-2
2
4
6
8
16

Figure 2.3

Figure 2.4

Another illustration of external contamination. I extracted 8 tracks from the high altitude data within 0.5 deg of the position lat –5, long 66. The tracks were measured at different times during the mapping phase (MO) portion of the mission. Each graph represent the value of the corresponding component versus latitude. Each track is 20 deg long. Since the tracks are so close to each other and virtually at the same altitude they should yield practically identical results for each component. This is not the case. The difference between the two extreme tracks is superior to the margin of error and must be attributed to external contamination.

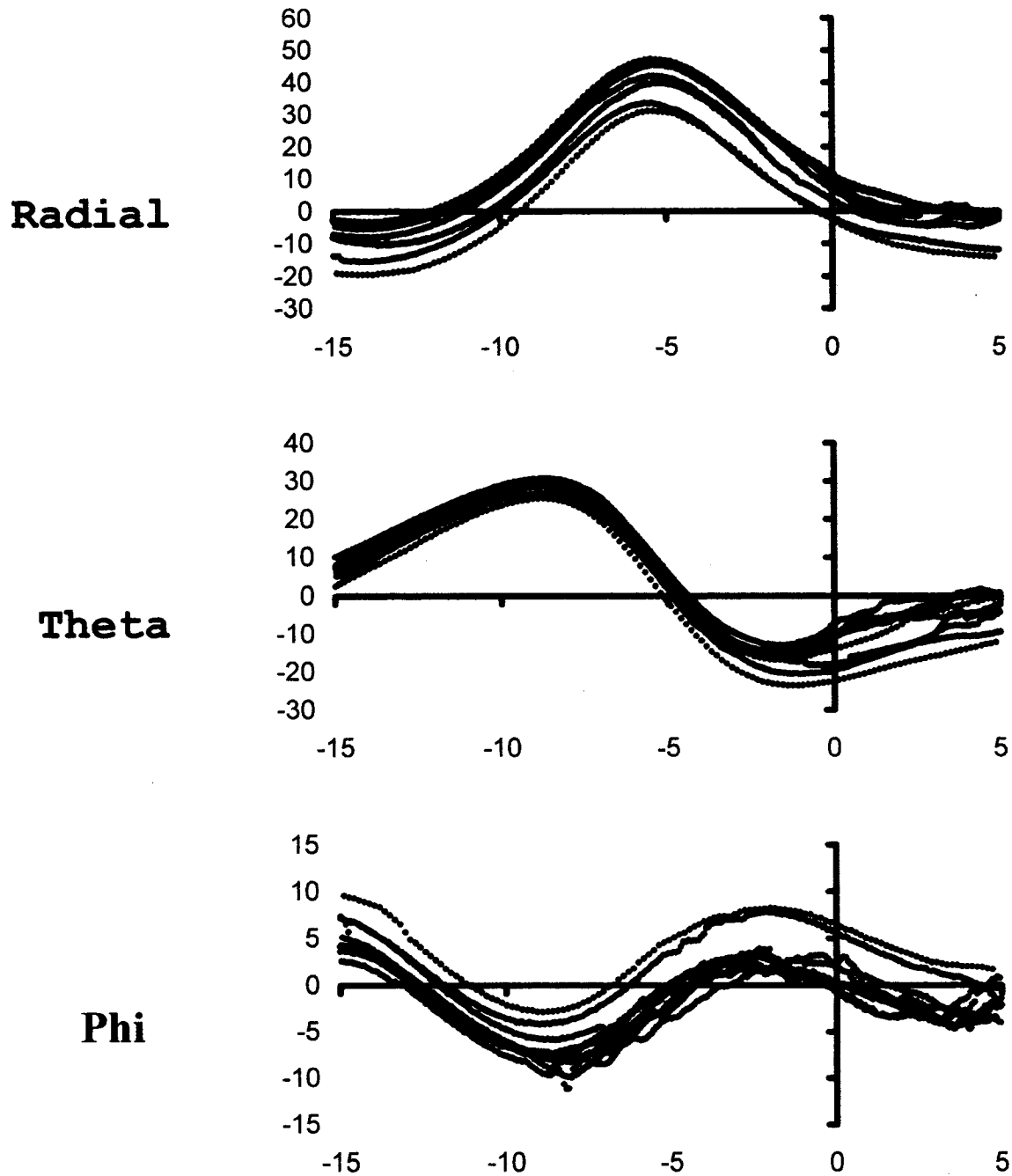
Radial
60
50
40
30
20
10
0
-10
-20
-30
-15
-10
-5
0
5
Theta
40
30
20
10
0
-10
-20
-30
-15
-10
-5
0
5
Phi
15
10
5
0
-5
-10
-15
-15
-10
-5
0
5

Figure 2.4

Figure 2.5

A numerical experiment in which 20 dipole sources of random dipole moment were placed at the surface of a planet of radius 3390 km, a Mars type planet. The total field resulting from the vector sum of the field of all individual sources was calculated at an altitude of 400 km. The three spherical coordinates components of the total field are presented. The white dots on each sphere represent the position of the sources bodies. Most sources are placed near longitude 180 and latitude 0 in order to mimic the actual situation on Mars. The goal of this simulation, however, was not to reproduced the observed field on Mars. In the case of the radial component one can clearly see that in many situations the maximum (or minimum) does not correlate with the actual position of the source. In the phi and theta maps some long wavelength influence is clearly visible and make for non zero field values at places very far away from any sources. The dipole field is calculated by using the method described in *Dyment and Arkani-Hamed* [1998].

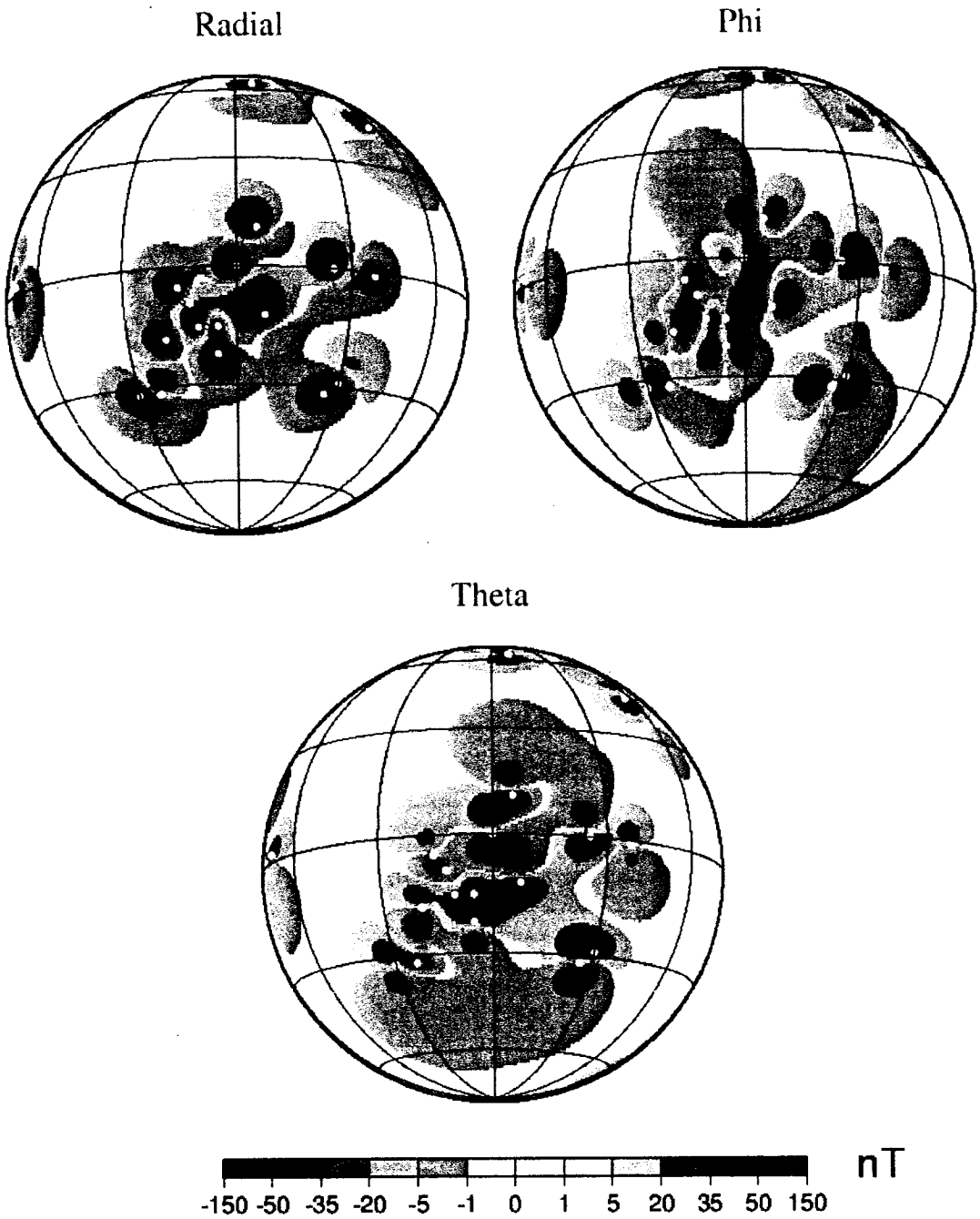

Figure 2.5

Figure 2.6

The radial component of the magnetic field of the nine magnetic anomalies used in the modeling of chapter 3 and 4. Each anomaly is represented by a 20^{o} by 20^{o} cut of the high altitude radial data map of figure 2.2. One can see the various shapes and sizes of the anomalies. It is quite apparent that these anomalies are not fully isolated. Around almost all of them there are nearby anomalies that are interacting to sensibly modify the resultant magnetic field of the anomaly of interest. For a well isolated anomaly this influence will be minimal. Most of the anomalies show an elliptical shape. Although anomaly A1 and A2 were treated as being produced by two different sources, one can not exclude the possibility that they come from a single source since the shape and size of both anomalies are similar.

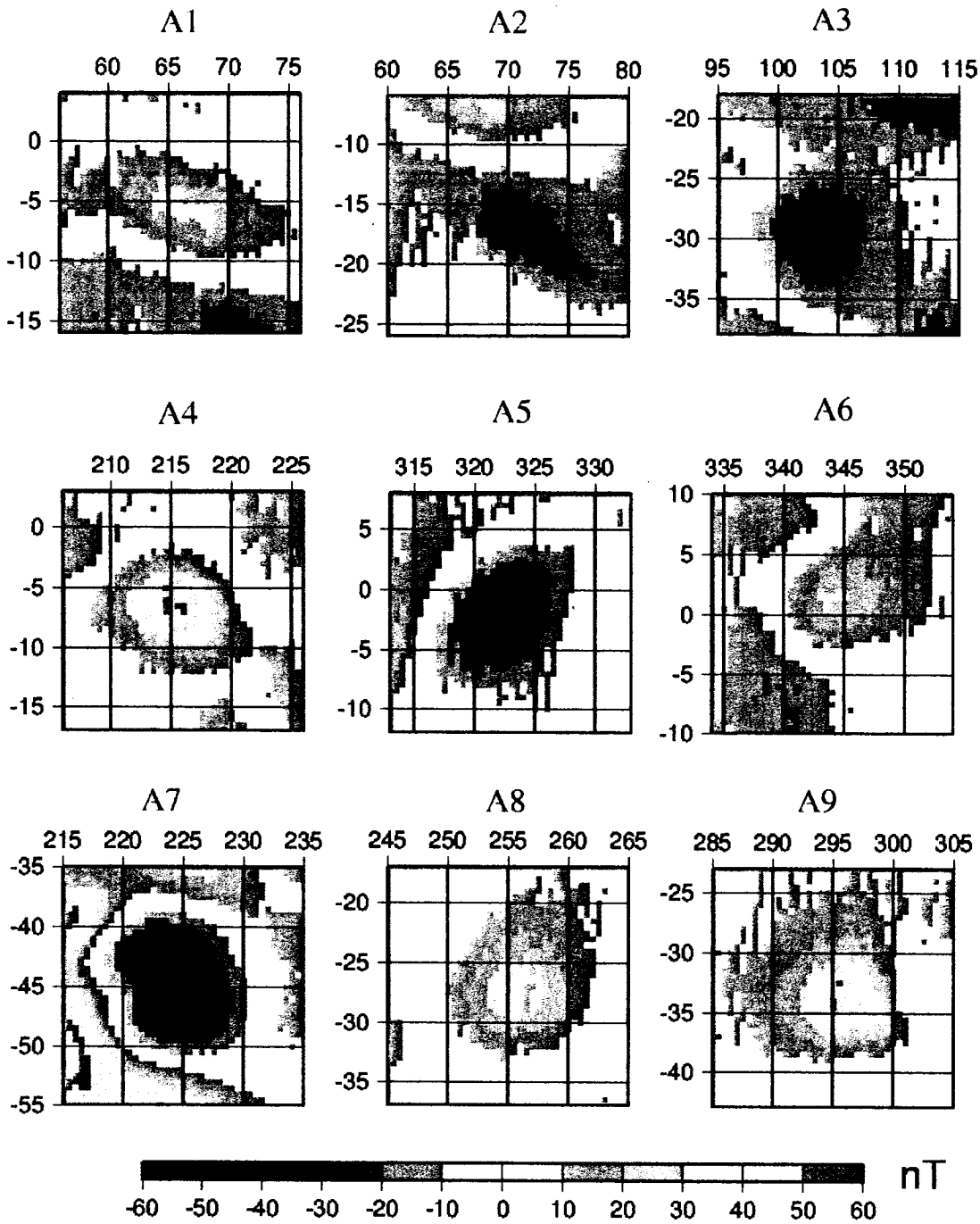
A1
60 65 70 75
0 -5 -10 -15
A2
60 65 70 75 80
-10 -15 -20 -25
A3
95 100 105 110 115
-20 -25 -30 -35
A4
210 215 220 225
0 -5 -10 -15
A5
315 320 325 330
5 0 -5 -10
A6
335 340 345 350
10 5 0 -5 -10
A7
215 220 225 230 235
-35 -40 -45 -50 -55
A8
245 250 255 260 265
-20 -25 -30 -35
A9
285 290 295 300 305
-25 -30 -35 -40
-60 -50 -40 -30 -20 -10 0 10 20 30 40 50 60
nT

Figure 2.6

Chapter 3: Paleomagnetic poles of Mars revisited

Jafar Arkani-Hamed and Daniel Boutin
Earth and Planetary Sciences, McGill University, Montreal, Canada
Published in Journal of Geophysical Research, Vol 109, 2004

3.1 Abstract

The huge amount of data acquired by Mars Global Surveyor during its mapping period provides a unique opportunity to re-assess the paleomagnetic pole positions of Mars previously determined on the basis of the limited low-altitude magnetic data. We identify 9 small and isolated magnetic anomalies on the basis of the global magnetic maps, and model each anomaly using a vertical prism of elliptical cross section. Both high-altitude (360-430 km) and low-altitude (100-200 km) magnetic data are used simultaneously. We calculate a paleomagnetic pole position assuming that the body is magnetized by a dipole core field. Although the new pole positions do not cluster as closely as the old ones, the new overlaps the older cluster. The clustering suggests that Mars' rotation axis has likely wandered by about 50-60 degrees in the last about 4 Gyr. The number of north and south poles in the cluster suggests at least one reversal of the core field during the time the source bodies acquired magnetization.

3.2 Introduction

Attempts have been made to estimate the core field direction that magnetized the Martian crust some ~4 Gyr ago. *Arkani-Hamed* [2001a] modeled the magnetic source bodies of 10 small and isolated magnetic anomalies using vertical prisms of elliptical cross sections and employing a Fourier domain algorithm. He then determined the corresponding paleomagnetic pole positions, assuming that the source bodies were magnetized by a

dipole core field, which is a standard practice in paleomagnetic investigations [e.g., *Butler*, 1992]. Seven out of the 10 poles clustered within a radius of 30 degrees centered at around 25N, 225E. The remaining three were also clustered to the west of the first cluster. *Hood and Zakharian* [2001] used along-track data to model the source bodies of two magnetic anomalies near the north pole using vertical prisms of circular cross sections and adopting a space domain algorithm. One of the anomalies was included in the 10 anomalies modeled by Arkani-Hamed, and the calculated pole positions by the authors are less than 5^{o} apart. The paleomagnetic pole positions were preliminary as emphasized by Arkani-Hamed, because of limited data available at the time. The 10 anomalies were extracted from a 50-degree spherical harmonic model of the magnetic field of Mars that had been derived on the basis of the low-altitude (100-200 km) Mars Global Surveyor data [*Arkani-Hamed*, 2001b]. The original data had many wide gaps parallel to the satellite tracks, and the number of original tracks passing over an individual anomaly was limited. The anomalies were partly defined through interpolation based on the spherical harmonic model. The track data used by Hood and Zakharian were also extracted from the low-altitude data and suffered from similar limited coverage and from the across-track interpolation process. If these paleopole positions are confirmed by the presently available vast amount of the high-altitude (360-430 km) magnetic data, they will have important implications not only about the magnetization of the source bodies, but also about the dynamics of Mars. For example, the clustering of the poles will indicate no pervasive plate tectonics on Mars since the source bodies were magnetized. The locations of the pole positions will suggest an appreciable polar wander of Mars if the dipole core field axis coincided with the rotation axis of the planet at ~4 Gyr ago, which is almost the case for Earth and Mercury at the present. The vast amount of high-altitude magnetic data also provides a good opportunity to identify and model other isolated anomalies. *Hood and Richmond* [2002] used earlier parts of the high-altitude data to model two new anomalies in the low latitudes. The paleomagnetic pole position determined from one of the anomalies falls within the 30-degree radius circle of Arkani-Hamed.

We present the paleomagnetic pole positions of Mars determined through modeling 9 small and isolated magnetic anomalies that include some of the previous 10 anomalies. We use vertical prisms of elliptical cross sections to model both the low- and high-altitude data simultaneously, by adopting a new space domain algorithm.

3.3 Paleomagnetic poles of Mars

The paleomagnetic pole position of Earth is usually determined using in situ measurements of the direction of rock magnetization [e.g., *Butler*, 1992 ; *Dunlop and Ozdemir*, 1997]. Such measurements are not available on Mars at present. However, a rough estimate of the paleomagnetic pole position of Mars can be made on the basis of modeling magnetic anomalies. A desirable anomaly must be a) isolated enough to ensure no substantial contribution from nearby magnetic source bodies, b) large enough to be resolved by magnetic measurements at high altitudes of ~400 km, and c) small and simple enough to ensure that it can be modeled by a simple-shaped body of uniform magnetization. It is difficult to fulfill all of these criteria. For example, a simple looking magnetic anomaly at high elevations can arise from coalescing of the magnetic fields of many irregular but closely located bodies. The anomaly simply arises from the combined magnetic fields of the bodies. However, the magnetizing core field direction may not change appreciably over a small area, unless it reverses or undergoes significant polar wander, and the small bodies are likely magnetized in a single direction. The magnetization direction of a single source model still is a good approximation of the core field direction. To fulfill these stringent criteria we must deal very carefully with the short wavelength components of the data that are close to the resolution limit and are likely more susceptible to data noise and data processing errors. Therefore stringent constraints on the data processing and modeling must be implemented (see the Appendix).

With the above caveats in mind, we model 9 isolated magnetic anomalies. A model source body is a vertical prism of elliptical cross section with uniform magnetization. The top of the prism coincides with the local surface of an elliptical Mars that has a polar radius of 3380 km and an equatorial radius of 3400 km. For a given magnetic anomaly, the three components of the magnetic data are extracted from both low- and high-altitude data sets and transferred to a local rectangular coordinate system centered on the anomaly with the origin at the surface of the elliptical Mars. Details of data processing and modeling are presented in the Appendix. The dimensions and vector magnetization components of the model source bodies are listed in Table 1.

Figure 3.1a shows the global map of the radial magnetic anomalies of Mars at 390 km elevation derived from the high-altitude data. The locations of the magnetic anomalies are superimposed on the figure. A paleomagnetic pole is determined from the magnetization of a source body, assuming that the body is magnetized by a dipole core field, which is a standard procedure in paleomagnetic studies [e.g., *Butler*, 1992]. The core field is upward in the north and downward in the south, it is in the opposite direction to Earth's geomagnetic dipole. The paleomagnetic pole positions thus determined (Figure 3.1b) show clustering of the poles, though not as tightly as those of *Arkani-Hamed* [2001a]. Included in Table 1 are the paleomagnetic pole positions shown in Figure 3.1b as well as those obtained by *Arkani-Hamed* [2001a] and *Richmond and Hood* [2003]. Figure 3.1b shows two clusters, three of the poles are clustered near 180 degree longitude and the rest around 270 longitude. Double clustering also existed in the pole positions of Arkani-Hamed. A densely distributed low-altitude magnetic data is required to better delineate the details of the small magnetic anomalies and determine whether the double clustering reflects appreciable polar wander of Mars within the period the magnetic bodies acquired magnetization, or arises from the uncertainty of the present pole positions. There is a general agreement between the results of different authors (see also *Phillips* [2003]) but they are not identical because of many factors discussed below.

3.4 Discussion

This section discusses some issues concerning the viability of the results and briefly addresses their main implications.

Determination of a magnetic source body on the basis of its magnetic anomaly is doubly non-unique. Not only the shape and the magnetization intensity of the source body, but also the direction of the magnetization must be obtained. To reduce the extent of the non-uniqueness, it is desirable to determine the shape of the body before calculating its magnetization. The analytic signal technique has been used to delineate sharp magnetic boundaries [e.g., *Nabighian*, 1972] and thus can be utilized to determine the shape of a magnetic body that is uniformly magnetized [*Roest et al.*, 1992]. We examined the applicability of this technique to the small and isolated magnetic anomalies of Mars by calculating the magnetic anomaly of a vertical prism at altitudes ranging from 50 to 400 km. The prism was 10 km thick and had a square cross section of 400X400 km. It was magnetized either vertically or horizontally parallel to a side of the square. The simple shape of the prism and its uniform magnetization result in the strongest analytic signal compared to those of irregular-shaped magnetic bodies with varying magnetization encountered in practice. In both models the maxima of the analytic signal at 50 km elevation delineated the sides of the square, but the maxima migrated inward as the elevation increased. The maxima coalesced at around 150 km elevation and formed a flat region that covered about 50% of the entire surface of the prism. At even higher altitudes they formed a single maximum over the center of the prism, which was broad and could not be effectively used in practice to determine the center of the prism. This is because in practice the data noise is enhanced due to the application of the gradient operator in the analytic signal calculations, and the location of the maximum can be controlled by local noise. Therefore, we made no attempts to use the analytic signal technique to define either the shape or the center of the source bodies.

Hood and Zakharian [2001] and Hood and *Richmond* [2002] used circular prisms to model some isolated magnetic anomalies. *Arkani-Hamed* [2001a] adopted elliptical models in his work, which is also utilized in the present study. We note that the circular prism is one of our trial models, when the semi-minor axis of the ellipse equals to its semi-major axis. However, none of the final models is circular. The freedom of varying the length of the semi-minor axis and the orientation of the ellipse, none of which are required for a circular prism, allows the magnetic field of an elliptical body fit the observation better than that of a circular body. It is desirable to determine as to what extent a paleomagnetic pole position determined by an elliptical model differs from that determined by a circular model. We address this question theoretically by calculating the magnetic field of an elliptical prism and then modeling the field using a circular prism. The magnetic field is calculated at 150 km and 400 km altitudes that are the mean elevations of the low- and high-altitude Mars Global Surveyor data, respectively. The total dipole moment (magnetization integrated over the entire volume of the body) of the circular prism is close to that of the elliptical prism in all models we calculated. If the elliptical body is vertically magnetized, the pole position determined by the circular prism model coincides with that of the elliptical prism. Figure 3.2 shows the magnetization of the original elliptical prism and that of the circular model when the original prism is horizontally magnetized (x and y axes of the figure are the semi-major and semi-minor axes of the elliptical prism). If the elliptical prism is magnetized along one of its symmetric axes, the pole position determined by the circular model coincides with that of the elliptical prism. However, when the elliptical body is horizontally magnetized at some angle with respect to either of its symmetric axes, the two magnetization directions differ, by as much as ~15 degrees, which can result up to ~900 km error in the paleomagnetic pole position on Mars. The difference is large enough to favor the elliptical prism modeling technique. Figure 3.2 shows that the difference is more pronounced at 150 km altitude than at 400 km. This is because the short wavelength components of the magnetic field strongly attenuate with elevation, making the magnetic field of an elliptical body closer to that of a circular model at higher altitude.

The resolution of the original data has an important effect on the magnetic fields of the isolated bodies considered in this study. This is largely because of the stringent constraints imposed by the small size of the source bodies. The sparse low-altitude data have only a few orbit tracks over each of the anomalies. Arkani-Hamed extracted the anomalies from a 50-degree spherical harmonic model of the magnetic potential of Mars [*Arkani-Hamed*, 2001b]. Although the 50-degree model is a viable interpolation function that satisfies the potential field criteria, it may not represent the local anomalies accurately over areas with no original data. The across-track interpolation of a few track data using other interpolation functions [*Hood and Zakharian*, 2001] would not have resulted in a higher accuracy either. The high-altitude data densely cover the entire globe (except for small polar caps), but their resolution suffers from the high altitudes. The crustal magnetic anomalies with wavelengths shorter than ~400 km are not accurately reflected in the data [*Connerney et al.*, 2001; *Arkani-Hamed*, 2002]. Moreover, because of proximity to the ionosphere [*Mitchell et al.*, 2001], and strong attenuation with altitude of the short wavelength components of the crustal magnetic field, the signal to noise ratio of the high-altitude data is low over these components. For example, some of the anomalies modeled by *Arkani-Hamed* [2001a] on the basis of low-altitude data are not well-defined at high altitudes. They are not considered in this paper. Although the spread of the pole positions may arise from the polar wander of Mars during the magnetization of the source bodies, it is likely that the data noise and relatively low resolution of the high-altitude data have appreciable effects. Consequently, despite determined efforts made by several investigators, the paleomagnetic pole positions determined by modeling the isolated magnetic anomalies should be regarded as preliminary. At present, the accuracy of a given paleomagnetic pole position must be decided upon agreement of the results obtained by different authors using different methods. Low-elevation and uniformly distributed data with short across-track distances are required to determine the pole positions more accurately in the future.

For accurate modeling of a small isolated magnetic anomaly in a local rectangular coordinate system, it is required to take into account the shape of the Martian surface. *McGovern et al.* [2002] showed that ignoring the dynamic ellipticity of Mars when calculating the gravity field of surface features, such as Olympus Mons, introduces appreciable errors. This is because of the significant dynamic ellipticity of Mars and the strong decay of the short wavelength components of the gravity field with increasing altitude. The error introduced by ignoring the dynamic ellipticity is expected to be even larger for the magnetic fields of the isolated bodies considered in this paper. Not only are the bodies smaller than Olympus and thus are characterized by much shorter wavelengths, but also the magnetic field decays with altitude faster than the gravity field. To assess the error made by ignoring the dynamic ellipticity of Mars in calculating the magnetic field of a small body, we consider two vertically magnetized vertical prisms of 400X400 km and 200X200 km cross sections and 10 km thickness. They are comparable to the upper and lower limits of the source bodies listed in Table 1. The vertical component of the magnetic field over the center of each prism is determined at 390 km and 400 km elevations, resembling the high-altitude data elevations. The 10 km elevation difference represents the difference between the equatorial radius of the elliptical Mars and the mean radius of Mars. The magnetic fields determined at both altitudes differ by ~7% for both prisms. We repeat the same calculations but at 140 and 150 km elevations, resembling the mean elevation of the low-altitude data. The magnetic fields determined at both elevations differ by ~8% for the large prism, but as much as 14% for the small prism. The error is more pronounced at lower altitude and for smaller bodies. As mentioned before, we use the elliptical Mars to minimize the error.

An important observation that there are north poles as well as south poles in the cluster confirms the earlier observation by *Arkani-Hamed* [2001a], that the core field of Mars had reversals within the time span that the bodies were magnetized. The Earth's core field in the last ~160 Myr has an almost random pole reversal pattern, ranging from a constant polarity interval of ~30 Myr during the Cretaceous quiet period to the most

frequent polarity reversals of less than 1 Myr in the recent past. The lack of direct correlation between the surface morphology and the magnetic source bodies of Mars makes it difficult to assess the chronology of the acquisition of magnetization of the source bodies, and thus the reversal pattern of the core field of Mars. Our results suggest at least one reversal. If the core field reversals occurred during the cooling of a magnetic source body, different parts of the body would have been magnetized in opposite directions, and thus create opposite magnetic fields that tend to cancel each other (see *Shive* [1989] and *Arkani-Hamed and Celetti* [1989] for details). The actual magnetization intensity of different parts of the body would then be stronger than the averaged magnetization determined from its magnetic anomaly. Moreover, the calculated magnetization direction would be the resultant of the magnetization directions of different parts.

The appreciable differences of the pole positions from that of the present rotation axis indicate a substantial polar wander of Mars, if the paleomagnetic pole position coincided with the rotation axis of Mars at ~4 Gyr ago, which is almost the case for Earth and Mercury at the present. Polar wander could have been induced largely by the formation of the Tharsis bulge [*Melosh*, 1980; *Spada et al.*, 1996], and to lesser extent by the large shield volcanoes, such as Olympus and Tharsis montes, and giant impact basins, such as Hellas, Utopia, Argyre and Isidis. Detailed modeling of the polar wander is outside the scope of this short paper that is focused on the paleomagnetic pole positions of Mars.

3.5 Conclusions

Using both high-altitude and low-altitude Mars Global Surveyor magnetic data we modeled 9 isolated small magnetic anomalies. We used vertical prisms of elliptical cross sections and calculated the model source bodies of the anomalies through a space-domain forward modeling procedure. The directions of the magnetization vectors of the bodies were used to estimate the paleomagnetic pole positions, assuming that a given body is

magnetized in a dipole core field. The paleomagnetic pole positions estimated from these 9 anomalies show general agreement with those modeled by other investigators [*Arkani-Hamed*, 2001a; *Hood and Zakharian*, 2001; *Hood and Richmond*, 2002; *Phillips*, 2003], but are not identical. The differences are mainly due to the low resolution of the high-altitude data and large gaps in the low-altitude data. Very low elevation magnetic data is required to better delineate the magnetic anomalies and determine the pole positions with a higher accuracy. The paleopoles tend to cluster, although not as tightly as those determined by *Arkani-Hamed* [2001a]. None of the poles coincide with the present rotation axis of Mars, implying a wander of the rotation axis since the source bodies acquired their magnetization. There are both north and south poles in the cluster, suggesting reversals of the Martian core field.

Acknowledgments: This research was supported by the Natural Sciences and Engineering Research Council (NSERC) of Canada. We would like to thank the reviewers Nicola Richmond and Jeff Phillips for their constructive comments.

3.6 Appendix

The densely distributed high-altitude magnetic data that cover the entire globe of Mars (except for a small regions over the poles) have been (and still are being) acquired at 360 to 430 km altitude range during the mapping phase of Mars Global Surveyor. The vast amount of these high-altitude data allows us divide the entire data set into two almost equal subsets, acquired during two different periods separated by about a year, and from these derive two separate sets of high-altitude magnetic maps. Each data set almost uniformly covers the entire surface (except for the small areas near the poles) with a mean track separation less than 15 km. In this study we use the nighttime data, acquired during March 1999 to August 2002, to minimize the effects of the external field. These data are then transferred from the original rectangular coordinate system, fixed to Mars with the origin at the center of the planet, to a spherical coordinate system, again fixed to the planet and with the same origin. It is easy to manipulate data in the spherical

coordinate, map the tracks on the planet, and compare the resulting global maps with surface features. This process results in 6 global maps, 2 radial components, 2 north-south components and 2 east-west components. We note that global maps are used only for initial detection of the location of each anomaly, and no calculations are made on the basis of the global maps.

3.6.1 Spherical coordinate

We decimate the high-altitude data by vertically binning over 0.25X0.25 degree grid cells. The data altitude within a grid cell changes by less than +- 5 km, which is about 80 times shorter than the mean altitude of the data. The binning introduces negligible errors into the magnetic field at about 400 km. The data within a gird cell were averaged after removing the outliers (see *Arkani-Hamed*, [2002] for details), and the corresponding mean altitude is taken to be the data altitude of the cell. For a given anomaly, we select data over a square of 128X128 grid points centered at the anomaly. Each map is tapered to zero near the boundaries using a Hanning function over 10 grid points. The resulting tapered map is Fourier transformed, and its power spectrum is determined. We also determine the degree correlation between two similar maps, for example between two radial component maps. We low-pass filter the two maps to retain all wavelengths with degree correlation coefficients greater than 0.8. The resulting filtered maps are then averaged to obtain the averaged high-altitude maps of the anomaly.

Despite the high density of the data coverage, the high-altitude data resolution suffers from the high elevation of the spacecraft [e.g. *Connerney et al.*, 2001; *Arkani-Hamed*, 2002]. We use the low-altitude science phase and aerobreaking phase data that were acquired at 100-200 km altitude range to improve the resolution of the final magnetic source models. The elevation of the low-altitude data over a given anomaly may change appreciably. We bin the low-altitude data within elevation intervals of 10 km, a grid cell

has a 0.25X0.25 degree horizontal cross section and a 10 km height. This resulted in a very sparse data distribution in the 3D space.

The two similar data sets, for example the radial components of the high- and low-altitude binned values, are combined to obtain a single data set. The data points in a 3D space over a region consist of the high-altitude points that are densely distributed within a short altitude range and the low-altitude points that are very sparsely distributed within the 100-200 km altitude range. This resulted in three data sets, the radial, north-south, and east-west components of the magnetic field. In the following we consider anomaly 5, a typical anomaly, to explain the data processing we have adopted in the local rectangular coordinate system.

3.6.2 Rectangular coordinate

The modeling of an individual anomaly in terms of a vertical prism is made in a local rectangular coordinate system. The combined data sets over a given anomaly are transferred to a local rectangular coordinate system with the (x,y) plane tangent to the local surface of the elliptical Mars and the z axis upward. A 2D boxcar circular filter, centered at the anomaly, is applied to each data set in order to minimize the effects of nearby magnetic features that do not relate to the anomaly under consideration. The filter removes the data outside a given radius, which is visually selected and varies from one anomaly to the next. We note that, unlike in the spherical coordinate system, the z coordinates of the data points change significantly in the local rectangular system. *Hood and Zakharian* [2001] and *Hood and Richmond* [2002] adopted a rectangular coordinate system algorithm in their model calculations. They assumed a circular disk for a magnetic body with the center at the mean radius of Mars, while the edges of the disk were located significantly above the surface. Rather than using the actual height of a data point from the horizontal plane of the rectangular coordinate system for the z coordinate, the authors used the distance between the data point and the mean spherical surface of the

planet directly beneath the point. Because of the curvature of the satellite orbits, the z coordinates of the data points in the rectangular coordinate system decrease rapidly as the horizontal distance from the center of the disk increases. However, the distances between the data points and the mean spherical surface change very slowly. Their model calculation was, therefore, made at a higher altitude than the actual data point, and resulted in a higher magnetization for the model. The error introduced due to this mixing may result in an overestimate of the magnetization intensity by up to 10%.

3.6.3 Modeling

A given magnetic anomaly is modeled by a vertical prism of an elliptical cross section. The top of the prism is tangent to the local surface of the elliptical Mars and the prism is 10 km thick. The magnetic anomaly of a uniformly magnetized prism depends on the vertical integration of its magnetization. Increasing the thickness of the prism results in the decrease of the intensity of its magnetization, and vice versa, without affecting the magnetization direction. Adopting an elliptical prism, rather than circular, provides an opportunity to change the aspect ratio (major/minor axes) as well as the orientation of the body and thus enhance the goodness of fit between the observed and calculated anomalies. We use forward modeling in space domain. The magnetization of a given prism is determined by least square fitting of the magnetic field of the body to the observed data (here by observed data we mean the binned data). Let B^i_x, B^i_y and B^i_z denote the x (east), y (north), and z (upward) components of the observed magnetic field at x^i, y^i, and z^i coordinates, and F^i_x, F^i_y and F^i_z be the corresponding components of the magnetic field of a model prism. The least squared misfit ε is defined by

$$\sum_i \left[\left(B^i_x - F^i_x\right)^2 + \left(B^i_y - F^i_y\right)^2 + \left(B^i_z - F^i_z\right)^2 \right] = \varepsilon$$

where summation is over all data points. The semi-major axis of the prism is increased from 100 km to a maximum of 500 km with 20 km intervals. For a given semi-major

axis, the semi-minor axis is increased from 1/2 the semi-major axis to the semi-major axis with the same intervals, and the angle of the major axis with respect to the x axis of the coordinate system, α, increased from 0 to 180 degrees at 10 degree intervals. The center of the prism is initially decided upon visual inspection of all three high-altitude magnetic components. To avoid the adverse effects of possible initial misplacement of the center, we move the center within a square grid of 160X160 km at 30 km intervals, or within an area large enough to ensure that the absolute minimum misfit occurs somewhere inside the area and not at the borders. In the 4-D model parameter space, consisting of the semi-major axis, the semi-minor axis, the prism orientation angle α, and the location of the center of prism, the parameter values resulting in the absolute minimum misfit define the final successful model.

Figure 3.3 shows the elevation of the data points within a circle of 360 km radius centered on anomaly 5. The data inside this area are used to calculate the source model of the anomaly. The MGS altitude gently increases toward the north, with a maximum altitude variation of about 14 km, which is about 28 times smaller than the mean altitude of the satellite. For a given semi-major axis we vary other parameters, semi-minor axis, the angle α and the location of the center of the prism. Figure 3.4 shows the misfit values, normalized to the absolute minimum misfit value, versus the semi-major axis of the source model of anomaly 5. From over 19,000 models examined we only show the descending minimum misfit values. For example for the semi-major axis of 100 km the first normalized minimum misfit value is 14.8, the second descending minimum is 14.4, the third is 14, and so on. The minimum misfit value decreases with the increase of the semi-major axis and reaches an absolute minimum, which defines the final successful source model of the anomaly. However, the descending-minimum value versus semi-major axis curve is broad, implying that the magnetization of the successful model is not tightly constraint. Figure 3.5 shows the three components of the observed high-altitude data, and those of the final model at 400 km, and figure 3.6 displays the observed low-altitude and model vector components along an orbit track that passes almost over the

center of the anomaly. The figures illustrate the goodness of fit of the model to the observation.

We determine the paleomagnetic pole position from the magnetization vector of a source body that is assumed to be magnetized by a dipole core field. Figure 3.7 shows the pole positions for all models of anomaly 5 with misfit values within 1.5 times the absolute misfit value. The slow convergence of the pole locations reflects the scale of uncertainty of the final pole position. The slow convergence is a direct consequence of the broad absolute minimum shown in Figure 3.4.

3.7 References

Arkani-Hamed, J., Paleomagnetic pole positions and pole reversals of Mars, Geophys. Res. Lett., 28, 3409-3412, 2001a.

Arkani-Hamed J., A 50 degree spherical harmonic model of the magnetic field of Mars {\it J. Geophys. Res.}, 106, 23,197-23,208, 2001b.

Arkani-Hamed, J., An improved 50-degree spherical harmonic model of the magnetic field of Mars, derived from both high-altitude and low-altitude observations, J. Geophys. Res., 107, E10, 5083, doi:10.1029/2001JE001835, 2002.

Arkani-Hamed, J., and G. Celetti, Effects of thermal remanent magnetization on the magnetic anomalies of intrusives, J. Geophys. Res., 94, 7364-7378, 1989.

Butler, R.F., Paleomagnetism, Blackwell Sci., Malden, Mass, 1992.

Connerney, J. E. P., M. H. Acuna, P. J. Wasilewski, G. Kletetschka, N.F. Ness, H. Remes, R. P. Lin, and D. L. Mitchell, The global magnetic field of Mars and implications for crustal evolution, Geophys. Res. Lett., 28, 4015-4018, 2001.

Dunlop, D.J., and O. Ozdemir, Rock magnetism: Fundamentals and Frontiers, Cambridge University Press, New York, 573 pp., 1997.

Hood, L.L., and N. Richmond, Mapping and modeling of major magnetic anomalies, LPSC XXXIII, Abstract 1128, LPI, Houston, 2002.

Hood, L.L., and A. Zakharian, Mapping and modeling of magnetic anomalies in the northern polar region of Mars, J. Geophys. Res., 106, 14601-14619, 2001.

McGovern P.J., S.C. Solomon, D.E. Smith, M.T. Zuber, M. Simons, M.A. Wieczorek; R.J. Phillips, G.A. Neumann, O. Aharonson, and J.W. Head, Localized gravity/topography admittance and correlation spectra on Mars: Implications for regional and global evolution, J. Geophys. Res., 107, E12, 5136, doi:10.1029/2002JE001854, 2002.

Melosh H.J., Tectonic patterns on a reoriented planet: Mars, Icarus, 73, 745--751, 1980.

Mitchell, D.L., R.P., Lin, C. Mazelle, H. Réme, P.A. Cloutier, J.E.P. Connerney, M.H. Acuña, and N.F. Ness, Probing Mars' crustal magnetic field and ionosphere with the MGS electron magnetometer, J. Geophys. Res., 106, 23,419-23,427, 2001.

Nabighian, M.N., The analytic signal of two-dimensional magnetic bodies with polygonal cross sections: Its properties and use for automated anomaly interpretation., Geophys., 37, 507-517, 1972.

Phillips, J.D., Martian magnetization vectors estimated from Helbig Analysis supports a reversing core dynamo, Fall AGU Meeting Abstract GP21A-0031, 2003.

Richmond, N.C., and L.L., Hood, Paleomagnetic pole positions of Mars, LPSC XXXIV, Abstract 1721, LPI, Houston, 2003.

Roest W.R., J. Verhoef, and M. Pilkington, Magnetic interpretations using the 3-D analytic signal, Geophys., 57, 116-125, 1992.

Shive, P.N., Can remanent magnetization in deep crust contribute to long wavelength magnetic anomalies, Geophys. Res. Lett., 16, 89-92, 1989.

Spada, G., R. Sabadini, and E. Boschi, Long-term rotation and mantle dynamics of the Earth, Mars, and Venus, J. Geophys., Res., 101, 2253-2266, 1996.

Table 3.1

Major characteristics of small isolated anomalies and their source bodies. Lat and Lon denote latitude and east longitude of the center of the model prisms. a and b are the semi-major and semi-minor axis of the model prism, in km. The prisms are 10 km thick. a is the angle between the semi-major axis of the prism and the x axis (East) measured clockwise, in degrees. X, Y, and Z are the east, north, and upward components of the magnetization vector of the prism, in A/m. Reference, (1) is this paper, (2) is *Arkani-Hamed* [2001a], and (3) is *Richmond and Hood* [2003]. Paleopoles show the south pole.

Anomaly	Model Prism					Magnetization			Paleopole		Ref
	Lat	Lon	a	b	α	X	Y	Z	Lat	Lon	
1	-6	66	280	140	160	0.47	1.33	13.15	16	241	1
1	-5	66	315	165	160	-1.00	2.05	12.57	23	255	2
2	-16	70	160	80	160	1.75	5.27	-25.78	7	76	1
2	-15	69	225	165	160	0.23	0.23	-10.95	-12	72	2
3	-28	105	240	120	40	-7.33	7.78	-10.4	20	60	1
3	-27	103	300	225	90	-2.31	1.65	-9.49	-7	78	2
4	-7	216	300	150	0	8.41	-12.45	11.42	-46	346	1
4	-5	214	315	195	0	-0.82	-5.77	13.45	-35	40	2
4	4	215	290	290					-66	47	3
5	-2	323	260	156	50	-9.13	13.18	-9.45	51	260	1
5	-1	322	330	180	40	2.10	-1.34	-11.68	-13	341	2
6	0	344	280	140	40	8.28	-4.44	12.10	-24	110	1
6	2	344	255	180	30	-0.41	0.57	10.78	4	168	2
6	0	341	180	180					70	79	3
7	-45	225	220	110	130	-25.54	-26.10	-21.08	-42	111	1
8	-27	255	260	130	0	15.56	3.50	7.56	17	351	1
9	-33	295	180	108	70	-21.67	-1.80	-18.77	8	182	1

Table 3.1

Figure 3.1

The locations of the magnetic anomalies and their respective paleomagnetic pole positions. a) is the radial component of the high-altitude magnetic data at ~390 km elevation. Note that the color is saturated to better delineate the isolated small anomalies considered in this paper. The small anomalies considered in this paper are shown in this figure. b) displays the locations of the paleomagnetic poles. The red circles denote north poles, blue circles denote south poles. The horizontal axes are east longitude and the vertical axes are latitude.

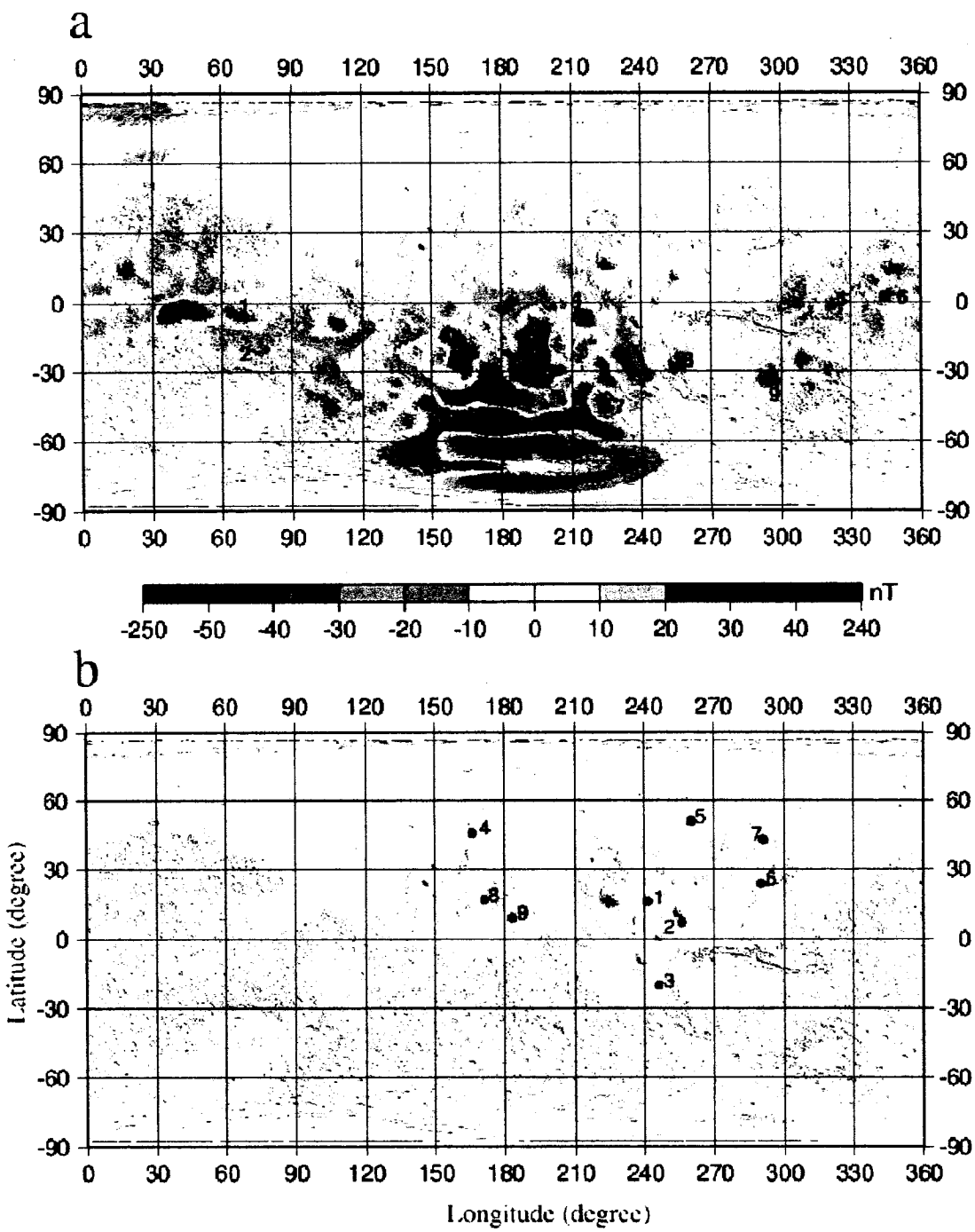
a
0 30 60 90 120 150 180 210 240 270 300 330 360
90 60 30 0 -30 -60 -90
nT
-250 -50 -40 -30 -20 -10 0 10 20 30 40 240
b
Latitude (degree)
Longitude (degree)

Figure 3.1

Figure 3.2

The magnetization vectors of three original elliptical prisms and their equivalent circular models. The elliptical prisms are horizontally magnetized along the semi-major axis, x, the semi-minor axis, y, and 45 degree from the semi-major axis. The solid lines are the directions of the magnetization of the elliptical prisms, and the dashed lines are those of the equivalent circular models. 150 km and 400 km denote the altitude used for the calculations.

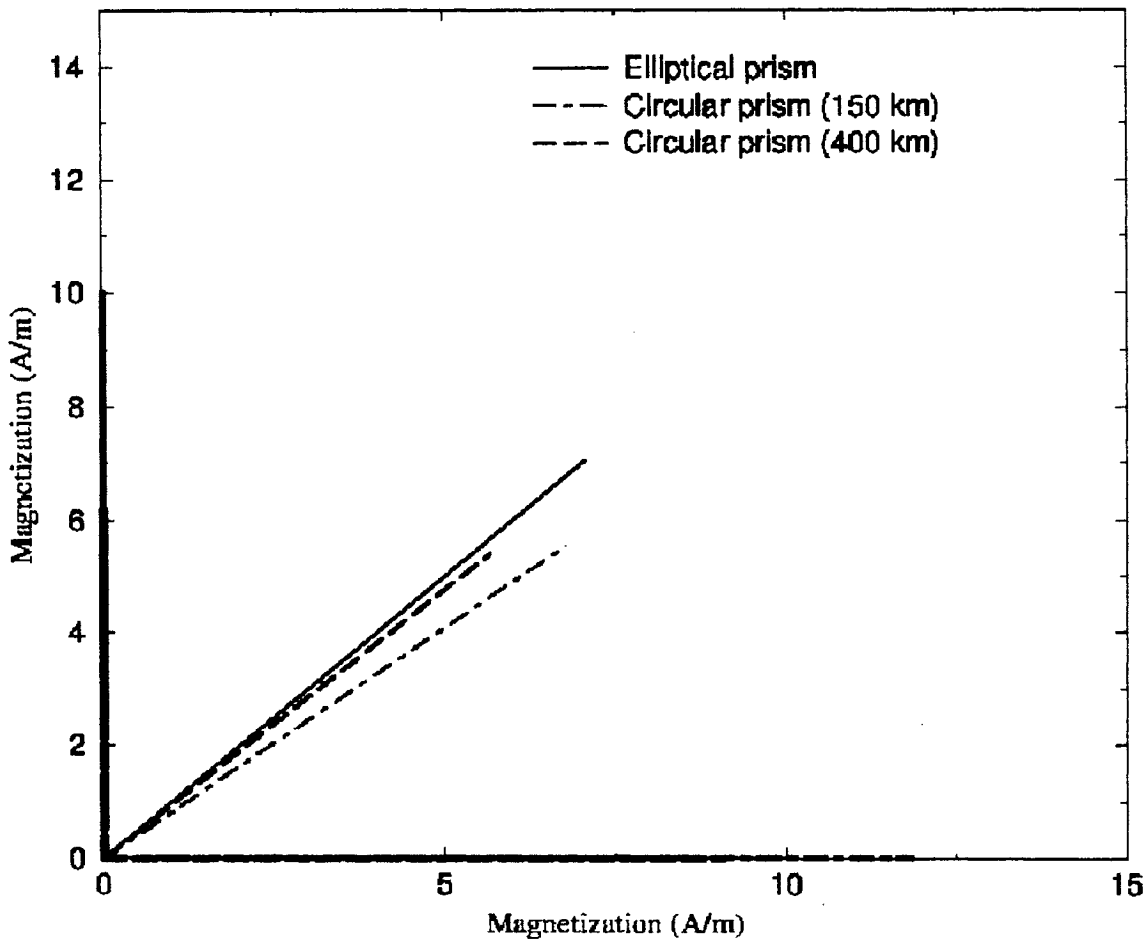
Elliptical prism
Circular prism (150 km)
Circular prism (400 km)
Magnetization (A/m)
Magnetization (A/m)
0
2
4
6
8
10
12
14
0
5
10
15

Figure 3.2

Figure 3.3

The altitude of Mars Global Surveyor over anomaly 5.

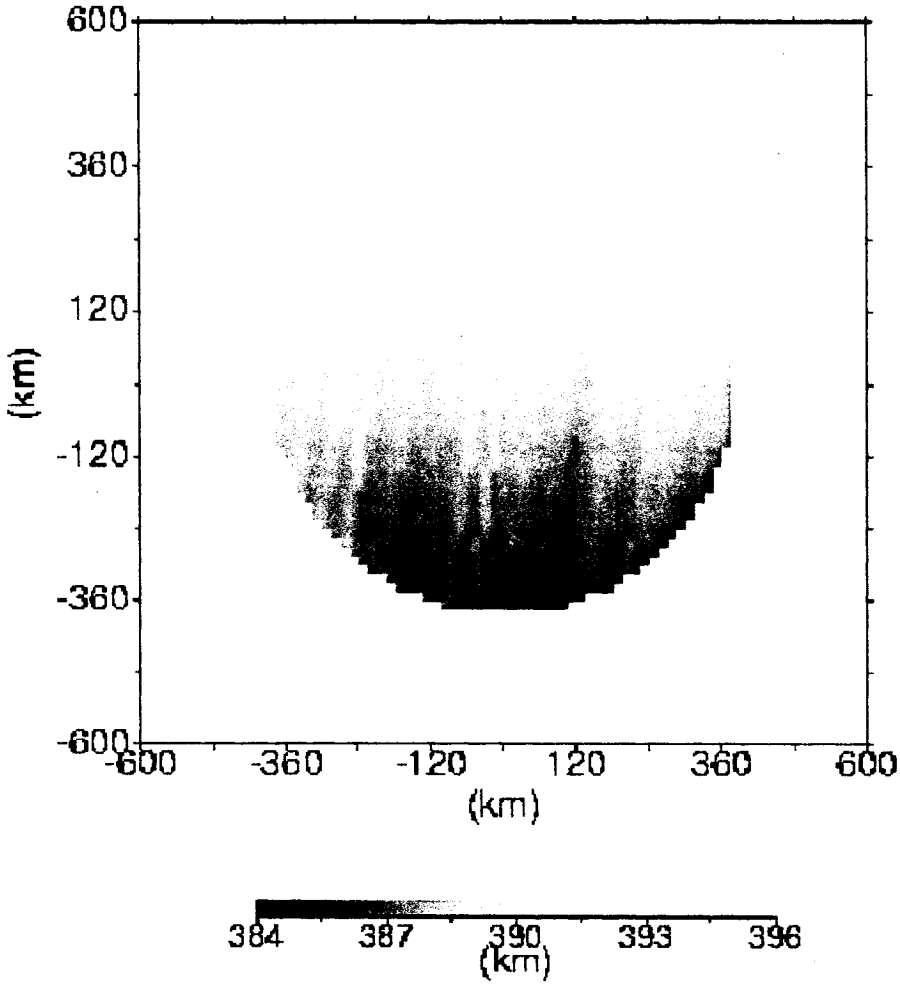
600
360
120
-120
-360
-600
(km)
-600
-360
-120
120
360
600
(km)
384
387
390
393
396
(km)

Figure 3.3

Figure 3.4

The normalized descending minimum misfit value ε versus the semi-major axis of the source body of anomaly 5. It is normalized to the absolute minimum misfit value.

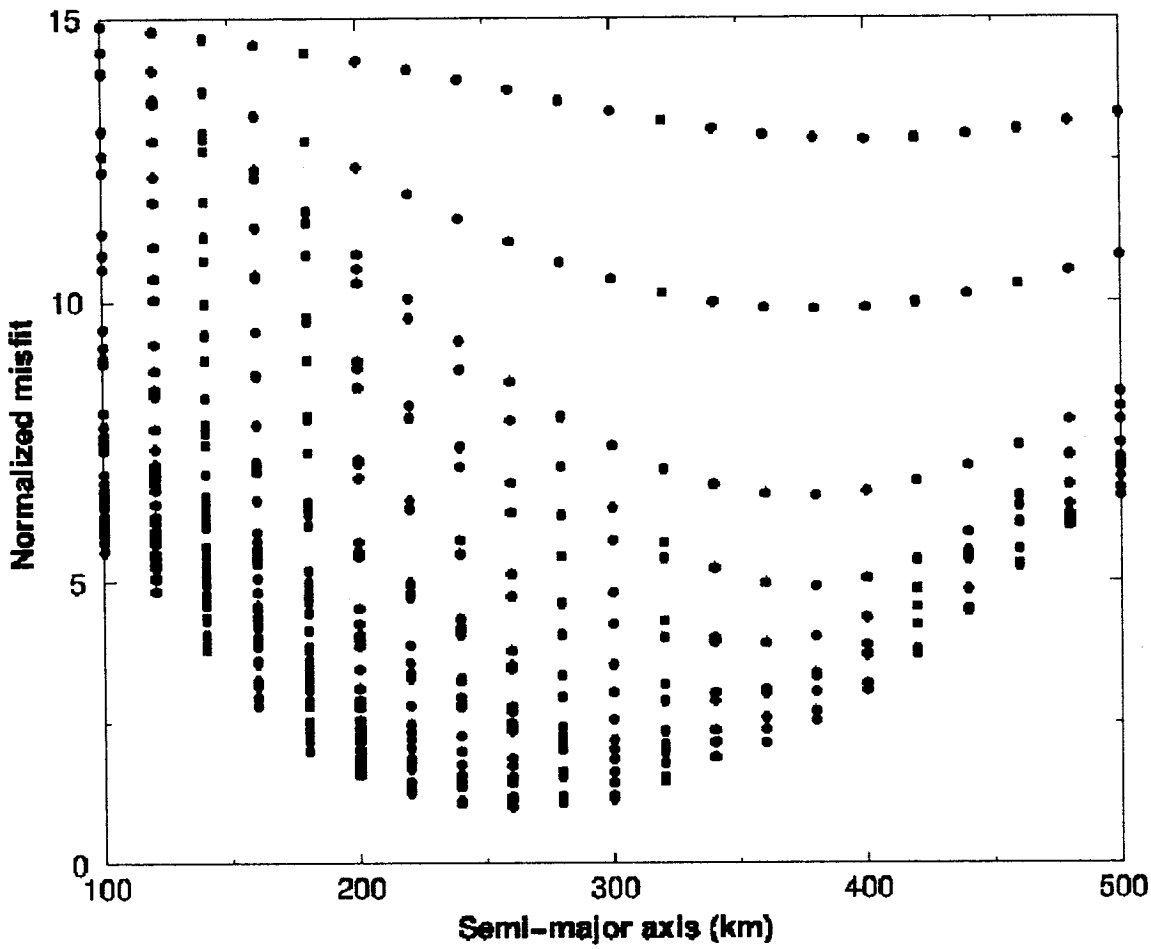
15
10
5
0
100
200
300
400
500
Normalized misfit
Semi-major axis (km)

Figure 3.4

Figure 3.5

The observed high-altitude magnetic data over anomaly 5 (right column) and the model magnetic field (left column) at 400 km elevation. X, Y, Z are the magnetic vector components in the east, north and upward directions, respectively. Only data inside the circular filter shown in the maps are modeled.

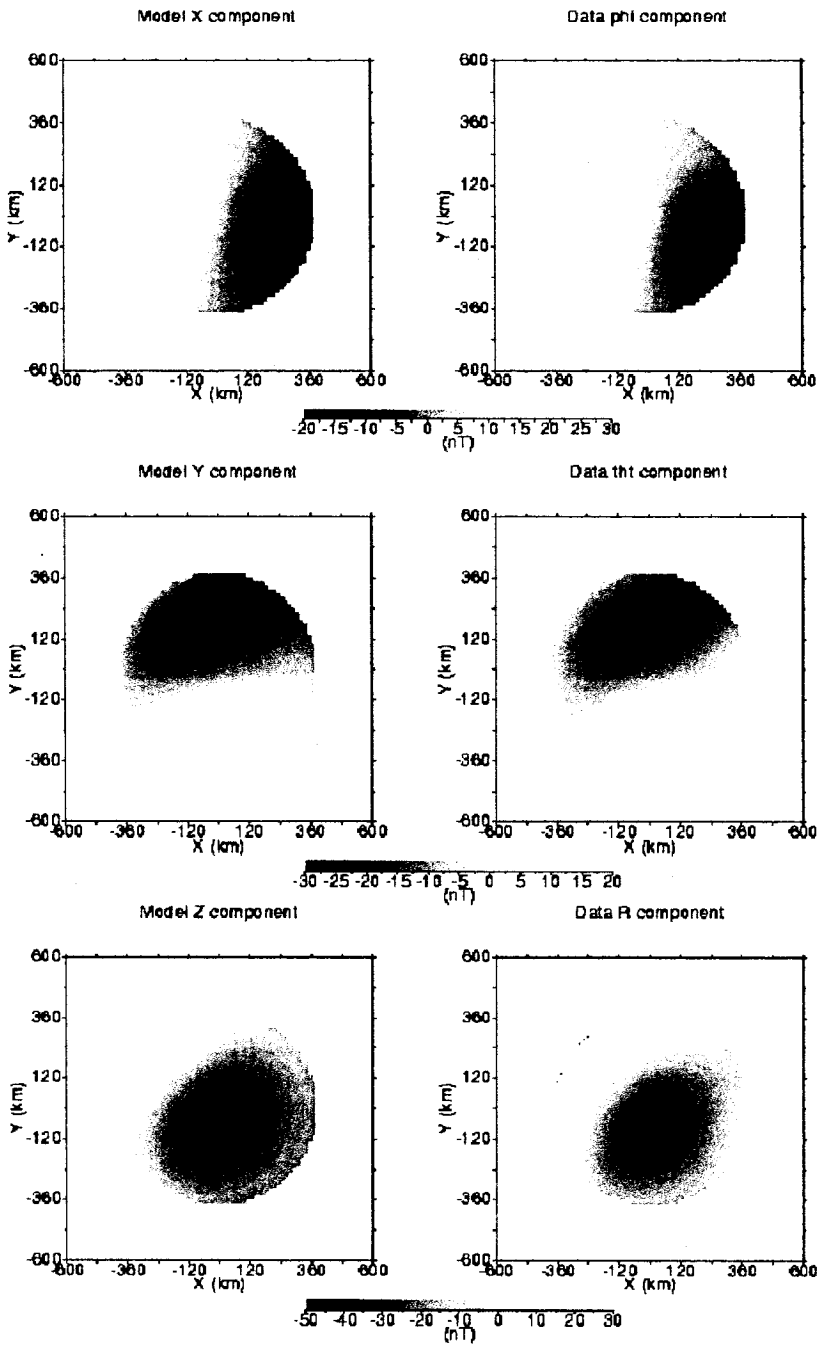
Model X component
Data phi component
Model Y component
Data tht component
Model Z component
Data R component
Y (km)
X (km)
600
360
120
-120
-360
-600
-20 -15 -10 -5 0 5 10 15 20 25 30
-30 -25 -20 -15 -10 -5 0 5 10 15 20
-50 -40 -30 -20 -10 0 10 20 30
(nT)

Figure 3.5

Figure 3.6

The observed low-altitude magnetic data and the model magnetic field along an orbit track passing almost over the center of anomaly 5. The horizontal axes are the distance along the track line.

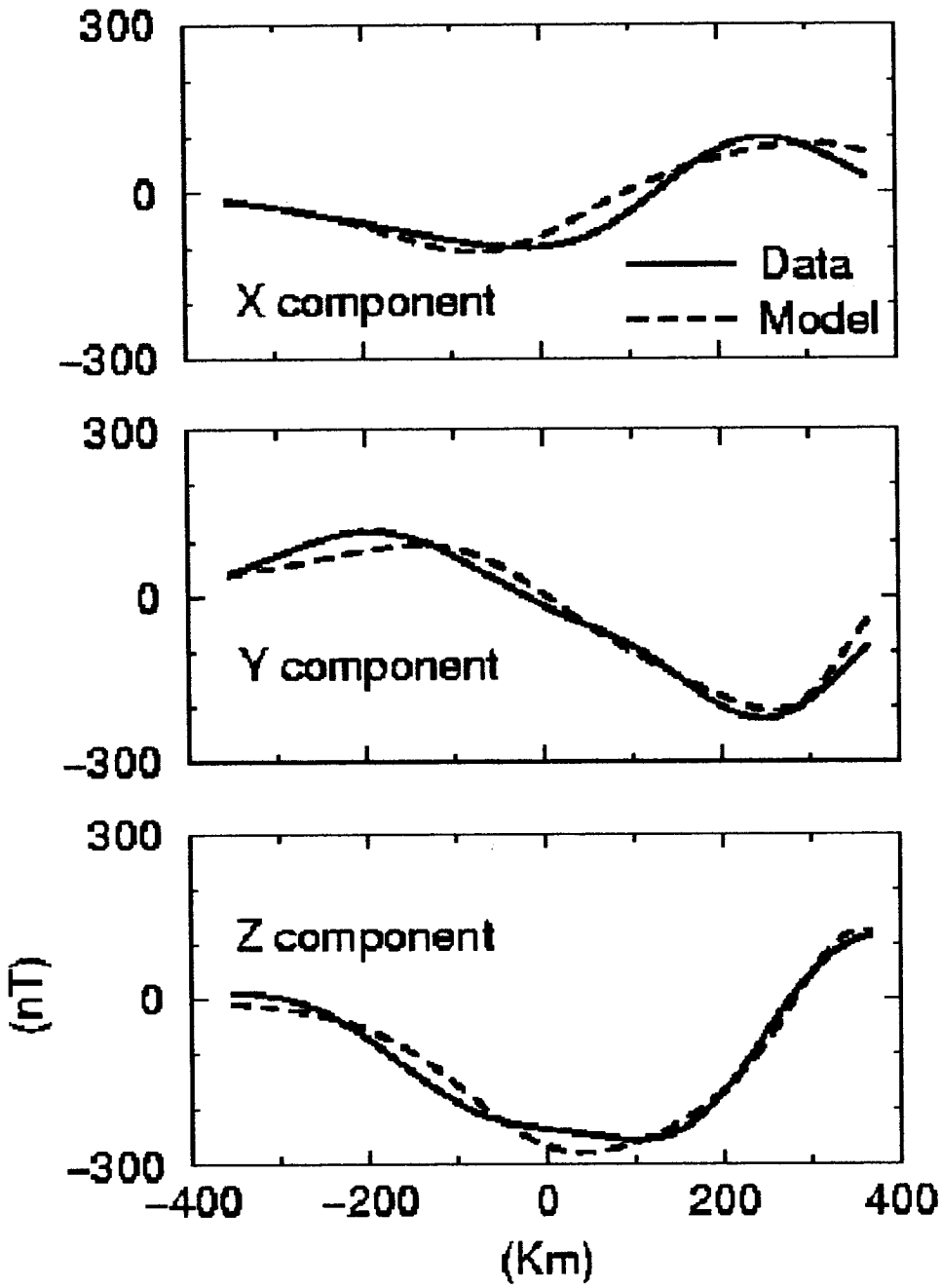
300
0
−300
X component
Data
Model
300
0
−300
Y component
300
0
−300
Z component
(nT)
−400
−200
0
200
400
(Km)

Figure 3.6

Figure 3.7

The paleomagnetic pole positions determined from all models of anomaly 5 with misfit values within 1.5 times the absolute minimum misfit value. The numbers denote the misfit values normalized to the absolute minimum misfit value.

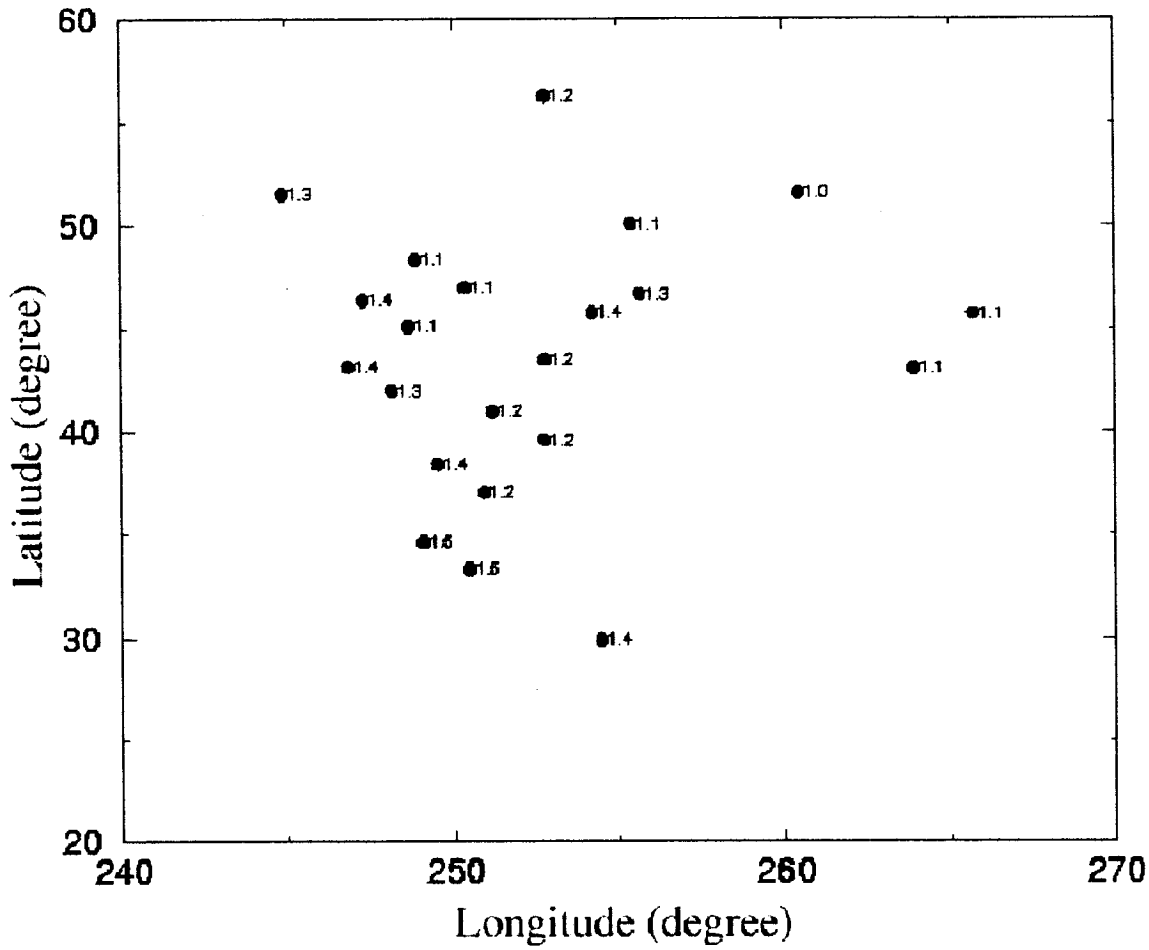
60
50
40
30
20
240
250
260
270
Latitude (degree)
Longitude (degree)
1.2
1.3
1.0
1.1
1.1
1.1
1.4
1.3
1.4
1.1
1.1
1.4
1.2
1.3
1.2
1.2
1.4
1.2
1.5
1.5
1.4

Figure 3.7

Chapter 4: High altitude data modeling

4.1 Introduction

In this second modeling effort I modeled nine isolated magnetic anomalies by using the high altitude data acquired by Mars Global Surveyor (MGS) during the mapping phase portion of the mission between March 1999 and April 2003. From this huge data set I extracted nighttime data to minimize external field contamination and separate the data into two sets of equal size, the first one incorporating data from March 1999 to February 2001 and the second one contain data from March 2001 to April 2003. I calculated the paleomagnetic pole position by assuming that an ancient dipolar core field magnetized the source. For each anomaly I modeled separately the 3 components of the observed magnetic field. I also modeled the radial component of the low altitude data for comparison purposes.

The results support the notion of magnetic pole reversal on Mars. Also most poles are concentrated in the Tharsis region supporting polar motion of 40 deg or more. The issue of data quality is also addressed in this study. The external contamination is removed in the Fourier domain and the effect of contamination by nearby sources is also discussed.

The discovery of important crustal magnetic anomalies by Mars Global Surveyor (MGS) has provided us with a unique opportunity to use those anomalies to study possible polar wandering on Mars. The lack of a global magnetic field, also established by MGS [*Purucker et al.*, 2000], gives us a much direct access to the crustal field.

The goal of this chapter is to show that polar motion on Mars is possible based on modeling magnetic anomalies and to make a global appreciation of the quality of the available data. This last point is especially important because in this study, as in all other studies using MGS data, how contamination is handled will have a profound influence on the final results. The method is discussed and the results presented. I show the result for

two well-isolated anomalies and two badly isolated anomalies. I will conclude by a general discussion of the results. The quality of the data is also address and we show how contamination by nearby sources can affect the calculated pole position.

4.2 Method

In this study I have used all the nighttime high altitude data acquired between March 1999 and April 2003. From this huge data set I extracted night side data for a total of 28,800,000 measurements. The low altitude data were not directly included because they are dayside data and are most probably contaminated by external sources. In the high altitude data I have used all 3 components separately in the modeling. Extensive testing of the space domain algorithm used in this study has shown that it can find the correct pole positions by using only one component of the observed magnetic field. See table 4.1 for some of the results of this testing.

The high altitude data set is separated in almost two equal parts. The first one (HA1) contains nighttime data acquired from March 1999 to February 2001 and the second part (HA2) contains data from March 2001 to April 2003. Technically those 2 data sets should be perfectly identical but because of time dependant external contributions and noise they are not. Comparing the two sets in the Fourier domain and removing any frequencies that do not correlate with at least a factor of 0.8 gives an opportunity to quantify and remove external field contamination. Both HA1 and HA2 are binned on a 0.5 by 0.5 deg grid and the mean value of the grid is determined after removing outlier points that are more than two standard deviations from the mean. Removing the outliers is the first step in removing external contamination. For each of the nine anomalies I extract data from both HA1 and HA2. I then compare the two anomaly sets obtained in the Fourier domain and remove all the frequencies that do not show a high degree of correlation. Going back to the space domain gives two more anomaly data sets. They are the smoothed sets where external contamination have been minimize but certainly not totally removed.

Now for each component of the magnetic field 4 models are obtained, 2 from the original anomaly sets and 2 more from the smoothed anomaly data sets. This result in 12 paleomagnetic pole positions. For comparison purposes I have also modeled the radial component of the low altitude data. In this case the data is binned in the same way as before and the outliers removed. However Fourier domain smoothing is not performed due to the lack of sufficient coverage. All 13 poles obtained should coincide perfectly if the anomalies were perfectly isolated and the data completely clean.

The actual modeling is performed by least square fitting the data with the magnetic field generated by a model elliptical prism. The basic modeling method is the same that was used in chapter 3. Before modeling, the data is transferred from a global spherical coordinate reference frame with the origin at the center of mass of the planet to a local Cartesian frame with the origin at the position of the anomaly on the surface. The model prism's top is place at the surface of the elliptical Mars and has a thickness of 10 km. The actual value of the prism thickness will not have any influence on the pole position found even though it certainly influence the intensity of the magnetization. Not placing the top of the prism at the surface would not change the result for the pole position either. It has been argued that the Martian surface and the first few kilometers of the crust might not be magnetic since there is no apparent correlation between magnetic anomalies and topography [*Arkani-Hamed*, 2002 ; *Nimmo and Gilmore*, 2001].

The position, shape and size of the model prism are changed and a new model evaluated. At that phase the data is circularly filtered to further minimize contribution form other nearby sources. Only the data inside the filter is actually used in the modeling. The model field is then compared to the observed field and the misfit calculated. The model with the smallest misfit is retained. The prism is moved inside a 320 km by 320 km square at 40 km intervals. The semi-major axis of the ellipse is changed from 100 to 500 km at 20 km intervals. The semi-minor axis is changed from half the semi-major axis to the semi-major-axis at 10% increment intervals. Finally the prism is rotated from 0 to 180 degree at 10 degree intervals.

4.3 Quality of the models

Evaluating the quality of a model, that is how good is the fit between the model field obtained with the best-fit prism and the data actually modeled is subjective. The least square fitting parameter value is also dependent on the number of data points. In this study I define a number called the quality index Q_I.

$$Q_i = \frac{\left[\sum B_{data}^2\right]^{1/2}}{\left[\sum (B_{data} - B_{\mathrm{mod}})^2\right]^{1/2}}$$

where B_{data} is the component (X,Y or Z) of the data and B_{mod} the same component of the best-fit model for the same data point. In theory a model that fits the data perfectly would have a Q_I factor equal to infinity. In practice however there is no need to go this high to get a very good model. This study has shown that models with Q_I lower than 25 are questionable. Models with $25 \leq Q_i \leq 50$ are usually acceptable while Q_I over 50 gives good models. Q_I over 100 represent very good models that fit the data very well. Models with Q_I over 100 can be used with confidence to find the pole positions. Not surprisingly models estimated with the low pass filtered data shows the highest values for Q_I. This observation helps in validating the correctness of the procedure used to low pass filter the data. This value is interesting in many respects. It gives an immediate appreciation of the quality of the fit between model and data and permits a selection of the models for pole positions evaluation based on less subjective criteria. This value is also independent of the number of data points that the model is trying to fit. A low value of Q_I for the filtered data is indicative of a non-isolated and/or very contaminated anomaly. Also how that number changes between the unsmoothed and smoothed data models gives an indication on how efficient the smoothing has been and gives us an idea of the contamination in the original unsmoothed data. Two examples of anomalies I consider well isolated and two anomalies that are not well isolated are presented.

4.4 Validating the method

The space domain algorithm calculates the magnetic field of the model prism by first calculating the magnetic field of a prism of infinite depth with it's top at the top of the actual prism and then repeat the calculation for an infinite prism with negative susceptibility and top at the bottom of the actual prism. The results of this program are checked with another program that calculates the magnetic field by using the Talwani algorithm [*Talwani*, 1965]. a very different algorithm than the one described above. My supervisor Arkani-Hamed wrote the original modeling program and I tested it myself . I wrote the second program based on the Talwani method. The two programs do not share a single line of code. However, for all practical purposes they give identical results. See appendix E for more details on the calculation of magnetic fields.

Before actually modeling the data it is important to make sure that modeling each component separately will give the same pole position. For this purpose I generated all three components of a magnetic field produced by an elliptical prism. The prism is located at position 0,0 in the local Cartesian frame (X east, Y north and Z perpendicular to the surface). The semi-major axis is 320 km, semi-minor axis is 210 km orientation of the prism is 20 deg counterclockwise from the X axis. The prism is placed at latitude 0 deg and longitude 180 deg on a sphere. The thickness of the prism is 10 km. The magnetic field was calculated at 400 km altitude with the Talwani method. The three components of the magnetization are changed to make the test as general as possible. Eight models are presented in table 4.1. All models uses the same prism but with a different magnetization. The results indicate that the algorithm functions correctly. The method used to find the paleomagnetic pole position from the magnetization components is described in detail in chapter 7 of *Butler* [1992].

4.5 Results and analysis

In this section I present 2 anomalies that I consider well isolated and 2 others that do not behave as well. I will also discuss the general quality of the data and pole distribution for

all 9 anomalies. Figure 4.1 identify the position of all the modeled anomalies on a topographic map of Mars overlaid by the radial component of the observed magnetic field at 400 km altitude. From now on the letter A followed by number 1 to 9 as represented on figure 4.1 will identify the anomalies. Anomalies A4 and A5 seems to be well isolated while anomalies A6 and A7 have very busy neighborhoods, especially A7 with it's location near the most intense magnetic part of Mars in the southern hemisphere. Appendix C shows that it is quite possible that this anomaly may not even have been produced by an independent source body. It is more likely the result of the vector sum of the magnetic fields produced by many other source bodies in the neighborhood.

4.5.1 A4 and A5: two well isolated anomalies

I now present the modeling results for anomaly A4 and A5, which show a good fit between model and data. The results for the 13 models obtained for each anomaly is presented in table 4.2.

One can immediately see the effect of external contamination on the data by looking at the big difference between the Q_i factors of the smoothed and unsmoothed data. The big improvement in the Q_i factor indicates that a lot of exterior contamination has been removed by the filtering process. Figure 4.2 present graphically the results given in table 4.2 for A5. The A5 figure shows that the poles obtained form the radial and theta component of the data are well clustered but the poles obtained with the phi component are not, indicating that external contamination is more prevalent in the phi component. The radial and theta poles do not however coincide which mean that the anomaly is not totally isolated. Another observation is the very low quality factor of the low altitude data model, which is probably due to a very uneven coverage at lower altitude and the fact that low altitude data is day side data. The A5 anomaly is as close as we can hope of being well isolated. Figure 4.3 present maps of models versus data for the radial component models of anomaly A5 which shows a very good fit. Scatter diagrams of the models and data are presented in figure 4.4. The shape and intensity of the anomaly is well represented by the model. As expected the smoothed data shows a very good

correspondence between data and model. This also clearly illustrated in the scatter diagrams of figure 4.4.

4.5.2 A6 and A7, two badly isolated anomalies

Anomalies A6 and A7 are not well isolated and this shows in the low quality factor values and generally not so good fit between data and model. Table 4.2 present the 13 pole positions for each anomaly. In general the models presented here have low Qi values and show only small improvements after filtering, indicating either that the external contamination was low to start with or that contamination was small compared to the effects of nearby sources. Filtering in the Fourier domain does not remove the contamination due to nearby sources but only attenuate time varying external contamination. I feel that these anomalies are simply not well isolated and in the end these results show that the method works correctly. Figure 4.5 presents graphically the results of table 4.2 for anomaly A7. Figure 4.6 presents a comparison between data and model for the radial component of the A7 anomaly. The anomaly is very twisted by nearby sources and it would take a prism with a much more complex shape than an elliptical prism to model it adequately. Figure 4.6 shows the scatter diagrams of the data and models presented in figure 4.5. It shows that the negative values which represent the major part of the anomaly, are not modeled correctly while the positive values are better represented by the model. See appendix C for more comments on anomaly isolation.

4.6 Global analysis

Figure 4.7 presents all of the poles obtained by modeling the high altitude radial component of the data. I choose to show the radial components poles because I feel that this component has the least external contamination. One can see that in most cases, for a given anomaly, the poles are clustering. This indicate that the exterior contamination was low for those anomalies. However some anomalies still show some differences between the poles of the smoothed and unsmoothed data sets. This shows that external contamination is still present in the data but that most of it has been removed by the

filtering process. This remaining external contamination could possibly have been eliminated by a more optimal choice of the uncorrelated frequencies that were removed by the filtering process. On a more global scale one can see that most of the poles are clustering in the Tharsis region. The clustering is not as tight as the one proposed by *Arkani-Hamed* [2001b] but this result and the one proposed by *Arkani-Hamed* [2001b] argues in favor of a rotational pole in this region. Results by *Melosh* [1980] and *Hood and Zacharian* [2001] generally agree with this affirmation. This would indicate that Tharsis originated much higher in the northern hemisphere, perhaps as much as 40 to 50 degrees. This conclusion however does not tell us if Tharsis itself, the volcanoes on it or a combination of both, is responsible for the inferred polar motion. However, as has been pointed out by many investigators Tharsis is more likely not fully compensated and Tharsis as a whole remain the prime suspect for the cause of polar motion on Mars.

It is important to note that contamination by nearby sources is not removed by the filtering process and is still present in the map of figure 4.8. Removing nearby contamination would conceivably improve the clustering shown in the figure. As pointed out earlier this is a very difficult task as this kind of problem is very non unique. As long as there is no supplementary data that would help us to put constraint on the shape, size and magnetization of a given anomaly the pole positions calculated, by whatever method, can only be considered preliminary. Unfortunately such new information is unlikely to come in the near future. To illustrate this important problem and try to better constraint what is an isolated anomaly in practice, consider the following problem. I have calculated, at many different altitudes, the radial component of the combined magnetic field of two elliptical prisms. The two prisms used are the model prisms obtained by *Arkani-Hamed* [2001b] for it's M4 and M5 anomalies. The M4 anomaly is located at lat =-5 and long =66 and M5 is located at lat = -15, long = 69. The two prisms parameters are given in table 4.3. The orientation of the prisms is measured counterclockwise from an horizontal axis in the eastward direction.

Figure 4.8 illustrate the combined field at 100, 200, 400 and 600 km altitude. For each map the scale chosen is such that it represent exactly the total data range from the

minimum to the maximum of each map. The models obtained by modeling each the positive lobe of each data sets are presented in table 4.4 . The paleopole obtained change with altitude, clearly indicating that the two bodies contaminate each other. *Arkani-Hamed* [2001b] obtained a pole position at (23 , 255) deg. If the source was not contaminated we would obtain the same pole position whatever the altitude as long as we are operating within reasonable limits. For this particular example the reason for the changing paleopoles can be seen in figure 4.8. As we go higher and higher one can clearly see the elliptical lobes of each anomaly rotate in the counterclockwise direction. This new orientation differ considerably from the original orientation of the prisms. Therefore the actual source prisms would not be correctly identified by the modeling.

This simple example easily shows that the low altitude data has more weight in the final result of the modeling of the data. However, in practice, one should not use simultaneously the low and high altitude data in a model because they are affected differently by nearby sources contamination. Combining both data sets will give an erroneous answer. Critical steps must be taken to remove external field contamination as well as to minimize contribution by nearby sources. I have done so in this study by removing external contamination in the Fourier domain and using a circular filter in the space domain to minimize contamination by nearby sources. Modeling the data as is will introduce appreciable errors. In the case of the M4 and M5 anomalies one must also not discount the possibility that the two lobes actually comes from only one source since the lobes are similar in shape, size and orientation. This view has been criticized by *Arkani-Hamed* [*Personal communication*] who argue that such a unique source would be too big to have been uniformly magnetized by the ancient core field. However there is no known size limit for uniformly magnetized body. The one source argument is also not supported by *Langlais et al.* [2003] (see their figure 6, radial component) whose surface magnetization map clearly shows two source bodies in that region.

Based on the modeling results I would suggest that an anomaly would be sufficiently isolated if it gives the same paleopole when modeled independently with low and high altitude data. As mentioned earlier modeling different components of the observed

magnetic field should yield the same paleopole position if the anomaly is isolated. The closest that I came to this ideal situation is for anomaly A5 which show a very good isolation. The paleopole obtained for the different high altitude components are reasonably close. Moreover the paleopole obtained generally agrees with the one obtained by *Arkani-Hamed and Boutin* [2004] who used both the low and high altitude data sets. For A5 I obtained a pole position at latitude 50° and longitude 269°, supporting polar motion of at least 40 deg. Although some of the poles obtained in this study can be different than the one obtained by other investigators, they still show clustering around Tharsis. *Arkani-Hamed* [2001b] ,by using a spherical harmonics model generated from low altitude data alone, has shown that poles cluster in that region. Considering that clustering was obtained separately for both low and high altitude data one can have more confidence in that result. If verified in the future, clustering of the poles would indicate a lack of major plate tectonic events on Mars. This support the arguments that Mars is, and probably always has been, a one plate planet. The results also make a case for magnetic field reversal on Mars as the cluster over Tharsis has both south and north poles. Figure 4.7 presents the pole positions obtained with the radial components models for each anomaly. Poles for anomalies A1, A5 and A9 are south magnetic poles. The other anomalies are represented by their north magnetic poles.

This study has also demonstrated that the use of elliptical prisms is better than circular one. One must also move the prism to find the best possible model. See figure 4.9 for a comparison of the results obtained for different prisms with the data from the A5 anomaly.

4.7 Conclusion

I have calculated the paleopole positions of 9 magnetic anomalies by modeling in the space domain the 3 components of the night side observed magnetic field measured by MGS. For each component I have calculated the poles for smoothed and unsmoothed data sets. This gave me the opportunity to evaluate the external filed contamination of the

data. The results show that for most anomalies contamination is low, since for a given component the poles of most anomalies cluster.

However, the filtering process used for removing external field contamination did not remove contamination by nearby sources. Most anomalies show different pole positions for different components of the data. Since external filed contamination has been mostly removed that difference must be largely related to nearby sources. Using an isolated anomaly is essential if the paleopole positions calculated are to mean anything. Assuming that the axis of rotation was truly aligned with the dipole axis of the ancient global field during Martian history then only one good anomaly is, in theory, sufficient to make a case for polar motion on Mars. In this study, anomaly A5 comes very close to the kind of anomaly we need. Most of the 13 poles calculated for this anomaly comes very close to each other indicating that the anomaly is well isolated. Although it is possible to make a case for polar motion on Mars based on other anomalies the A5 anomaly suggests polar motion of up to 40 deg. Global clustering of the poles is also supported by this study. Although clustering is not as good as previously reported in other studies, I feel that the results still support it. Pole reversal is also supported by the results. Better resolution measurements and better techniques to remove nearby contamination would go a long way to solve this issue. A practical and usable way to express how well an anomaly is isolated would also help a lot. An "isolation factor", similar to the quality index used to asses the quality of a model is, I feel, urgently needed.

The paleopole positions indicate the lack of plate tectonics on Mars or at the very least that plate tectonics has not been a major contributor to Martian geophysical history. The lack of plate tectonic is indicative of a Martian interior that did not generate enough heat to drive convection in the mantle at a high enough rate to brake the one plate and produce tectonic as we know it here on Earth. If the heat production was high then the Martian interior must have evacuated it very quickly leading to a quick shutdown of convection in the mantle and of the global magnetic core field. This interpretation is consistent with most thermal evolution models which predict that most important events on Mars happened very quickly, probably within the fist 500 My.

Table 4.1

Test results of the space domain algorithm. The prism used for this test is described in the text. The magnetization is varied in the 8 quadrants. The magnetization values (in A/m) are indicated above the results of each test. Results in parenthesis are the expected latitude and longitude of the magnetic south poles. The very small differences between estimated and expected values is consistent with numerical approximations.

Component	Pole latitude	Pole longitude	Pole latitude	Pole longitude
	Jx = 4 , Jy = 9 , Jz = 5		Jx = 4 , Jy = 9 , Jz = -5	
X	62.32 (62.34)	302.01 (302.00)	62.32 (62.34)	237.98 (237.99)
Y	62.45 (62.34)	302.17 (302.00)	62.45 (62.34)	237.82 (237.99)
Z	62.38 (62.34)	302.00 (302.00)	62.38 (62.34)	237.91 (237.99)
	Jx = 4 , Jy = -9 , Jz = 5		Jx = 4 , Jy = -9 , Jz = -5	
X	-62.33 (-62.34)	301.97 (302.00)	-62.33 (-62.34)	238.02 (237.99)
Y	-62.30 (-62.34)	301.93 (302.00)	-62.30 (-62.34)	238.06 (237.99)
Z	-62.35 (-62.34)	302.00 (302.00)	-62.35 (-62.34)	237.99 (237.99)
	Jx = -4 , Jy = -9 , Jz = 5		Jx = -4 , Jy = -9 , Jz = -5	
X	-62.32 (-62.34)	57.98 (57.99)	-62.32 (-62.34)	122.01 (122.00)
Y	-62.45 (-62.34)	57.82 (57.99)	-62.45 (-62.34)	122.17 (122.00)
Z	-62.38 (-62.34)	57.91 (57.99)	-62.38 (-62.34)	122.00 (122.00)
	Jx = -4 , Jy = 9 , Jz = 5		Jx = -4 , Jy = 9 , Jz = -5	
X	62.33 (62.34)	58.02 (57.99)	62.33 (62.34)	121.97 (122.00)
Y	62.30 (62.34)	58.06 (57.99)	62.30 (62.34)	121.93 (122.00)
Z	62.35 (62.34)	57.99 (57.99)	62.35 (62.34)	122.00 (122.00)

Table 4.1

Table 4.2

13 paleopoles obtained for anomalies A4 to A7. The latitude, longitude and Qi factor of model are presented. For each component the models are from left to right: HA1, HA2, HA1 smooth and HA2 smooth. The last column is the low altitude data radial model.

A4	Radial				Phi				Theta				LA
Lat	-26	-26	-26	-26	25	38	30	31	-38	-39	-39	-38	-34
Long	77	74	76	75	75	54	75	73	52	343	53	343	84
Qi	59	41	110	89	76	37	311	185	51	32	67	55	13

A5	Radial				Phi				Theta				LA
Lat	52	50	52	50	31	18	30	51	68	67	68	68	0
Long	269	267	268	267	269	269	269	278	287	285	288	291	254
Qi	94	70	315	343	106	55	337	550	81	51	235	232	7

A6	Radial				Phi				Theta				LA
Lat	-24	-22	-24	-26	2	-12	-5	3	58	56	67	49	-62
Long	90	91	90	97	73	73	56	53	232	232	243	238	97
Qi	12	13	14	17	17	20	44	49	17	18	45	28	12

A7	Radial				Phi				Theta				LA
Lat	-19	-19	-19	-19	-13	-12	-13	-12	-29	-28	-35	-30	-7
Long	122	123	123	122	125	125	125	126	320	320	320	315	307
Qi	8	8	9	8	72	58	97	87	33	29	51	47	5

Table 4.2

Table 4.3

Parameters of the two test prisms. The prisms are the M4 and M5 model prisms of Arkani-Hamed (2001b).

Anomaly	M4	M5
Latitude , Longitude (deg)	-5 , 66	-15,69
Semi-major axis (km)	320	220
Semi-minor axis (km)	160	160
Inclination (deg)	160	160
Magnetization (Mx , My , Mz) (A/m)	-1.00 , 2.05 , 12.57	0.23 , 0.23 , -10.95
Pole latitude and longitude (deg)	23 , 255	-12 , 72

Table 4.3

Table 4.4

Paleomagnetic pole positions obtained by modeling the two test prisms of table 3 at different altitudes.

Altitude	100	200	400	600
Semi-major axis (km)	320	340	320	260
Semi-minor axis (km)	160	170	160	130
Inclination (deg)	160	160	160	160
Magnetization (Jx,Jy,Jz) (a/m)	-0.84 , 1.75 , 12.79	-3.9 , 5.3 , 11.6	-4.0 , 12.6 , 10.1	-5.6 , 21.3 , 11.9
Pole latitude and longitude (deg)	20 , 253	41 , 282	66 , 291	72 , 300

Table 4.4

Figure 4.1

Position of the magnetic anomalies on the surface of Mars. Anomalies A4 and A5 are considered well isolated on the basis of the modeling results. Anomaly A6 and A7 with there low Q_i factor are considered less well isolated.

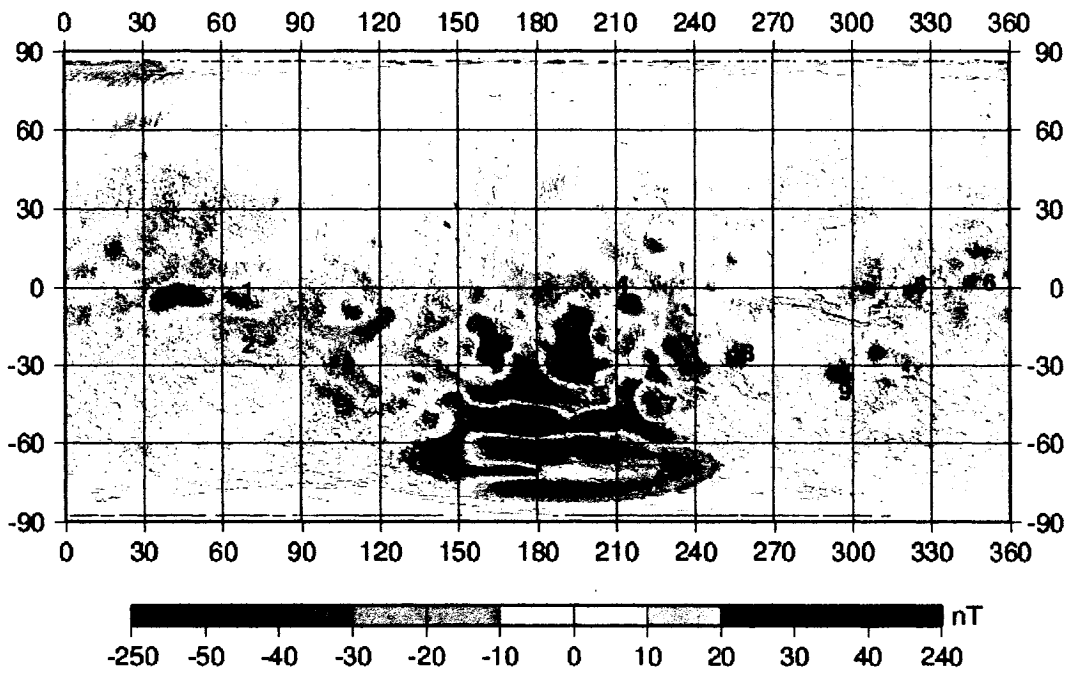
0 30 60 90 120 150 180 210 240 270 300 330 360
90
60
30
0
-30
-60
-90
nT
-250 -50 -40 -30 -20 -10 0 10 20 30 40 240

Figure 4.1

Figure 4.2

The 13 pole positions of table 4.2 for anomaly A5 and A6. First panel represent A5 models. In each panel squares represent phi models, Triangles represent theta models. Circle is the low altitude data model. The star symbols represent the position of the anomaly. The squares with thick borders represent the radial models. This information is also available in table 4.2.

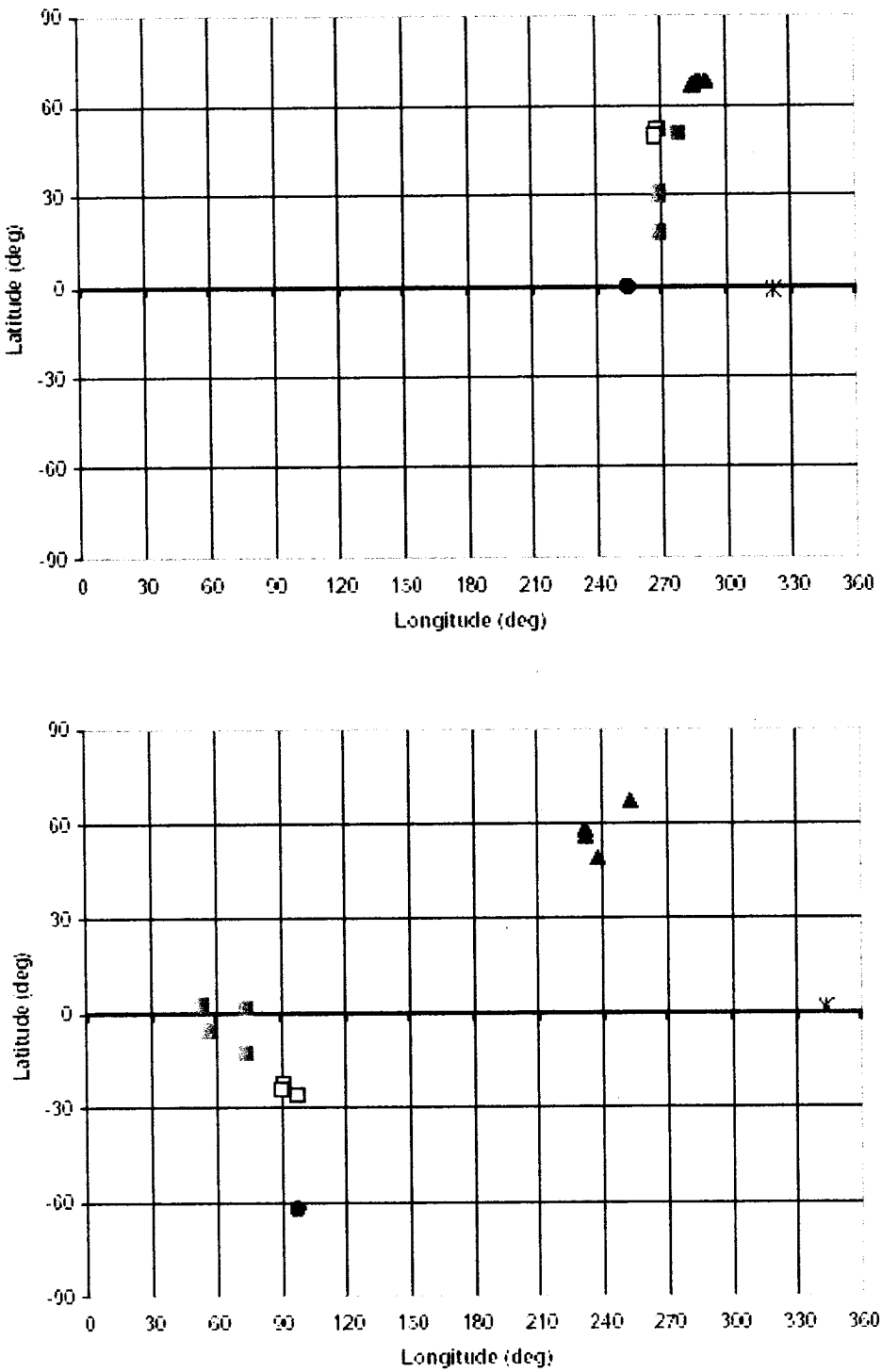
90
60
30
0
-30
-60
-90
Latitude (deg)
0 30 60 90 120 150 180 210 240 270 300 330 360
Longitude (deg)
90
60
30
0
-30
-60
-90
Latitude (deg)
0 30 60 90 120 150 180 210 240 270 300 330 360
Longitude (deg)

Figure 4.2

Figure 4.3

Comparison between data and model for the Z models of the A5 anomaly. Only the data actually used for modeling is represented.

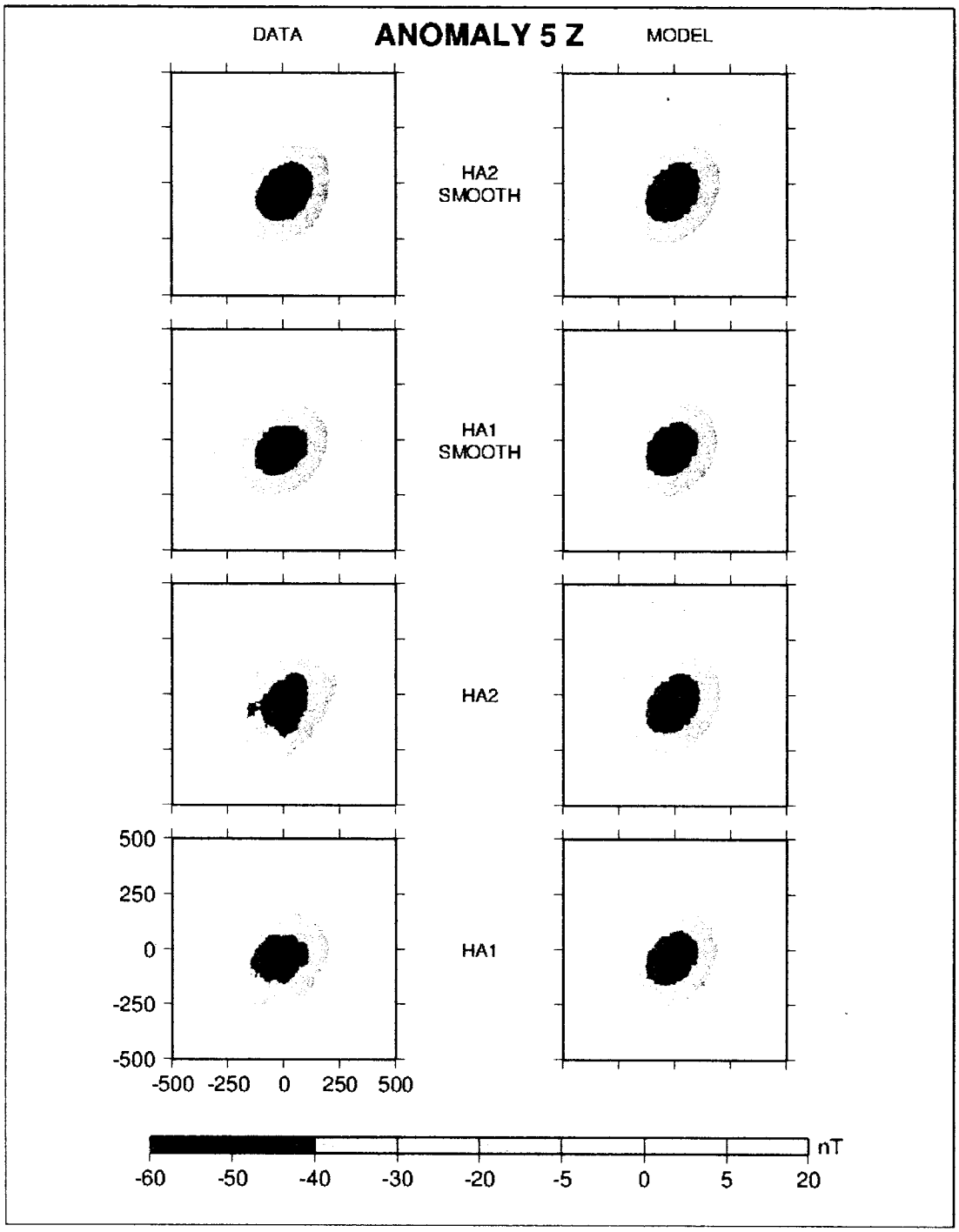
DATA
ANOMALY 5 Z
MODEL
HA2
SMOOTH
HA1
SMOOTH
HA2
HA1
500
250
0
-250
-500
-500 -250 0 250 500
nT
-60 -50 -40 -30 -20 -5 0 5 20

Figure 4.3

Figure 4.4

Scatter diagrams of the data and models presented in figure 4.3. The black line has a slope of 1 and Y intercept 0 and represent a perfect model. Data is on the horizontal axis and model on the vertical axis.

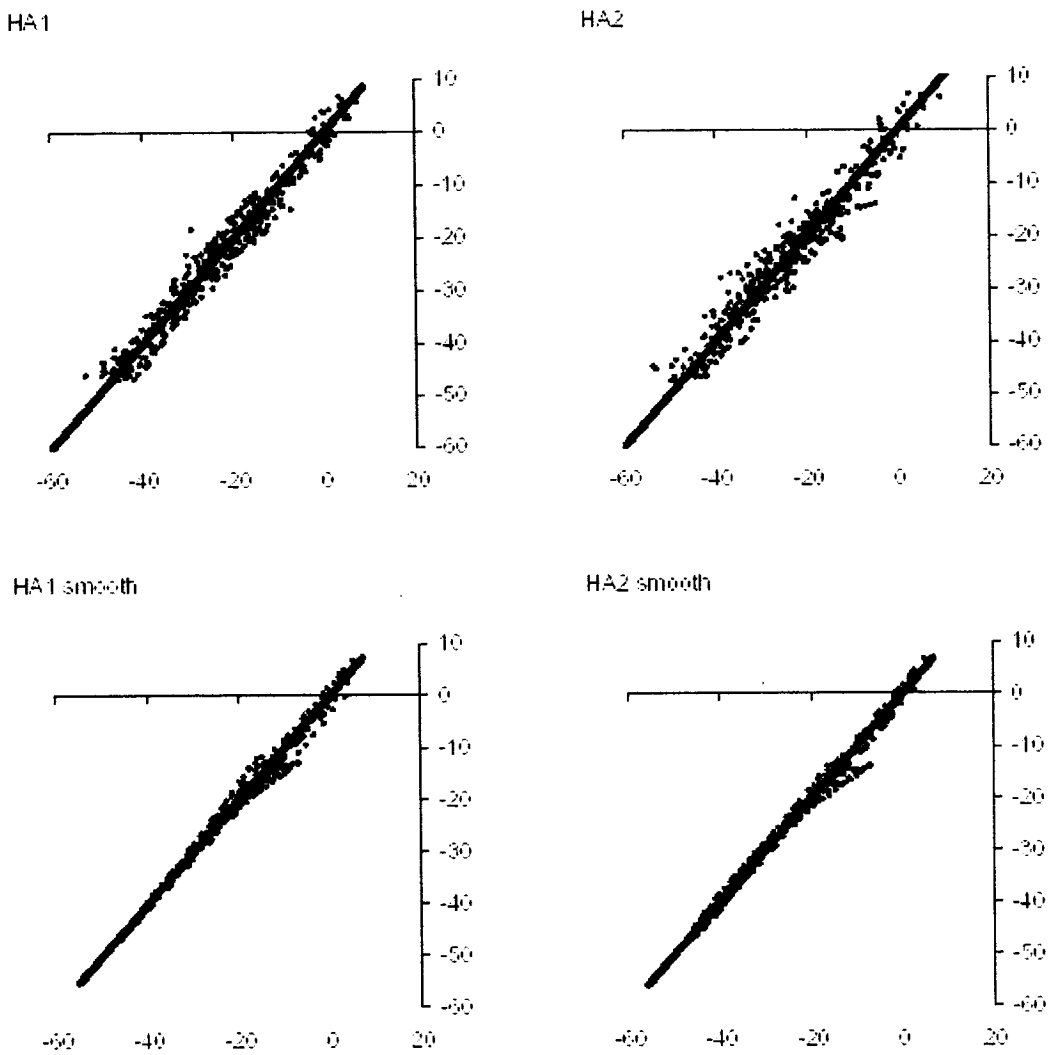
A5 Z models
HA1
HA2
HA1 smooth
HA2 smooth
10
0
-10
-20
-30
-40
-50
-60
-60
-40
-20
0
20

Figure 4.4

Figure 4.5

Comparison between data and model for the Z models of the A7 anomaly. As in figure 4.3 only the data actually used for modeling is represented.

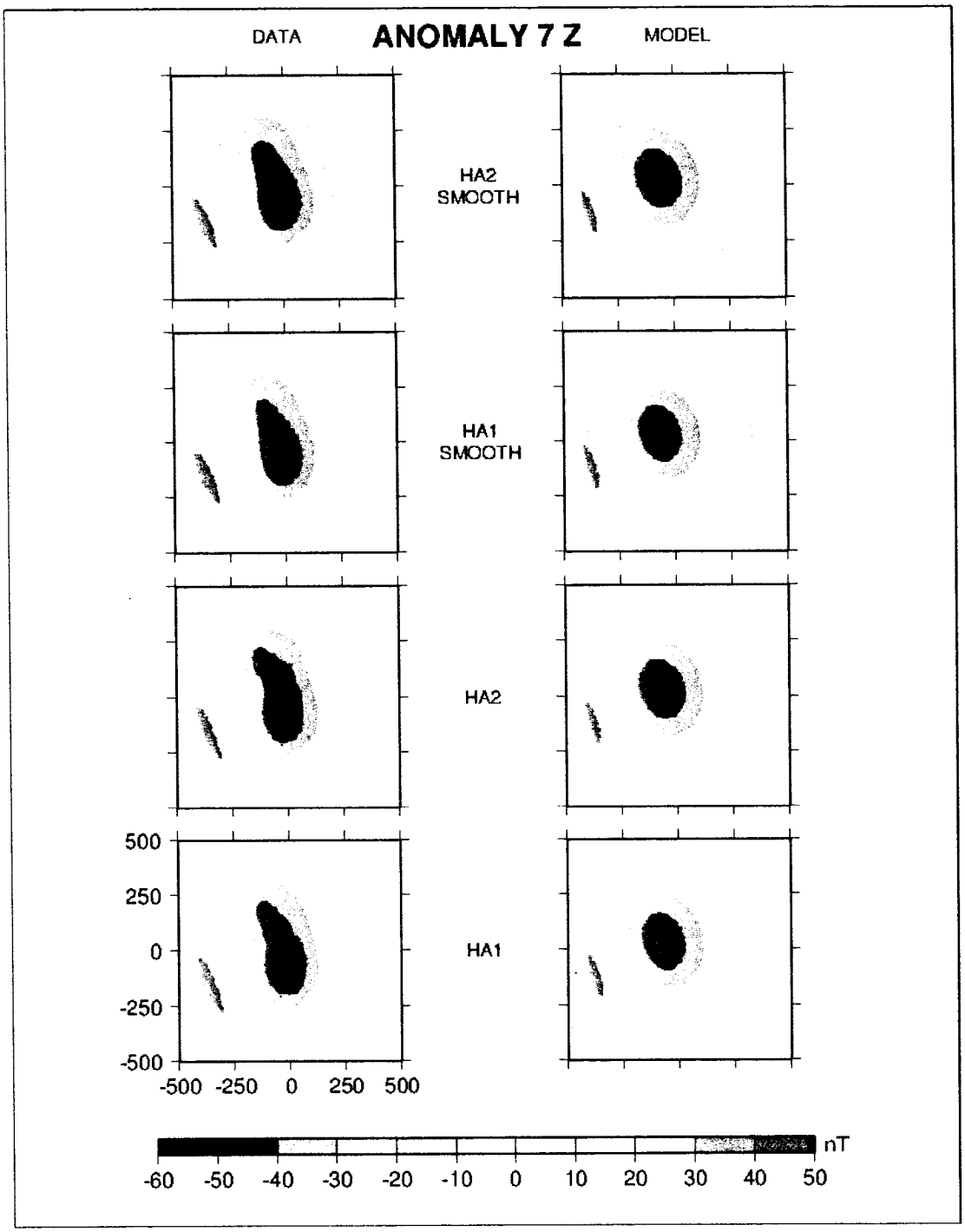
DATA
ANOMALY 7 Z
MODEL
HA2
SMOOTH
HA1
SMOOTH
HA2
HA1
500
250
0
-250
-500
-500 -250 0 250 500
nT
-60 -50 -40 -30 -20 -10 0 10 20 30 40 50

Figure 4.5

Figure 4.6

Scatter diagrams for the Z models of the A7 anomaly

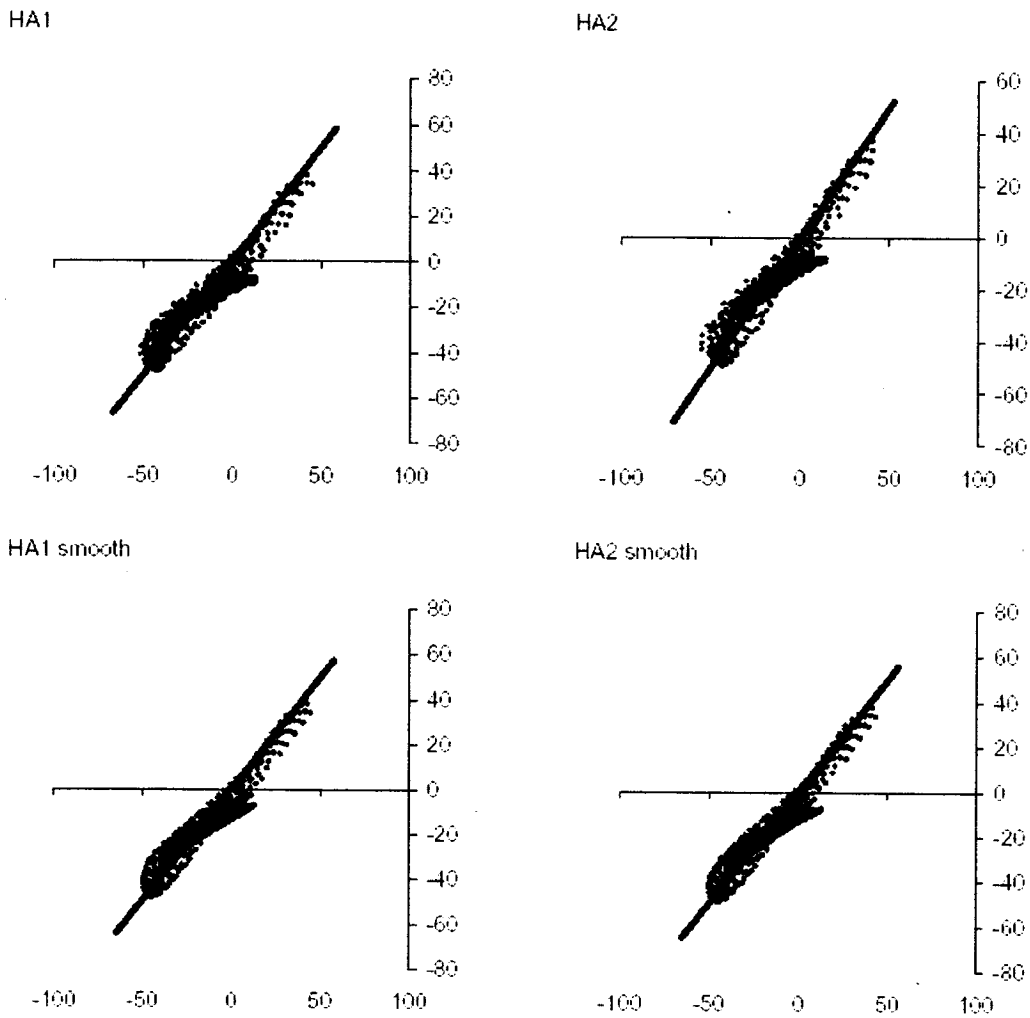
A7 Z models
HA1
HA2
HA1 smooth
HA2 smooth
80
60
40
20
0
-20
-40
-60
-80
-100
-50
0
50
100

Figure 4.6

Figure 4.7

Pole positions obtained by using all the high altitude radial models obtained in this study. Anomalies A1, A5 and A9 are represented by their south magnetic poles. The other anomalies are represented by their north magnetic poles.

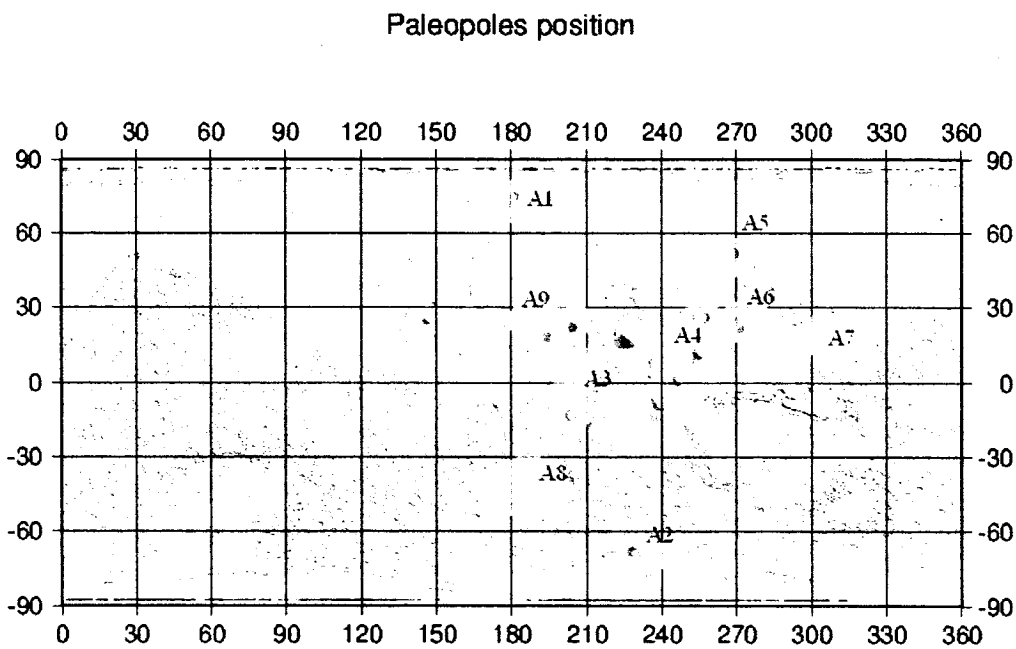
Paleopoles position
0 30 60 90 120 150 180 210 240 270 300 330 360
90 60 30 0 -30 -60 -90
A1
A5
A9
A6
A4
A7
A3
A8
A2

Figure 4.7

Figure 4.8

Combined radial component magnetic field of the two test prisms of table 4.3. The scale is chosen such as to represent minimum to maximum of each map.

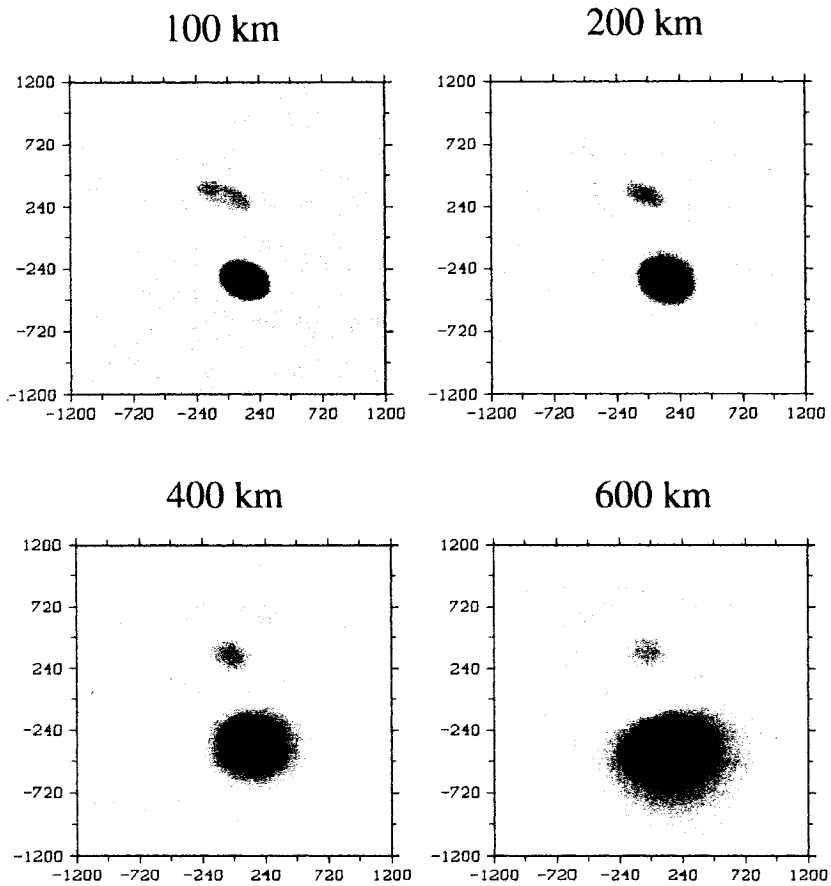
100 km
200 km
400 km
600 km
1200
720
240
-240
-720
-1200
-1200 -720 -240 240 720 1200

Figure 4.8

Figure 4.9

The 12 high altitude A5 pole positions obtained by using different prisms. In each panel squares represent phi models, Triangles represent theta models. Circle is the low altitude data model. Open symbols represent poles obtained by using a fix circular prism. Two colors symbols represent poles obtained by using a moving circular prism in the same way the elliptical prism used in this study was moved. Poles obtained by the fix circular prisms are much different than the rest.

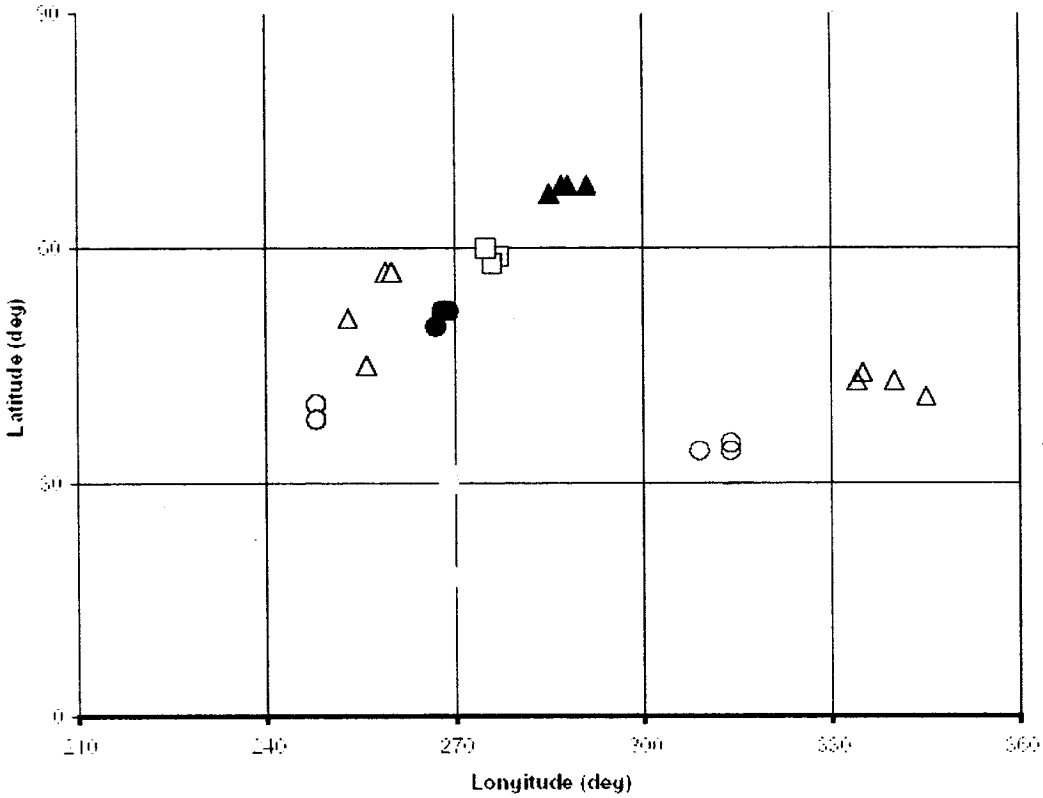

Figure 4.9

Chapter 5 : Conclusion and future research

5.1 Conclusion

This thesis has presented the theory of rotational dynamics of non-rigid planets and the result of modeling the observed magnetic field of Mars discovered during the current MGS mission. I have examined the quasi-fluid long-term estimation of polar motion for non-rigid planets based on the theory described by *Ricard et al.* [1993] and *Spada et al.* [1996]. The ultimate goal was to make a case for polar wandering on Mars based on the result of this modeling. In chapter 3 and 4 two different ways of modeling the MGS magnetic data were presented to infer the ancient core field dipole axis orientation and consequently the ancient rotation axis orientation.

The theory of long-term polar motion is described in chapter 1. It is a very complex subject that begs for a simplified approach. I found that the formulation of the theory exposed in *Ricard et al.* [1993], which seems to be the basis for the formulation of the rotational number of *Spada et al.* [1996], although technically correct is simply not necessary for a better comprehension of the use of the rotational number. I have shown in appendix B that the same result can be obtained from the linear polar motion equation in the Laplace domain. One positive point about this matrix formulation is that it is easier to implement in a computer program.

The rotational number itself is obtained only after an enormous simplification of the actual problem and can not be actually calculated because it depend so heavily on poorly known internal structure parameters. As with so many other things in geophysics, it is heavily model dependant. For example the estimation of the readjustment time of the equatorial bulge (T_1), a key parameter in the calculation of the rotational number, depend on the stratification model used and the various values of the Love numbers. However, having such a complex phenomenon, related to only one number is a critical step in the right direction, even though the estimation of that number is difficult. One must also remember that equations obtained in section 1.7 gives us only the starting point of the polar motion path. One must solved the full set of Euler-Liouville equation

with the full expression of the inertia tensor to get the complete polar motion path. One of the drawbacks of the derivation in appendix B, although simpler than the Ricard formulation to obtain the equations of section 1.7, is that we cannot solve for the full polar motion path.

This exploration of rotational dynamics makes it very likely that Mars experienced some polar wandering episode throughout its history. The presence of such important surface loads such as Tharsis and Mount Olympus and the Tharsis mountains indicates that early in history Mars was very geologically active. Some of these loads are still not compensated and must still contribute to this day to polar wandering on Mars.

That impression is still true after looking at the result of the magnetic anomalies modeling. If one looks at the modeling result on an anomaly per anomaly basis he will notice that the paleomagnetic pole positions obtained in the modeling of chapter 3 are different than those obtained in chapter 4. Most anomalies, indeed give different pole positions. This is unfortunate, but can be explained rather easily. First and foremost, two different methods were used. If our anomalies were clean and perfectly isolated this would not matter much, but this is not the case. In the case of chapter 3 both the low and high altitude data were used. The low altitude coverage is very scarce. Only a few tracks were used over each anomaly. All three components of the magnetic field were used. In the case of the study in chapter 4 only high altitude data were used. High altitude coverage is good but has poor resolution. Since outside and nearby sources affect anomalies in different and basically unpredictable ways it is next to impossible, as explained in chapter 2, to completely remove this contamination. Low and high altitude data is influenced in a different way. If the anomaly is not perfectly isolated, modeling each data set independently or combining them will result in different pole positions. Many investigators using different methods have obtained different results.

Given this, it is difficult to have complete confidence in any pole position for a given anomaly. The pole positions obtained can only be considered as preliminary. However the two modeling efforts made in this study have yielded some general results that are consistent with results obtained in other studies. First, absolutely none of pole positions found correspond with the

actual rotation axis of Mars. Assuming that our fundamental assumption is true then this is indicative that, indeed, Mars experienced some polar motion. This is truly consistent with other studies using different methods. However, to be on the pessimistic side of things, one cannot dismiss the possibility that the non-correlation between the actual rotation axis and the paleopole positions might be due to contamination. This issue must be resolved to have confidence in any result. Second, there seems to be a clustering of the poles in the Tharsis region. Although the clustering obtained in this study does not seem to be as tight as the one obtained in previous efforts it is still indicative of the role played by Tharsis in the polar motion history of Mars. Also found in this study, again consistent with other studies, is that poles of different signs are present in the cluster. This strongly argues for core field reversal on Mars, in much the same way the core field of the Earth has reversed.

In theory one good anomaly is sufficient to make a case for polar motion on Mars. In my case that anomaly would be A5 because it yield very close pole positions in the two studies. This, as mentioned earlier, is indicative of polar motion of at least 40 deg on Mars. Tharsis is probably responsible for that polar motion and the actual equatorial position of the structure does not seem to be a coincidence but rather the natural consequence of polar wandering.

5.2 Suggestions for future research

5.2.1 Rotational dynamics

The theory exposed by *Ricard et al.* [1993], and *Spada et al.* [1996] clearly shows the importance of the internal structure of rotating body in the amount and the type of polar motion that the body will experienced. The robustness of the interior structure models used in any estimation or prediction of polar motion is key to the confidence we can have in this estimation. I have verified in this study that, at least on the level of mathematics, the concept of rotational number seems to be correct. However, the concept is verified for some very simple (in a relative sense !!) situations like placing a point mass at the surface of the planet. It would be interesting to

see if the predictions of the type of polar motion still hold true for a more complex load or one that, geologically speaking, changes quickly with time.

The result obtained assumes that the load is very slow varying with respect to time and is small compare to the overall mass of the planet. While the latter point can be reasonably expected, the former is not as certain, especially in the case of Mars where things happened very quickly early in Martian history. To have more confidence in the theory it should be applied in a more general and more realistic situation despite the heavy mathematical price that would need to be paid to achieve a more general result.

5.2.2 Magnetic anomalies modeling

The results obtained in this thesis show clearly how any user of the MGS magnetic data is at the mercy of outside and nearby sources contamination. In this thesis I have removed outside contamination by using a Fourier domain technique in which two maps taken at a different time are compared in the frequency domain and any frequencies that do not correlate well are removed. Assuming that non correlating frequencies have been affected by time varying outside sources, then this method should work. However one must understand that those frequencies have not been created by the outside source, they have been only affected. So removing them from the data also removes some of the crustal magnetic field signal contained in those frequencies. We need to do that because we just do not know the exact proportion of crustal and non crustal signal in the frequencies we remove. The safest route is thus to remove them entirely.

It is really necessary to get a good idea of the portion of the crustal signal we remove by removing those non correlating frequencies. To do that it would be necessary to make a study of magnetic field versus time and try to identify trends if any. Such a study is possible with the actual high altitude data set, which spans many years of measurements. For example, one could divide the entire data set in 10 ,15 or more parts and do a correlation study between all those maps. This would give a much better idea of the situation than separating in two huge parts as I did in chapter 4. The goal of such a study would not be to get a general model of the

contamination, which would be very difficult at best, but to get a portrait of the external contamination just for the period during which data was obtained by MGS.

The problem of nearby sources contamination is even more difficult and fundamental in the use of magnetic anomalies for determining ancient pole positions. As mentioned earlier, this problem is fundamentally non unique. It is probably hopeless to think that we will ever get a robust and absolute portrait of the magnetization of the Martian surface. A more practical approach has to be used and we have to work with magnetization models obtained by different authors. There is a need for a high resolution magnetization model. For example *Langlais et al.* [2003] have proposed a magnetization model of the surface based on inverse dipole source modeling. *Philips* [2003] has also proposed one based on the Helbig method. *Arkani-Hamed* [2002] has proposed a magnetization model based on a 50 degree and order spherical harmonics expansion of the magnetic potential. It is very important to test the robustness of these magnetization models to identify which one fits the observed data best. This could be done simply by calculating the model field at a given altitude and compare with data. Or, maybe more interestingly, one could compare the calculated field from the many available spherical harmonics model available to the one produced by a magnetization model. Spherical harmonics models do not say anything about the magnetization of the surface but they can help validate magnetization models. Once a good magnetization model is identified it is then possible to calculate and remove the field created by nearby sources over any given anomaly. Therefore, identifying (or creating) a robust, high resolution, magnetization model of the Martian surface seems to be an important and necessary step to have confidence in the pole positions obtained in any paleomagnetic study. Also the resolution of the magnetization model needs to be increased. The resolution of *Langlais et al.* [2003] model is 173 km. This is much too coarse to detail the shape and size of the anomalies. See appendix C for a numerical experiment using that model.

There is also a strong need to constrain the depth and thickness of the source body. This has not been looked into during this study since paleomagnetic pole position is basically independent of those parameters . In particular the depth would constrains the magnetic layer thickness and give a crude evaluation of the temperature profile underneath the anomalies. If, for example, it was

demonstrated that the source bodies are close to the surface then the anomalies would most certainly be related to surface processes involving water. This could be the case for anomalies A5 and A6, which sits right over regions where liquid water was present in a distant past. The topography underneath those anomalies shows unmistakable signs of liquid water movement. For some other anomalies, like A1 and A2, which are situated on older, more cratered terrain, then one would expect that deep intrusives are more likely responsible for the observed magnetic field and therefore model elliptical prisms situated deeper below the surface would fit the data better. Modeling magnetic anomalies with prisms of varying depth and thickness would constitute a logical next step in this research.

Appendix A: Derivation of the polar motion equation

In this appendix I derive the long-term polar motion equation directly from the Euler-Liouville equation and the expression of the inertia tensor without using the Ricard formulation of equations 1.106 to 1.109. The Euler-Liouville equation is

$$\frac{d}{dt}([J]\bullet\vec{\omega})+\vec{\omega}\times([J]\bullet\vec{\omega})=0 \qquad \textbf{A.1}$$

where we have neglected relative motion of the mass elements inside the body and assume that external torque is 0. The matrix $[J]$ is the inertia tensor given by (see equation 1.105)

$$J_{ij}=I\delta_{ij}+\frac{k_f^T a^5}{3G}\left[\omega_i\omega_j-\frac{1}{3}\omega^2\delta_{ij}\right]-\frac{k_f^T a^5 T_l}{3G}\left[\dot{\omega}_i\omega_j+\omega_i\dot{\omega}_j-\frac{2}{3}\omega\dot{\omega}\delta_{ij}\right]+\left(1+k_f^L\right)\Delta I_{ij} \qquad \textbf{A.2}$$

I will use the following variables to simplify the algebra

$$U=\frac{k_f^T a^5}{3G} \quad , \quad E_{ij}=\left(1+k_f^L\right)\Delta I_{ij} \qquad \textbf{A.3}$$

So that the inertia tensor becomes

$$J_{ij}=I\delta_{ij}+U\left(\omega_i\omega_j-\frac{1}{3}\omega^2\delta_{ij}\right)-UT_l\left(\dot{\omega}_i\omega_j+\omega_i\dot{\omega}_j-\frac{2}{3}\omega\dot{\omega}\delta_{ij}\right)+E_{ij} \qquad \textbf{A.4}$$

with

$$I=\frac{1}{3}\sum_{i=1}^{3}I_{ii} \qquad \textbf{A.5}$$

A.1 The Euler-Liouville equation

Let's first consider the Euler-Liouville equation. The term $[J]\bullet\vec{\omega}$ can be simply expressed as

$$[J]\bullet\vec{\omega}=\begin{bmatrix}J_{11} & J_{12} & J_{13}\\ J_{21} & J_{22} & J_{23}\\ J_{31} & J_{32} & J_{33}\end{bmatrix}\begin{bmatrix}\omega_1\\ \omega_2\\ \omega_3\end{bmatrix}=\begin{bmatrix}J_{11}\omega_1+J_{12}\omega_2+J_{13}\omega_3\\ J_{21}\omega_1+J_{22}\omega_2+J_{23}\omega_3\\ J_{31}\omega_1+J_{32}\omega_2+J_{33}\omega_3\end{bmatrix}=\begin{bmatrix}\eta_1\\ \eta_2\\ \eta_3\end{bmatrix}=\vec{\eta} \qquad \textbf{A.6}$$

The vector $\vec{\eta}$ is then

$$\vec{\eta}=\hat{\varepsilon}_1\left(J_{11}\omega_1+J_{12}\omega_2+J_{13}\omega_3\right)+\hat{\varepsilon}_2\left(J_{21}\omega_1+J_{22}\omega_2+J_{23}\omega_3\right)+\hat{\varepsilon}_3\left(J_{31}\omega_1+J_{32}\omega_2+J_{33}\omega_3\right) \qquad \textbf{A.7}$$

where $\hat{\varepsilon}_1$, $\hat{\varepsilon}_2$ and $\hat{\varepsilon}_3$ are the unit vectors along the x_1, x_2 and x_3 axis respectively. In the Liouville equation the vector product $\vec{\omega}\times\left([J]\bullet\vec{\omega}\right)$ can then be written as

$$\vec{\omega}\times\left([J]\bullet\vec{\omega}\right)=\vec{\omega}\times\vec{\eta}=\begin{vmatrix}\hat{\varepsilon}_1 & \hat{\varepsilon}_2 & \hat{\varepsilon}_3\\ \omega_1 & \omega_2 & \omega_3\\ \eta_1 & \eta_2 & \eta_3\end{vmatrix}=\hat{\varepsilon}_1\begin{vmatrix}\omega_2 & \omega_3\\ \eta_2 & \eta_3\end{vmatrix}-\hat{\varepsilon}_2\begin{vmatrix}\omega_1 & \omega_3\\ \eta_1 & \eta_3\end{vmatrix}+\hat{\varepsilon}_3\begin{vmatrix}\omega_1 & \omega_2\\ \eta_1 & \eta_2\end{vmatrix} \qquad \textbf{A.8}$$

After a little more algebra we get

$$\vec{\omega}\times\left([J]\bullet\vec{\omega}\right)=\hat{\varepsilon}_1\left(\omega_2\eta_3-\eta_2\omega_3\right)+\hat{\varepsilon}_2\left(\eta_1\omega_3-\eta_3\omega_1\right)+\hat{\varepsilon}_3\left(\omega_1\eta_2-\eta_1\omega_2\right) \qquad \textbf{A.9}$$

The Euler-Liouville equation can now be written as

$$\dot{\eta}_1 + \omega_2\eta_3 - \eta_2\omega_3 = 0$$
$$\dot{\eta}_2 + \omega_3\eta_1 - \eta_3\omega_1 = 0 \qquad \textbf{A.10}$$
$$\dot{\eta}_3 + \omega_1\eta_2 - \eta_1\omega_2 = 0$$

Substituting the inertia tensor and taking the appropriate derivative in the last 3 expressions we get

$$\dot{J}_{11}\omega_1 + J_{11}\dot{\omega}_1 + \dot{J}_{12}\omega_2 + J_{12}\dot{\omega}_3 + \dot{J}_{13}\omega_3 + J_{13}\dot{\omega}_3 + \omega_2\left(J_{31}\omega_1 + J_{32}\omega_2 + J_{33}\omega_3\right)$$
$$-\omega_3\left(J_{21}\omega_1 + J_{22}\omega_2 + J_{23}\omega_3\right) = 0$$

$$\dot{J}_{21}\omega_1 + J_{21}\dot{\omega}_1 + \dot{J}_{22}\omega_2 + J_{22}\dot{\omega}_3 + \dot{J}_{23}\omega_3 + J_{23}\dot{\omega}_3 + \omega_3\left(J_{11}\omega_1 + J_{12}\omega_2 + J_{13}\omega_3\right) \qquad \textbf{A.11}$$
$$-\omega_1\left(J_{31}\omega_1 + J_{32}\omega_2 + J_{33}\omega_3\right) = 0$$

$$\dot{J}_{31}\omega_1 + J_{31}\dot{\omega}_1 + \dot{J}_{32}\omega_2 + J_{32}\dot{\omega}_3 + \dot{J}_{33}\omega_3 + J_{33}\dot{\omega}_3 + \omega_1\left(J_{21}\omega_1 + J_{22}\omega_2 + J_{23}\omega_3\right)$$
$$-\omega_2\left(J_{11}\omega_1 + J_{12}\omega_2 + J_{13}\omega_3\right) = 0$$

Now assuming that the angular velocity vector is initially aligned with the x_3 axis, that is $\vec{\omega} = (0,0,\omega_3)$ we can immediately simplify the last 3 equations and write

$$J_{11}\dot{\omega}_1 + J_{12}\dot{\omega}_3 + \dot{J}_{13}\omega_3 + J_{13}\dot{\omega}_3 - J_{23}\omega_3^2 = 0$$

$$J_{21}\dot{\omega}_1 + J_{22}\dot{\omega}_3 + \dot{J}_{23}\omega_3 + J_{23}\dot{\omega}_3 + J_{13}\omega_3^2 = 0 \qquad \textbf{A.12}$$

$$J_{31}\dot{\omega}_1 + J_{32}\dot{\omega}_3 + \dot{J}_{33}\omega_3 + J_{33}\dot{\omega}_3 = 0$$

A.2 Replacing the inertia tensor into the Liouville equation

Let's now consider each of the last 3 equations one by one and substitute the appropriate component of the inertia tensor. Again we assume $\vec{\omega} = (0,0,\omega_3)$ and that all second order derivatives and squares or product of derivatives are small enough to be neglected. Other reasonable assumptions will be made to simplify the mathematics. One must remember that our goal is to get a long-term approximate behavior of polar motion not a precise polar motion history of a given planet. The equations , as derived, basically only describe the situation at time t = 0. I will give a complete derivation of the first equation with all the necessary approximations and then quickly describe the result for the other two equations. Let's first consider the first equation in A.12. The inertia tensor components needed for this equation are

$$J_{11} = I + U\left(\omega_1^2 - \frac{1}{3}\omega^2\right) - UT_1\left(2\dot{\omega}_1\omega_1 - \frac{2}{3}\omega\dot{\omega}\right) + E_{11} \qquad \textbf{A.13}$$

Now taking into account that $\vec{\omega} = (0,0,\omega_3)$ so that $\omega = \omega_3$

$$J_{11} = I - U\frac{1}{3}\omega^2 + \frac{2}{3}\omega\dot{\omega}UT_1 + E_{11} = I - U\frac{1}{3}\omega_3^2 + \frac{2}{3}\omega_3\dot{\omega}_3UT_1 + E_{11} \qquad \textbf{A.14}$$

For the other components we find

$$\begin{aligned} J_{12} &= E_{12} \\ \dot{J}_{13} &= U\dot{\omega}_1\omega_3 + \dot{E}_{13} \\ J_{13} &= -UT_1\dot{\omega}_1\omega_3 + E_{13} \\ J_{23} &= -UT_1\dot{\omega}_2\omega_3 + E_{23} \end{aligned} \qquad \textbf{A.15}$$

Substituting all of this in the first Euler-Liouville equation we get

$$\left(I - U\frac{1}{3}\omega_3^2 + \frac{2}{3}\omega_3\dot{\omega}_3 UT_1 + E_{11}\right)\dot{\omega}_1 + E_{12}\dot{\omega}_3 + \left(U\dot{\omega}_1\omega_3 + \dot{E}_{13}\right)\omega_3 + \left(-UT_1\dot{\omega}_1\omega_3 + E_{13}\right)\dot{\omega}_3$$
$$-\left(-UT_1\dot{\omega}_2\omega_3 + E_{23}\right)\omega_3^2 = 0 \qquad \textbf{A.16}$$

According to our small squares and product of derivatives approximation we can write the last expression as

$$I\dot{\omega}_1 - \frac{1}{3}U\omega_3^2\dot{\omega}_1 + E_{11}\dot{\omega}_1 + E_{12}\dot{\omega}_2 + U\dot{\omega}_1\omega_3^2 + \dot{E}_{13}\omega_3 + E_{13}\dot{\omega}_3 + UT_1\omega_3^3\dot{\omega}_2 - E_{23}\omega_3^2 = 0 \qquad \textbf{A.17}$$

Now it is reasonable to assume that any inertia perturbation would be much smaller than the normalized inertia I . This would be equivalent as saying that the mass of the perturbation is much smaller than the mass of the entire planet. This is reasonable even in extreme cases like Tharsis, which has a very important mass but still much smaller than the mass of Mars. Consequently we can write

$$I\dot{\omega}_1 >> E_{11}\dot{\omega}_1 \ , \ E_{12}\dot{\omega}_2 \ , \ E_{13}\dot{\omega}_3 \qquad \textbf{A.18}$$

Of course if, as in the example given in section 1-7 the inertia perturbation is situated in the x_2x_3 plane than E_{11}, E_{12} and E_{13} are identically 0. So that the first Liouville equation becomes

$$I\dot{\omega}_1 + \frac{2}{3}U\omega_3^2\dot{\omega}_1 + \dot{E}_{13}\omega_3 + UT_1\omega_3^3\dot{\omega}_2 - E_{23}\omega_3^2 = 0 \qquad \textbf{A.19}$$

Now a case can be made for neglecting the second and third term of the last expression. In the case of the second term we usually have

$$\frac{2}{3}U\omega_3^2 << I \qquad \textbf{A.20}$$

This is especially true in the case of Venus where a difference in magnitude in the order of 10^7 is calculated by using reasonable values of the different parameters involved. In the case of the third term one can argue that the rate of change of the inertia perturbation will be very slow so that the derivative with respect to time of the inertia perturbation will be very small so that $\dot{E}_{13} \approx 0$. With these supplementary approximations we finally get for the first Euler-Liouville equation

$$I\dot{\omega}_1 + UT_1\omega_3^3\dot{\omega}_2 - E_{23}\omega_3^2 = 0 \qquad \textbf{A.21}$$

Now to get the first polar motion equation of section 1-7 that was obtained using the Ricard formulation we use $UT_1 = (C-A)T_1\omega_3$, so that

$$I\dot{\omega}_1 + (C-A)T_1\omega_3\dot{\omega}_2 - E_{23}\omega_3^2 = 0 \qquad \textbf{A.22}$$

By using a similar derivation as above and the same approximations and simplifications we can work out the second equation in A.12 as

$$J_{21}\dot{\omega}_1 + J_{22}\dot{\omega}_3 + \dot{J}_{23}\omega_3 + J_{23}\dot{\omega}_3 + J_{13}\omega_3^2 = 0 \qquad \textbf{A.23}$$

with

$$\begin{aligned} J_{21} &= E_{12} \\ J_{22} &= I - \frac{1}{3}U\omega_3^2 + \frac{2}{3}UT_1\omega_3\dot{\omega}_3 + E_{22} \\ \dot{J}_{23} &= U\dot{\omega}_2\omega_3 + \dot{E}_{23} \\ J_{23} &= -UT_1\dot{\omega}_2\omega_3 + E_{23} \\ J_{13} &= -UT_1\dot{\omega}_1\omega_3 + E_{13} \end{aligned} \qquad \textbf{A.24}$$

Substituting the above values in the second Euler-Liouville equation we get the following expression after all the simplifications and approximations have been applied

$$I\dot{\omega}_2 - (C-A)T_1\omega_3\dot{\omega}_1 + E_{13}\omega_3^2 = 0 \qquad \textbf{A.25}$$

For the third equation in A.12 we have in the same manner

$$J_{31}\dot{\omega}_1 + J_{32}\dot{\omega}_3 + \dot{J}_{33}\omega_3 + J_{33}\dot{\omega}_3 = 0 \qquad \textbf{A.26}$$

with

$$\begin{aligned} J_{31} &= -UT_1\dot{\omega}_1\omega_3 + E_{31} \\ J_{32} &= -UT_1\dot{\omega}_2\omega_3 + E_{32} \\ \dot{J}_{33} &= \frac{4}{3}U\omega_3\dot{\omega}_3 + \dot{E}_{33} \\ J_{33} &= I + \frac{2}{3}U\omega_3^2 - \frac{4}{3}UT_1 + E_{33} \end{aligned} \qquad \textbf{A.27}$$

Substituting in the third Euler-Liouville equation and applying again the different approximations and simplifications we get simply

$$I\dot{\omega}_3 + \dot{E}_{33}\omega_3 = 0 \qquad \textbf{A.28}$$

A.3 Conclusion

We have now derived the three equations of motion that will ultimately lead us to the polar motion equation, they are

$$I\dot{\omega}_1 + (C-A)T_1\omega_3\dot{\omega}_2 - E_{23}\omega_3^2 = 0$$

$$I\dot{\omega}_2 - (C-A)T_1\omega_3\dot{\omega}_1 + E_{13}\omega_3^2 = 0 \qquad \textbf{A.29}$$

$$I\dot{\omega}_3 + \dot{E}_{33}\omega_3 = 0$$

This derivation shows that the matrix formalism of *Ricard et al.*, [1993] is correct and can be used to derive the equation of motion. If one puts $\vec{\omega} = (0,0,\Omega)$ in equation 1.112 the result in A.29 will appear. A.29 is the equation actually used to derive equation 1.113 in section 1.6. As stated earlier this formalism is not absolutely necessary to get the polar motion equation of section 1.7.

Appendix B : More on long term polar motion

B.1 Evaluation of the equatorial bulge realignment time

The time needed for the equatorial bulge to realign perpendicularly to the axis of rotation is an important parameter of polar motion of non-rigid planet. I feel it is necessary to explain clearly where this parameter comes from. Recall that the linear form of the polar motion equation in the time domain is given by

$$i\frac{\dot{m}(t)}{\sigma_r} + m(t)\left[1 - \frac{k^T(t)}{k_o}\right] = \Psi^L(t) \qquad \textbf{B.1}$$

Now let's go back into the Laplace domain where we will be able to use the different expressions for the tidal Love number . In the Laplace domain the last equation becomes

$$\left(i\frac{s}{\sigma_r} + \left[1 - \frac{k^T(s)}{k_o}\right]\right)m(s) = \Psi^L(s) \qquad \textbf{B.2}$$

where the Laplace transform of the product of functions $k^T(t) \times m(t)$ has been approximated by the product of their respective Laplace transform. The tidal Love number can be expressed as

$$k(s) = k_e + \sum_{i=1}^{M}\frac{k_i}{s - s_i} \qquad \textbf{B.3}$$

We have seen that for the long-term limit that the last Love number can be expressed as

$$k_f = k_e - \sum_{i=1}^{M}\frac{k_i}{s_i} \qquad \textbf{B.4}$$

Now if we consider the situation where $s << s_i$ one can expand the k(s) expression in Taylor series and get after a simple transformation

$$k(s) = k_e - \sum_{i=1}^{M} \frac{k_i}{s_i} \frac{1}{\left(1 - \frac{s}{s_i}\right)} = k_e - \sum_{i=1}^{M} \frac{k_i}{s_i} \left(1 + \frac{s}{s_i} + \left(\frac{s}{s_i}\right)^2 + \left(\frac{s}{s_i}\right)^2 + ...\right) \qquad \textbf{B.5}$$

If we neglect terms of higher order to keep our calculation in line with a linear approximation, we get

$$k(s) = k_e - \sum_{i=1}^{M} \frac{k_i}{s_i} \left(1 + \frac{s}{s_i}\right) = k_e - \sum_{i=1}^{M} \frac{k_i}{s_i} - s \sum_{i=1}^{M} \frac{k_i}{s_i^2} \qquad \textbf{B.6}$$

By using equation B.4 we can express k(s) as

$$k(s) = k_f - s \sum_{i=1}^{M} \frac{k_i}{s_i^2} \qquad \textbf{B.7}$$

With this information and again approximating the secular Love number by the fluid Love number we get

$$\left(i\frac{s}{\sigma_r} + \left[1 - \frac{k_f - s \sum_{i=1}^{M} \frac{k_i}{s_i^2}}{k_f} \right] \right) m(s) = \Psi^L(s) \qquad \textbf{B.8}$$

which becomes after simplification

$$\left(i\frac{s}{\sigma_r} + \frac{s}{k_f} \sum_{i=1}^{M} \frac{k_i}{s_i^2} \right) m(s) = \Psi^L(s) \qquad \textbf{B.9}$$

Now isolating the polar motion function m(s) we get after a few algebraic transformations

$$m(s) = -i\sigma_r \frac{\Psi^L(s)}{s\left(1 - i\sigma_r \frac{1}{k_f}\sum_{i=1}^{M}\frac{k_i}{s_i^2}\right)} \qquad \textbf{B.10}$$

We now define the readjustment time T_1 of the equatorial bulge as

$$T_1 = \frac{1}{k_f}\sum_{i=1}^{M}\frac{k_i}{s_i^2} \qquad \textbf{B.11}$$

This important parameter depend on the different relaxation times $\tau_i = -\frac{1}{s_i}$ which in turn depend on viscosity and rigidity, so the visco-elastic parameters of the planetary interiors play a crucial role in the evaluation of the time parameter and consequently on polar wander itself. The equation for linear polar motion B.10 thus become

$$m(s) = -i\sigma_r \frac{\Psi^L(s)}{s(1 - i\sigma_r T_1)} \qquad \textbf{B.12}$$

B.2 Long term interpretation of the rotational number from the linear Euler-Liouville equation

One can obtain the polar motion equation of section 1.6 that will ultimately lead to the interpretation of the rotational number of section 1.7 by using the last expression. We can write

$$m(s) = \left[\frac{-i\sigma_r}{s(1 - i\sigma_r T_1)}\right]\Psi^L(s) \qquad \textbf{B.13}$$

Now let's try to express the constant term in brackets in the more traditional complex form $A + iB$. We have

$$\left[\frac{-i\sigma_r}{s(1-i\sigma_r T_l)}\right]=\frac{-i\sigma_r}{s(1-i\sigma_r T_l)}\times\frac{1+i\sigma_r T_l}{1+i\sigma_r T}=\frac{-i\sigma_r+\sigma_r^2 T_l}{s(1+\sigma_r^2 T_l^2)} \qquad \textbf{B.14}$$

This last expression can be written as

$$\frac{-i\sigma_r+\sigma_r^2 T_l}{s(1+\sigma_r^2 T_l^2)}=\frac{1}{s}\left[\frac{\sigma_r^2 T}{(1+\sigma_r^2 T_l^2)}-i\frac{\sigma_r}{(1+\sigma_r^2 T_l^2)}\right] \qquad \textbf{B.15}$$

Transferring this in the polar motion equation in the Laplace domain and multiplying on each side by the Laplace variable s, we get

$$\left[\frac{\sigma_r^2 T_l}{(1+\sigma_r^2 T_l^2)}-i\frac{\sigma_r}{(1+\sigma_r^2 T_l^2)}\right]\Psi^L(s)=sm(s) \qquad \textbf{B.16}$$

Now let's consider again the rotational number R_o (equation 1.116) we have seen that

$$R_0=\Omega\frac{T_l(C-A)}{I} \qquad \textbf{B.17}$$

And from equation 1.37 we have

$$\sigma_r=\left[\frac{C-A}{A}\right]\Omega \qquad \textbf{B.18}$$

Simple algebra yield the following relationship between R_o and σ_r

$$R_o=\frac{T_l\sigma_r A}{I} \qquad \textbf{B.19}$$

If one assume a very small difference between A and I, such that $I \approx A$, we can finally write

$$R_o = T_l \sigma_r \rightarrow \frac{R_o}{T_l} = \sigma_r \qquad \textbf{B.20}$$

So that the ratio of the rotational number over the readjustment time of the equatorial bulge is equal to $2\pi/T_{chan}$ where T_{chan} is the Chandler wobble period for a rigid planet. Now let's take the relation $R_o = T_l \sigma$ into the polar motion equation B.16. We have

$$\left[\frac{R_o \sigma_r}{(1+R_o^2)} - i\frac{\sigma_r}{(1+R_o^2)}\right]\Psi^L(s) = sm(s) \qquad \textbf{B.21}$$

Now let's multiply each side by R_o and divide by σ_r to find

$$\left[\frac{R_o^2}{(1+R_o^2)} - i\frac{R_o}{(1+R_o^2)}\right]\Psi^L(s) = \frac{R_o}{\sigma_r} sm(s) \qquad \textbf{B.22}$$

Note that the term in brackets is identical to the one in the polar motion equation 1.118 in section 1.6.1. Now using equation B.20 and going back into the space domain we get

$$\left[\frac{R_o^2}{(1+R_o^2)} - i\frac{R_o}{(1+R_o^2)}\right]\Psi^L(t) = T_l \dot{m}(t) \qquad \textbf{B.23}$$

We have $\omega = m\Omega$ so that $\dot{m} = \dot{\omega}/\Omega$ and

$$\begin{aligned} \dot{\omega}(t) &= \left[\frac{R_o^2}{(1+R_o^2)} - i\frac{R_o}{(1+R_o^2)}\right]\frac{\Omega}{T_l}\Psi^L(t) \\ \omega(t) &= \left[\frac{R_o^2}{(1+R_o^2)} - i\frac{R_o}{(1+R_o^2)}\right]\frac{\Omega}{T_l}\int_0^t \Psi^L(t)dt \end{aligned} \qquad \textbf{B.24}$$

One must now consider the excitation function $\Psi^L(t)$. We have given the expression of this function in section 1.3. It is

$$\Psi(t)=\frac{1}{\Omega^2[C-A]}\left[\Omega^2\Delta I(t)-i\Delta\dot{I}(t)+\Omega h(t)-i\dot{h}(t)+iL(t)\right] \qquad \textbf{B.25}$$

Now let's make the same simplifications and approximations made in appendix A. This will reduce equation B.25 to

$$\Psi(t)=\frac{\Delta I(t)}{[C-A]} \qquad \textbf{B.26}$$

To take load compensation into account one must multiply this last expression by the term $1+k_f^L$. We can now replace in the polar motion equation to get

$$\omega(t)=\left[\frac{R_o^2}{\left(1+R_o^2\right)}-i\frac{R_o}{\left(1+R_o^2\right)}\right]\frac{\Omega\left(1+k_f^L\right)}{T_i(C-A)}\int_0^t\Delta I(t)dt \qquad \textbf{B.27}$$

This formula is identical to the polar motion equation 1.119 in section 1.6.1 and would therefore lead to the very same conclusion when extreme limits of R_o are investigated.

Appendix C : Supplementary comments on anomaly isolation

In chapter 4 I presented results of modeling 9 magnetic anomalies. The robustness of the pole position found for each anomaly, that is how much confidence we can have in the result, is greatly dependant on how well isolated a given anomaly is. In chapter 4, based on the value of the quality index, it was argued that anomalies A4 and A5 are well isolated and that anomalies A6 and A7 are not well isolated. If the pole position found is to mean anything the source body must be well isolated and uniformly magnetized. As mentioned earlier, there is just no such thing as a perfectly isolated anomaly.

First, one must have a clear understanding of what an isolated anomaly is, in the practical world where the modeled data is actually the vector sum of the magnetic field produced by many sources. In a simple situation one could define an isolated anomaly as an anomaly where the distance between the anomaly and other sources is much bigger than the size of the anomaly. What actually « much bigger » means is somewhat subjective. A minimum value for the distance of 5 to 6 times the diameter of the anomaly seems to be indicated by numerical experiments that I performed during this study. It has also been mentioned in chapter 4 that another criteria to determine if an anomaly is isolated is that such an anomaly yields the same pole position no matter the altitude of the data used for modeling. This last assertion has been verified many times in this study on synthetic data. The MGS data, unfortunately, has global coverage at high altitude only and it is then difficult to verify the assertion on actual data.

However on Mars no anomaly of interest have this ideal characteristic. How do we explain then that some anomalies like A5 have such high value of the quality index and therefore that the model fit the data so well? This is especially perplexing since a quick look at the global map of the radial component of the high altitude magnetic field (see figure 2.2) clearly shows that the A5 anomaly (located at lat = -1 and long = 322) does not correspond to the ideal criteria of distance

mentioned above and is part of a busy neighborhood where magnetic sources are interacting strongly.

However one can look at anomaly isolation from another angle. If an anomaly is dominant in a given neighborhood or if by some luck the interaction of the other source bodies close to the anomaly is such that their influence cancel or is very weak compared to the anomaly itself then we basically have an isolated anomaly. In this appendix I want to make the case that this is exactly the situation for anomaly A5. I will also show that anomaly A7 is not well isolated because the influence of the nearby sources does not cancel.

To show this at the present time we need global data coverage at different altitudes. This is just not possible at this time. Instead, we must rely on models to obtain global coverage at an altitude different than 400 km. Preferably, we need a magnetization model of the surface that will give us the opportunity, not only to calculate the magnetic field at any altitudes, but also to remove sources at a given location to see the influence of the neighboring sources. One model of interest is the one obtained by *Langlais et al.,* [2003] who have modeled the magnetic field of Mars by using magnetic dipoles. This model has been mentioned numerous times in this thesis. Their best fit model uses 4840 dipoles with an average separation of 173 km and, consistent with other studies, they have used a magnetic layer thickness of 40 km. The dipoles themselves are at 20 km depth. Benoit Langlais, of Nasa's Goddard Space Flight Center, has graciously provided me with his magnetization map. With this information it is then relatively easy to calculate the 3 components of the magnetic field of the model at any altitudes higher than 173 km, which is the resolution limit of the model. Details on the method to calculate the magnetic field are provided in *Dyment and Arkani-Hamed* [1998].

Of course, this is only a model of the magnetic field. I assume that the model represent well the magnetic field at any altitude higher than 173 km. I have used this model to calculate the magnetic field at 400 km altitude. The result is shown in figure C.1. Compare this figure with figure 2.2. Both figures used the same color scale. The model represent well long wavelength features but seems to have some difficulties in the mid to small wavelength characteristics of the

field, especially for the theta and phi components. This is probably indicative of higher contamination in the horizontal components. However the radial component of the model compare well with the data of figure 2.2 so that only the radial component will be used in the following argument.

To illustrate my point I have generated synthetic data for anomaly A5 and A7 for 3 different altitudes : 200, 300 and 400 km. According to the argument made in chapter 4 a well isolated anomaly will give the same pole position irrespective of the altitude of the data. For each anomaly I have obtained , by using the very same least square fitting technique used in chapter 4, the pole position for each altitude. The results are given in table C.1 below. One can see that for anomaly A5 the changes in the pole position are small with altitude variation and that the elliptical prism obtained for each altitude have identical characteristics. This consistency in the results is indicative of a well-isolated anomaly. In the case of A7 results in both the pole position and the characteristics of the elliptical prism show much greater dependence on altitude and A7 is therefore considered not well isolated. In both cases the pole position obtained at 400 km altitude is consistent with the one obtained in chapter 4.

To show why anomaly A5 is well isolated and anomaly A7 is not, I have removed them from the global magnetization map and recalculated the total magnetic field over the area occupied by each anomaly. In the case of A5 I have removed all dipoles within a 6 deg radius of the center of the anomaly. In the case of A7 I have removed all dipoles within 7 deg from the center of the anomaly. For each anomaly the same filter value was used at all altitudes. These values are the filter radii used in the modeling program. Only the data inside that radius was used for the modeling. It is assumed that the actual source body is situated within that radius of the center of the anomaly. The result of this little experiment are displayed in figure C.2 and C.3.

In each figure, for each altitude, the left hand figure is the total radial component of the field at the given altitude. The right hand figure is the total field with the above-mentioned dipoles removed. One can see very clearly that in the case of A5 the anomaly practically disappear over the center of the anomaly at lat = -1 and long = 322. This is especially true at 300 and 400 km

altitude. In the case of A7 however (figure C.3) we have a quite different situation. At 200 km altitude, despite the fact that all dipole sources have been removed in a radius of 7 deg (appreciatively 420 km) from the center at lat = -45 and long = 225 the shape of the anomaly is still present. This is indicative that the anomaly is strongly influence by nearby sources and the shape itself of the anomaly is changed by nearby sources. This anomaly, might not even have been created by an independent source and is more likely the result of the combined effect of many sources outside the 7 deg radius where dipoles have been removed, basically a ghost anomaly. This figure also shows that at 300 km altitude there is still a significant presence of nearby contamination. In the end, I feel that the pole position obtained with this anomaly, simply cannot be trusted.

Since it is unlikely that we will get global data coverage at different altitudes in the near future we need magnetization models of the surface to better constraint the influence of one anomaly over the other. The model used in this little experiment is too coarse to make good judgments on influence of anomalies over each other. An improvement of the resolution of the model, actually at 173 km would be welcome. Resolutions in the 15 to 30 km range are needed to better constraint the shape, size and position of each source bodies responsible for the observed anomalies.

Table C.1

Pole positions obtained by modeling data generated by the Langlais et Al, 2003 surface magnetization model. The data was generated for anomalies A5 and A7 of chapter 4 at altitude of 200, 300 and 400 km. The fact that the A5 anomalies give consistent result from one altitude to the other indicates that the anomaly is well isolated. This is not the case for A7.

A5

Altitude (km)	A (km)	B (km)	θ (deg)	Pole lat (deg)	Pole long (deg)
200	300	210	60	63	267
300	300	210	60	53	270
400	300	210	60	51	268

A7

Altitude (km)	A (km)	B (km)	θ (deg)	Pole lat (deg)	Pole long (deg)
200	300	150	100	-32	134
300	220	110	100	-26	132
400	100	50	100	-33	119

A : semi-major axis of elliptical prism

B : semi-minor axis of elliptical prism

θ : Orientation of prism (counterclokwise from east oriented x axis)

Pole lat and long : paleopole latitude and logitude

Table C.1

Figure C.1

Global magnetic field at 400 km altitude generated by the *Langlais et al.,* [2003] magnetization model. Compare this figure to figure 2.2, which represent the binned high altitude data used to model the actual magnetic field. The model is more successful in representing the radial component of the actual field.

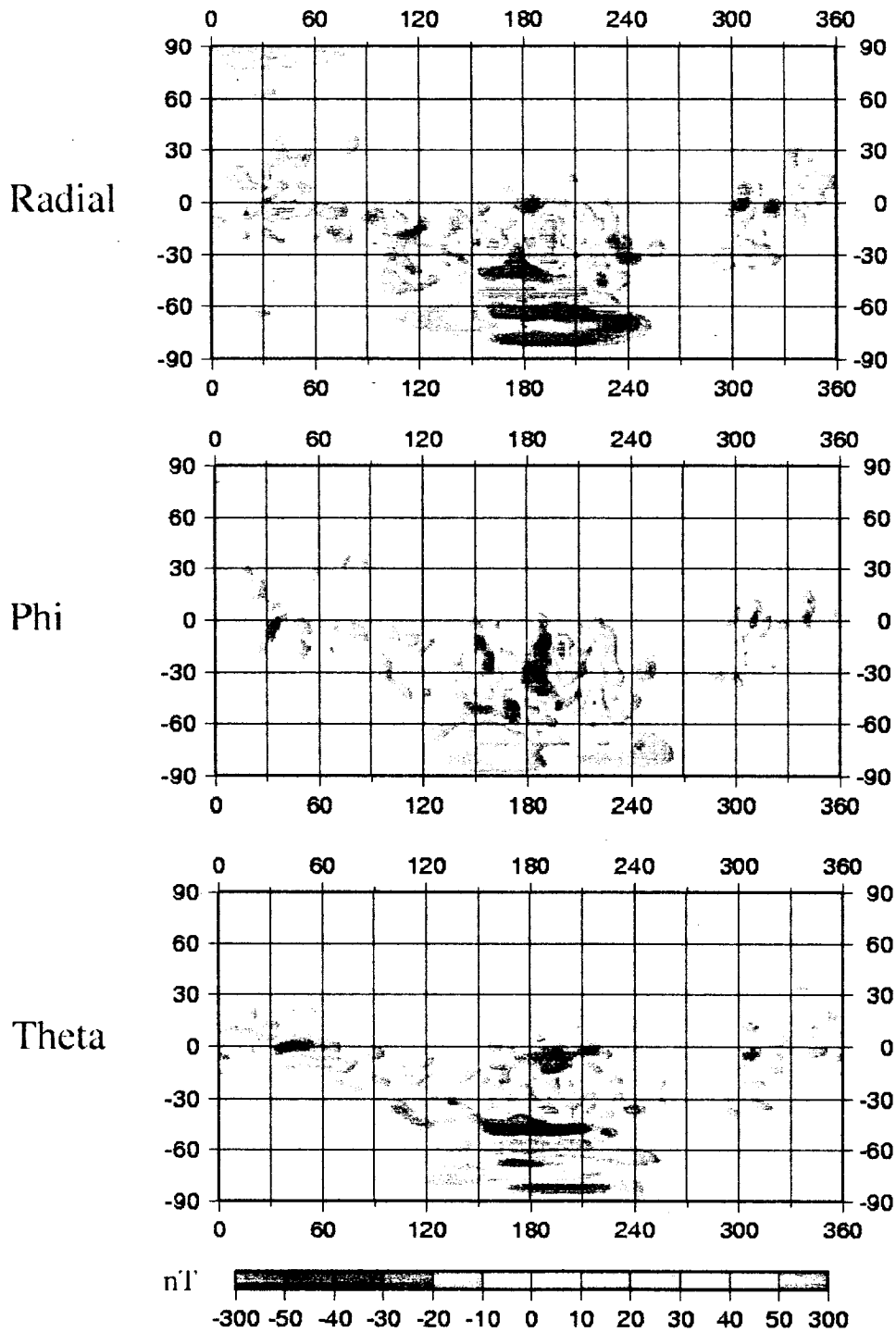
Radial
Phi
Theta
0 60 120 180 240 300 360
90 60 30 0 -30 -60 -90
nT
-300 -50 -40 -30 -20 -10 0 10 20 30 40 50 300

Figure C.1

Figure C.2

The A5 anomaly according to the *Langlais et al.*, [2003] model. The left hand panel for each altitude is the total radial component of magnetic field over anomaly A5. The right hand panel is the radial component over the same area but with dipoles within 6 deg of the center of the anomaly removed. The fact that the anomaly disappears indicates that contamination by nearby sources is weak and that A5 is well isolated.

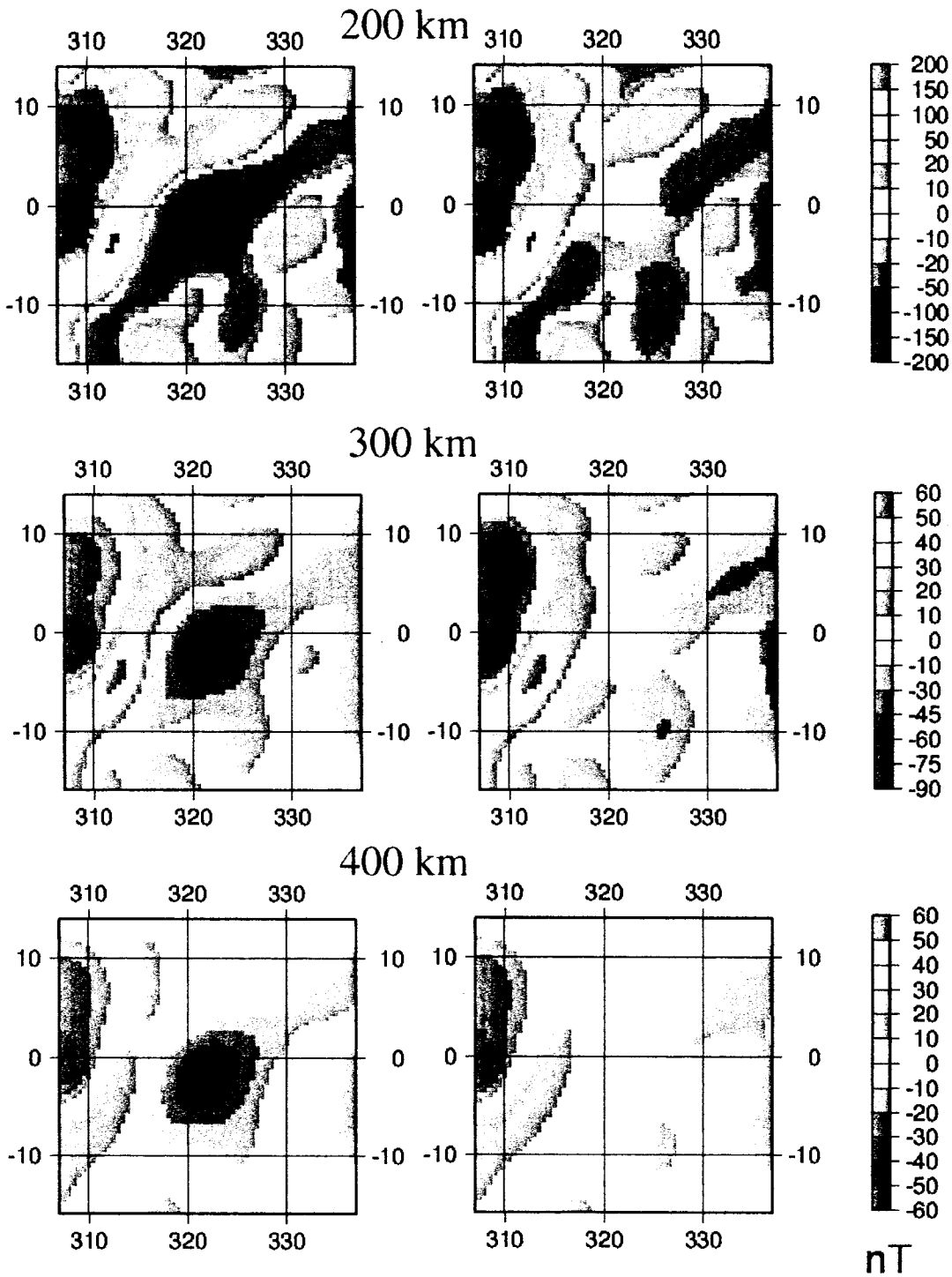
200 km
300 km
400 km
310
320
330
10
0
-10
200
150
100
50
20
10
0
-10
-20
-50
-100
-150
-200
60
50
40
30
20
10
0
-10
-30
-45
-60
-75
-90
60
50
40
30
20
10
0
-10
-20
-30
-40
-50
-60
nT

Figure C.2

Figure C.3

Figure similar to figure C.2 but for anomaly A7. Dipoles within a radius of 7 deg were removed to calculate the radial component of the field in the right column. Clearly at 200 km altitude the anomaly is still very present, indicating that most of the anomaly comes from nearby sources. A7 is not well isolated and may not even be created by an independent body but simply be the vector sum of the magnetic field created by nearby sources.

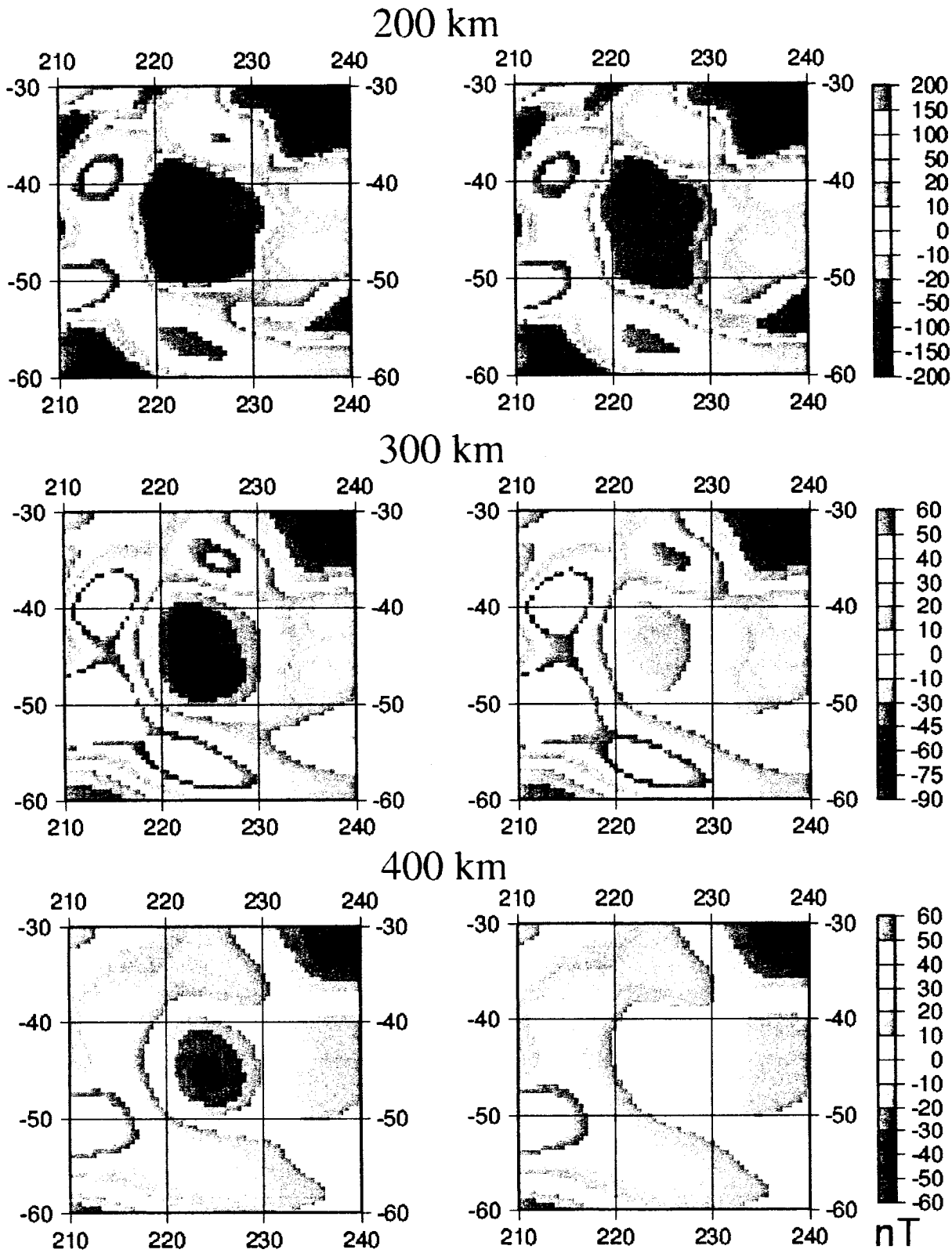
200 km
300 km
400 km
210
220
230
240
-30
-40
-50
-60
200
150
100
50
20
10
0
-10
-20
-50
-100
-150
-200
60
50
40
30
20
10
0
-10
-30
-45
-60
-75
-90
nT

Figure C.3

Appendix D : Magnetic anomalies and topography

This appendix presents nine high-resolution topographic maps of the regions where the anomalies modeled in this study are. Each map is overlaid with the radial component of the binned magnetic field over each region. On each map, the anomaly is at the center (or very close to) of the map. All maps use the same color scale for easier comparison. The maps show no clear correlation between the anomalies and topographical features. This was to be expected since my modeling found sources bodies (elliptical prisms) that have semi-major axis in the 200 to 300 km range. There is simply no major topographical feature of that dimension in the regions where the anomalies are. In some cases however (A5 and A6 anomalies) the anomaly can possibly be related to surface processes involving water. In the case of A6 for example, the anomaly is at the receiving end of what seems to be a dry riverbed. Magnetic minerals may have been deposited there and formed the anomaly.

In most cases this lack of correlation probably indicates that the sources are deeper into the crust. However, how deep exactly, remains to be seen. That depth does not need to be extreme. Most investigators favor an average magnetic thickness of 40 to 50 km. *Langlais et al.*, [2003] magnetization model place their best fit dipoles at a 20 km depth which seems to indicate that the crust is not magnetized all the way to the surface for many source bodies.

A1 radial component

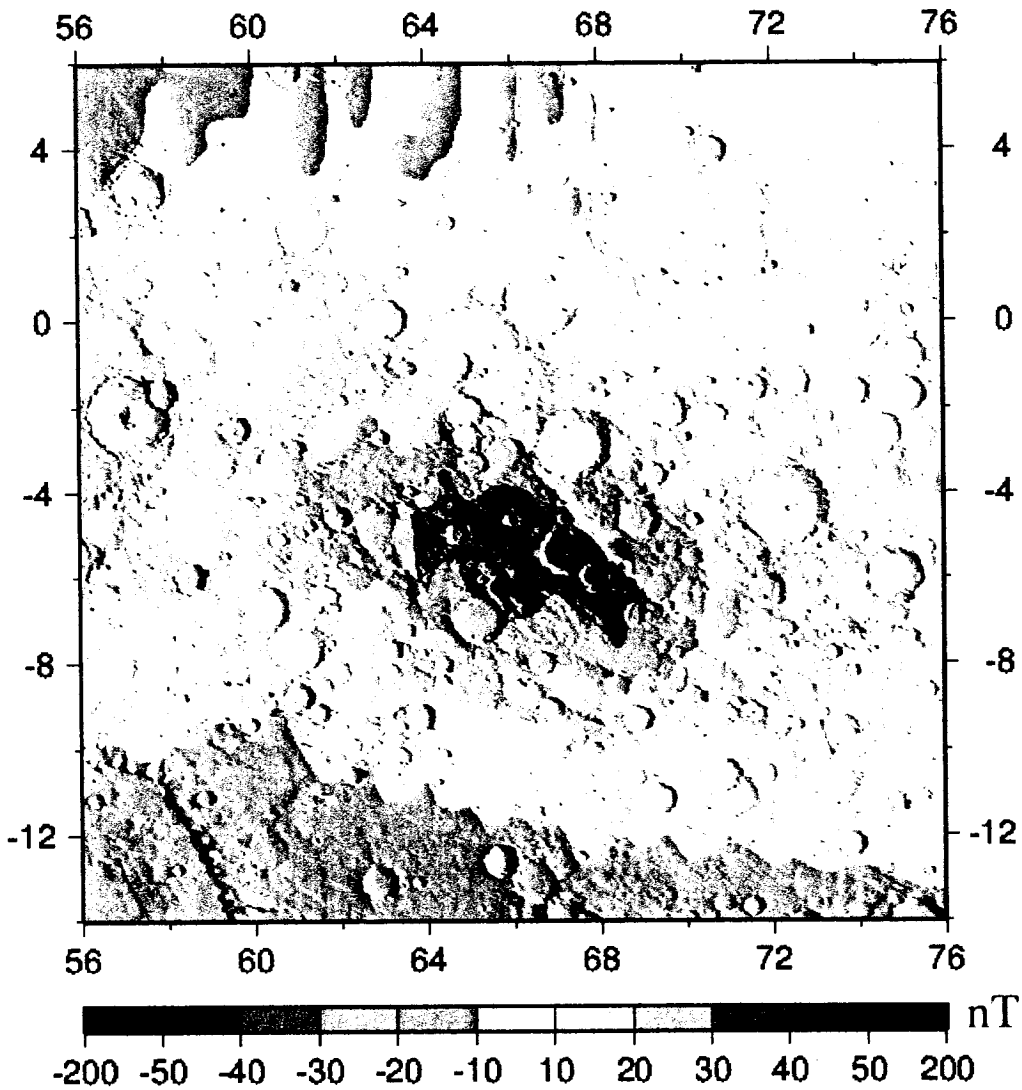

A2 radial component

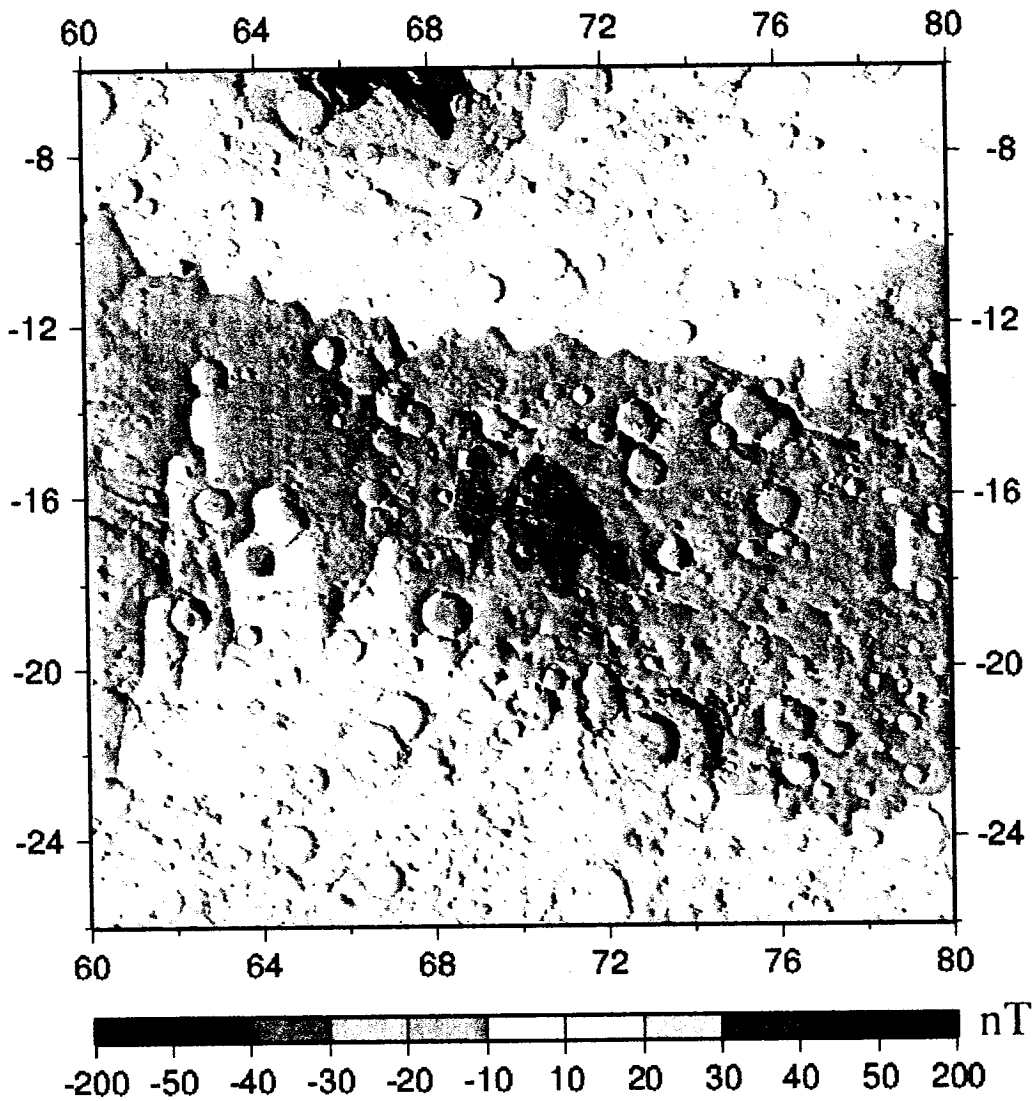

A3 radial component

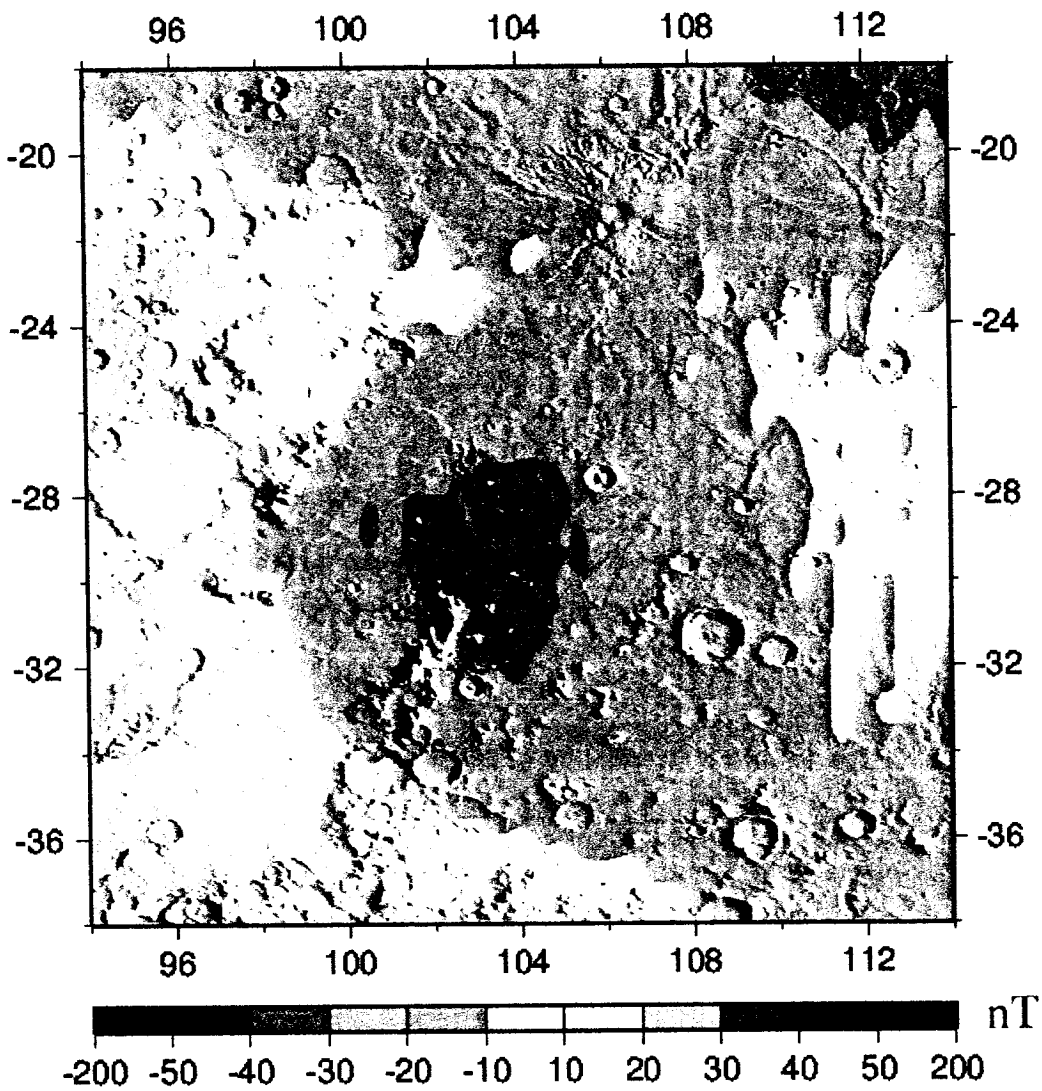

A4 radial component

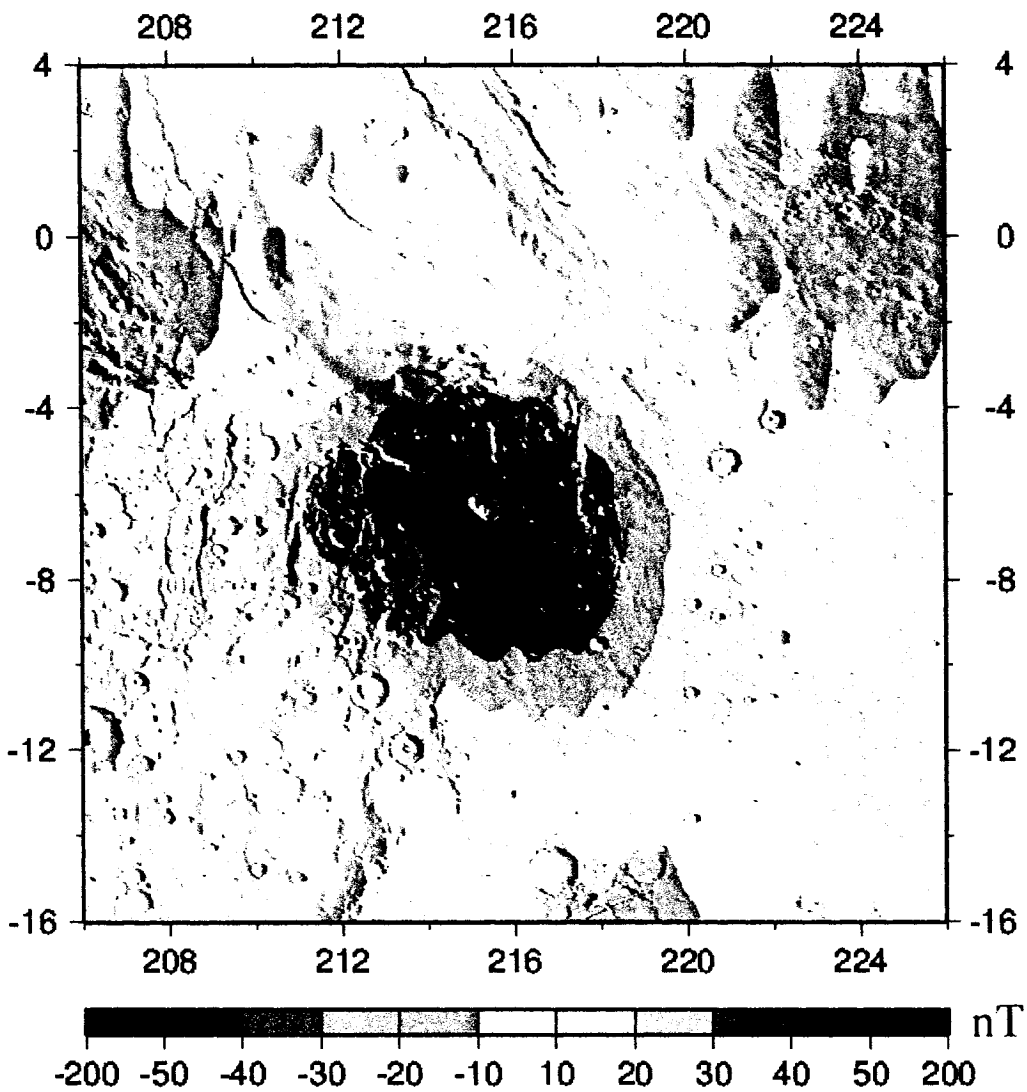

A5 radial component

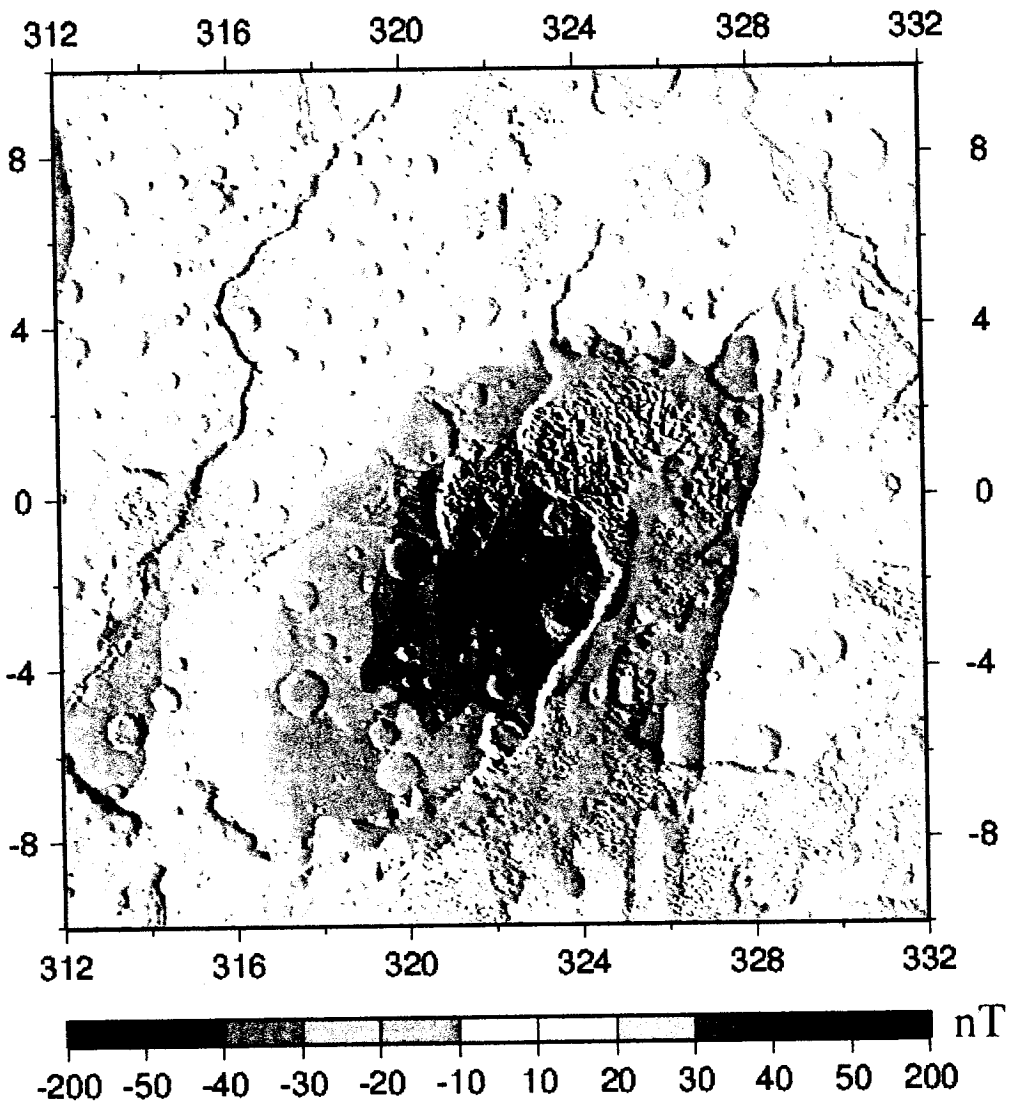

A6 radial component

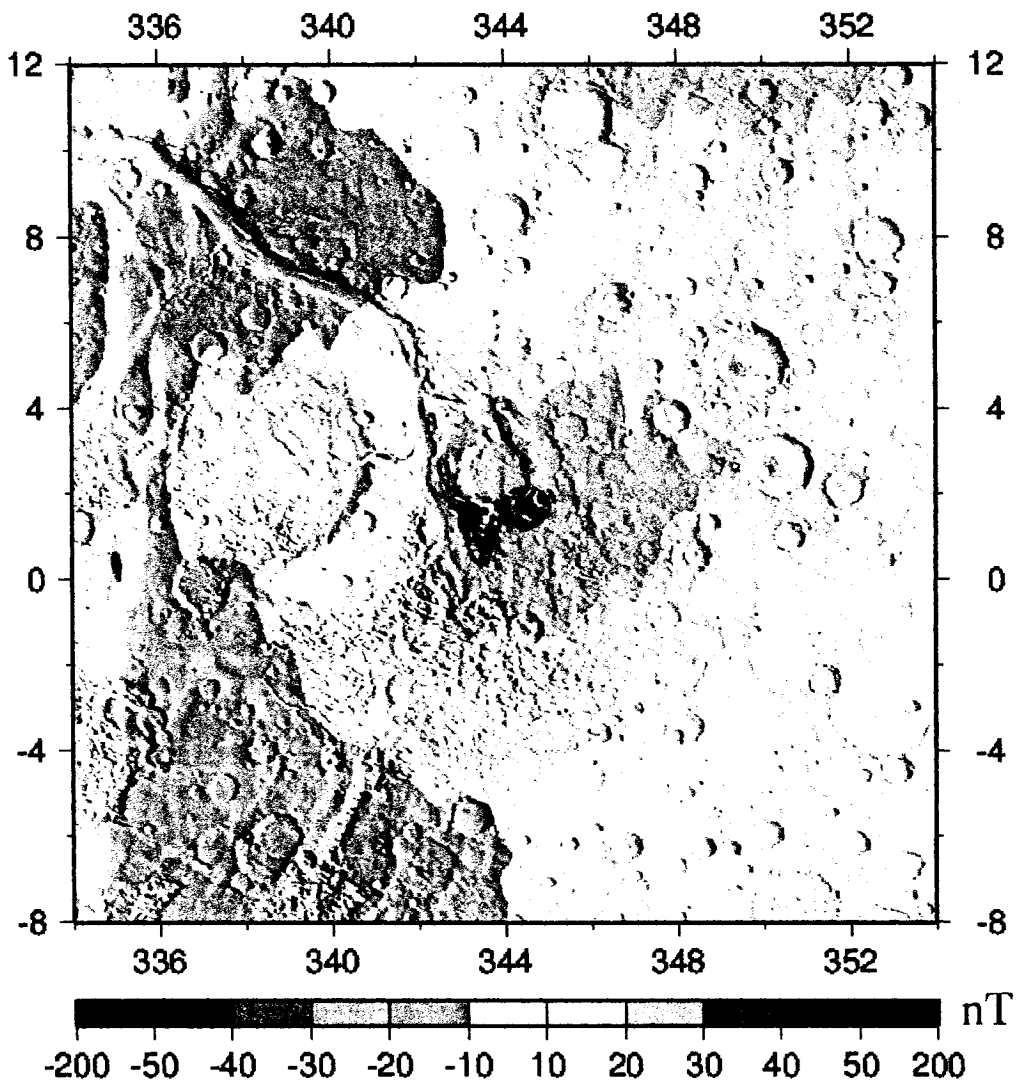

A7 radial component

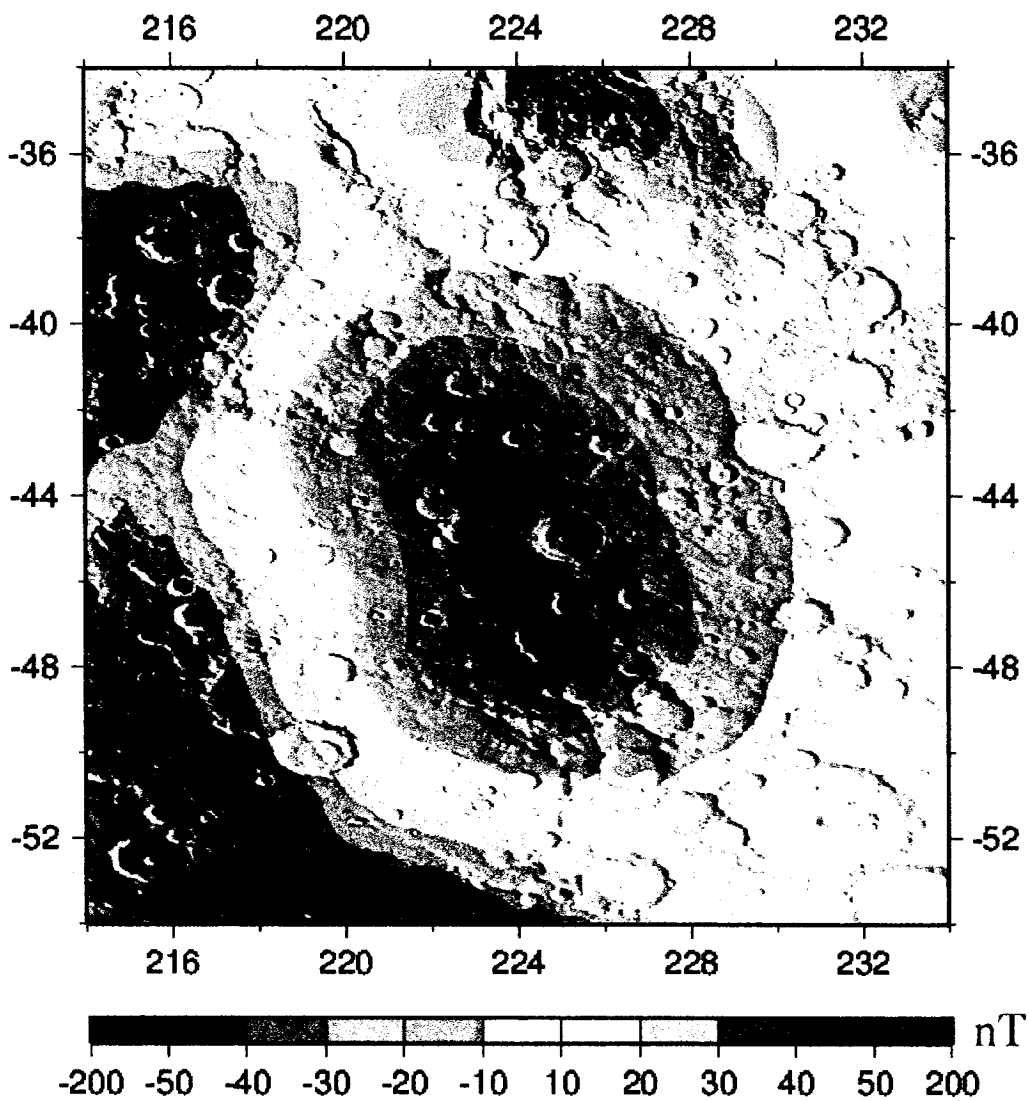

A8 radial component

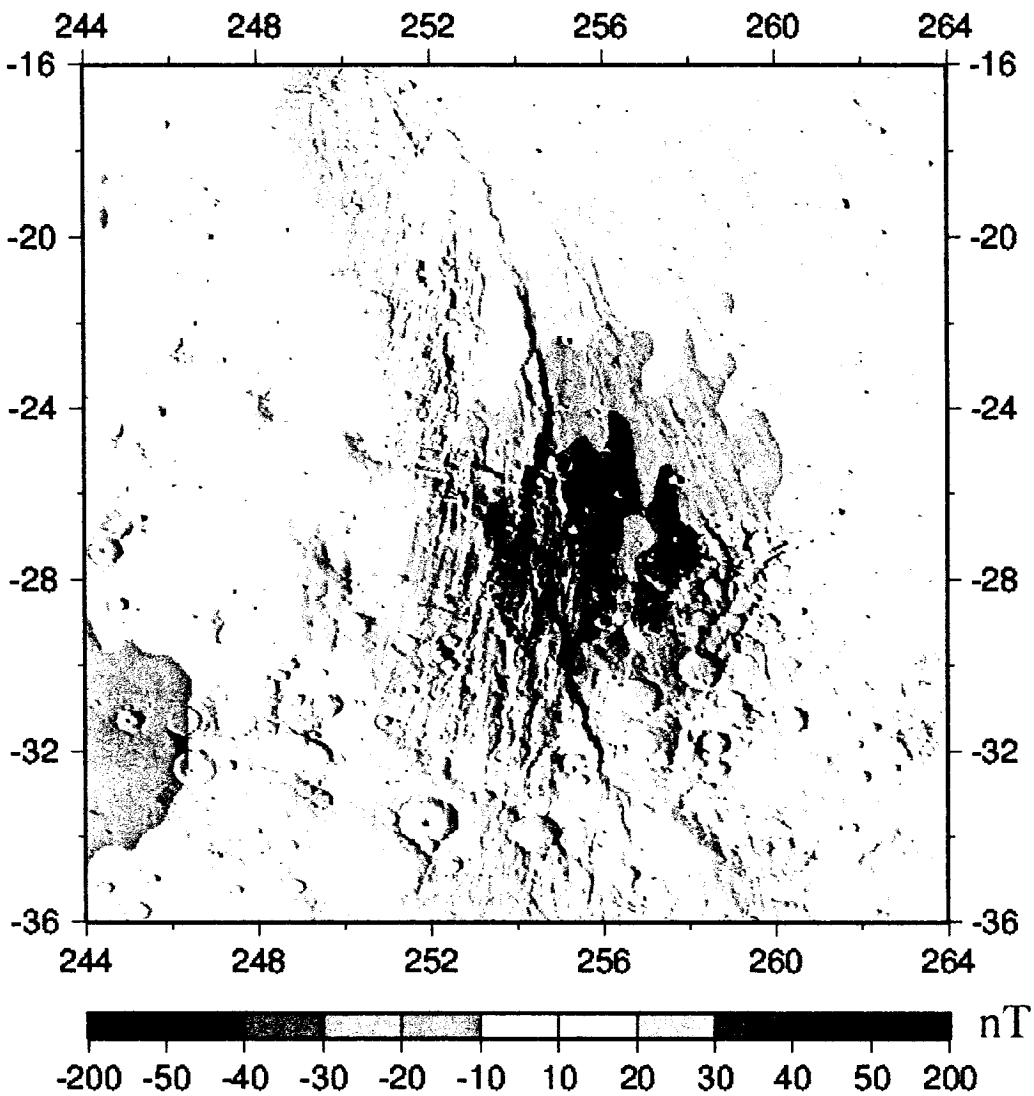

A9 radial component

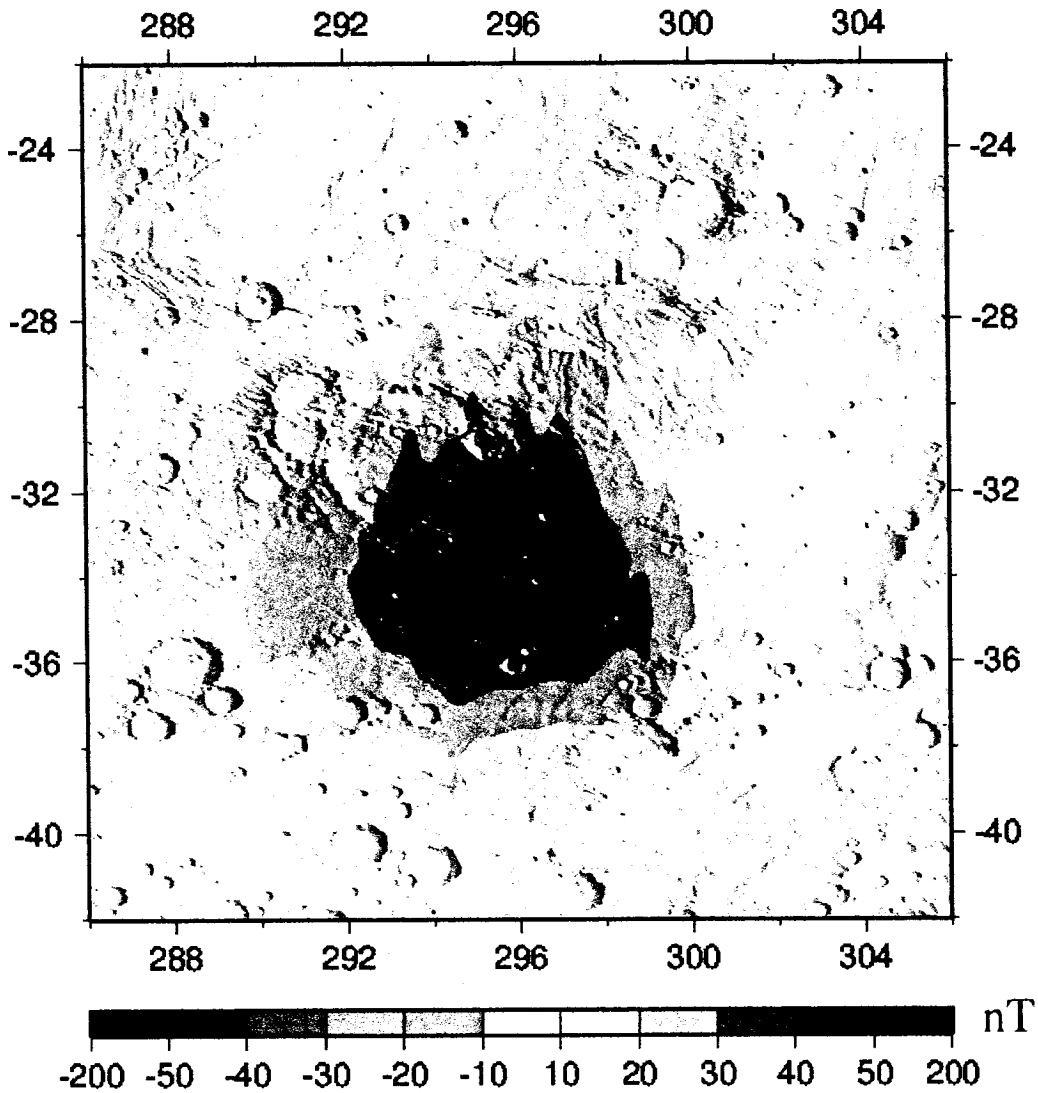

Appendix E: Magnetic field calculation

E.1 Introduction

One of the key elements of this thesis is the calculation of the magnetic field produced by an elliptical prism of constant magnetization. This magnetic field is calculated for elliptical prisms of different configurations and then compared with the observed data. The Fortran routine used in this thesis to calculate the magnetic field of an elliptical prism was originally designed and written by my supervisor. One very important part of my work was to test this routine and make sure that the calculated model field is correct.

To check this routine one can, of course, look directly at the code. However, for such complex routine, this is not sufficient. It is always possible, even after one has made many revisions, to find out that the code outputs incorrect results. In this work I have adopted a different way of looking at this problem. First, as stated in section 4.4, I have developed my own magnetic field calculation routine based on the Talwani numerical method. This method works in a very different way than the one used in the modeling program. For a given set of input parameters the two routines must, of course, yield very similar results. In the end the choice of one method over the other is only a matter of preference and computer performance. In this case the method provided by my supervisor perform the calculation much faster than the Talwani method and consequently this is the one I used in the modeling program.

Although this testing method is robust, I went one step further, by calculating analytical expressions for simple prism configurations and comparing the result with the output of both numerical routines. This appendix explains in more details the inner working of both numerical methods used during this work. The next section also provides an example of analytical field calculations. This result will be used later to compare with the outputs obtained from both numerical methods.

E.2 Example of magnetic field calculation

In this section I derive an analytical expression for the magnetic field produced by circular prism of constant magnetization. The situation is illustrated in figure E.1. The prism is basically a cylinder of radius R and height h. It is located at the origin of a suitable reference frame. We seek to determine the magnetic field at a point P situated on the cylinder axis at a distance D from the top of the prism. In this situation the magnetization vector is aligned in the z axis direction, so that the magnetization can be written as

$$\vec{m} = m\hat{k} \qquad \textbf{E.1}$$

The magnetic potential produced by a volume distribution of magnetization is given by

$$V(\vec{r}) = -\frac{1}{u}\iiint_{Volume} \hat{m} \bullet \nabla\left(\frac{m}{|\vec{r} - \vec{r}'|}\right) dV' \qquad \textbf{E.2}$$

Where $\vec{r}$ is the position vector of the point where we want to calculate the magnetic field. $\vec{r}'$ is the position vector of an infinitesimal volume element inside the prism. The gradient operator operates in the $\vec{r}$ domain while the integration is carried in the $\vec{r}'$ domain. The expression $|\vec{r} - \vec{r}'|$ is simply the distance between the two points. Finally the magnetization unit vector $\hat{m}$ is $\hat{k}$ in this situation. The constant u is the free space permeability and is given by

$$u = \frac{4\pi}{u_o} = 1 \times 10^{7} \qquad \textbf{E.3}$$

The magnetic field at point P is then calculated by taking the negative of the gradient of the potential field, that is

$$\vec{B} = -\nabla V \qquad \textbf{E.4}$$

Because of the symmetry of the prism it is more convenient to work in cylindrical coordinates to solve the integral in equation E.2. In cylindrical coordinates the gradient operator is written as

$$\nabla = \frac{\partial}{\partial r}\hat{r} + \frac{1}{r}\frac{\partial}{\partial \theta}\hat{\theta} + \frac{\partial}{\partial z}\hat{k} \qquad \textbf{E.5}$$

Since the magnetization is along the z axis then the scalar product inside equation E.2 simply becomes

$$\hat{m} \bullet \nabla\left(\frac{m}{|\vec{r} - \vec{r}'|}\right) = \frac{\partial}{\partial z}\left(\frac{m}{|\vec{r} - \vec{r}'|}\right) \qquad \textbf{E.6}$$

So that the integral in equation E.2 becomes

$$V(\vec{r}) = -\frac{1}{u}\iiint_{Volume} \frac{\partial}{\partial z}\left(\frac{m}{|\vec{r} - \vec{r}'|}\right) r'\,dr'\,d\theta'\,dz' \qquad \textbf{E.7}$$

The solution of this integral is

$$V(z) = \frac{2\pi m}{u}\left[\left((z-h)^2 + R^2\right)^{1/2} + h - \left(z^2 + R^2\right)^{1/2}\right] \qquad \textbf{E.8}$$

And correspondingly

$$B_z = \frac{2\pi m}{u}\left[\frac{z}{\left(z^2 + R^2\right)^{1/2}} - \frac{(z-h)}{\left((z-h)^2 + R^2\right)^{1/2}}\right] \qquad \textbf{E.9}$$

This formula will be used later in this appendix to compare with the outputs of both the Talwani numerical method and the magnetic field calculation routine that was actually used in the modeling program.

E.3 The Talwani numerical method

The Talwani method calculates the magnetic field produced by an arbitrary shaped body of constant magnetization. The advantage of this method is that two of the three integrals that need to be solved have analytical solutions. It is always more convenient and accurate to have analytical solutions. The method basically uses the same logic as explained in the preceding section. First we obtain the magnetic potential of an infinitesimal element of magnetization at the origin of the reference frame. It is given by

$$V = \frac{\vec{d} \bullet \vec{R}}{R^3} \qquad \textbf{E.10}$$

This potential element can be expressed in term of the magnetization, knowing that $\vec{d} = \vec{m}\,\Delta x \Delta y \Delta z$ where the vector $\vec{m}$ is the magnetization vector. We get

$$V = \frac{m_x x + m_y y + m_z z}{R^3} \Delta x \Delta y \Delta z \qquad \textbf{E.11}$$

One can than integrate all over the volume to get the total potential. As before the magnetic field is calculated by taking the negative of the gradient of the potential. Talwani then calculate the magnetic field at the origin of the reference frame as follow

$$\begin{aligned} B_x &= m_x I_1 + m_y I_2 + m_z I_3 \\ B_y &= m_x I_2 + m_y I_4 + m_z I_5 \\ B_z &= m_x I_3 + m_y I_5 + m_z I_6 \end{aligned} \qquad \textbf{E.12}$$

Where I_1.....I_6 are the following volume integrals.

$$I_1 = \iiint_{Volume} \frac{3x^2 - R^2}{R^5} dxdydz$$

$$I_2 = \iiint_{Volume} \frac{3xy}{R^5} dxdydz$$

$$I_3 = \iiint_{Volume} \frac{3xz}{R^5} dxdydz$$

$$I_4 = \iiint_{Volume} \frac{3y^2 - R^2}{R^5} dxdydz$$

$$I_5 = \iiint_{Volume} \frac{3yz}{R^5} dxdydz$$

$$I_6 = \iiint_{Volume} \frac{3z^2 - R^2}{R^5} dxdydz$$

E.13

The body is divided into a series of horizontal layers that are approximated by polygonal laminas. The surface part of the last integrals is evaluated and programmed as an analytical formula into the computer. The calculation of each volume integral is then completed by numerically integrating in the z direction.

E.4 Comparing methods

Table E.1 shows the z component of the magnetic field of a circular prism calculated at different altitudes between 300 and 400 km. The prism is 10 km thick and has a radius of 200 km. All 3 methods are used to calculate the field. The results obtained by the two numerical methods are identical to 3 decimal places and negligibly different from the value obtained by equation E.9. Many numerical experiments have shown the almost perfect correlation of the two numerical methods for more complex situations.

Table E.1

Results of calculation of the magnetic field of a circular prism by using an analytical formula, the Talwani method and the numerical routine actually used during the modeling process. Results of the numerical procedures are identical within 3 decimal places.

Altitude	Equation E.10	Talwani	Modeling pro.
(km)	(nT)	(nT)	(nT)
300.0	55.528	55.484	55.484
310.0	51.813	51.771	51.771
320.0	48.390	48.350	48.350
330.0	45.236	45.197	45.197
340.0	42.326	42.288	42.288
350.0	39.640	39.604	39.603
360.0	37.160	37.124	37.125
370.0	34.867	34.833	34.833
380.0	32.746	32.714	32.714
390.0	30.783	30.752	30.752
400.0	28.964	28.934	28.934

Table E.1

Figure E.1

Calculation of the z component of the magnetic field on the axis of a circular prism.

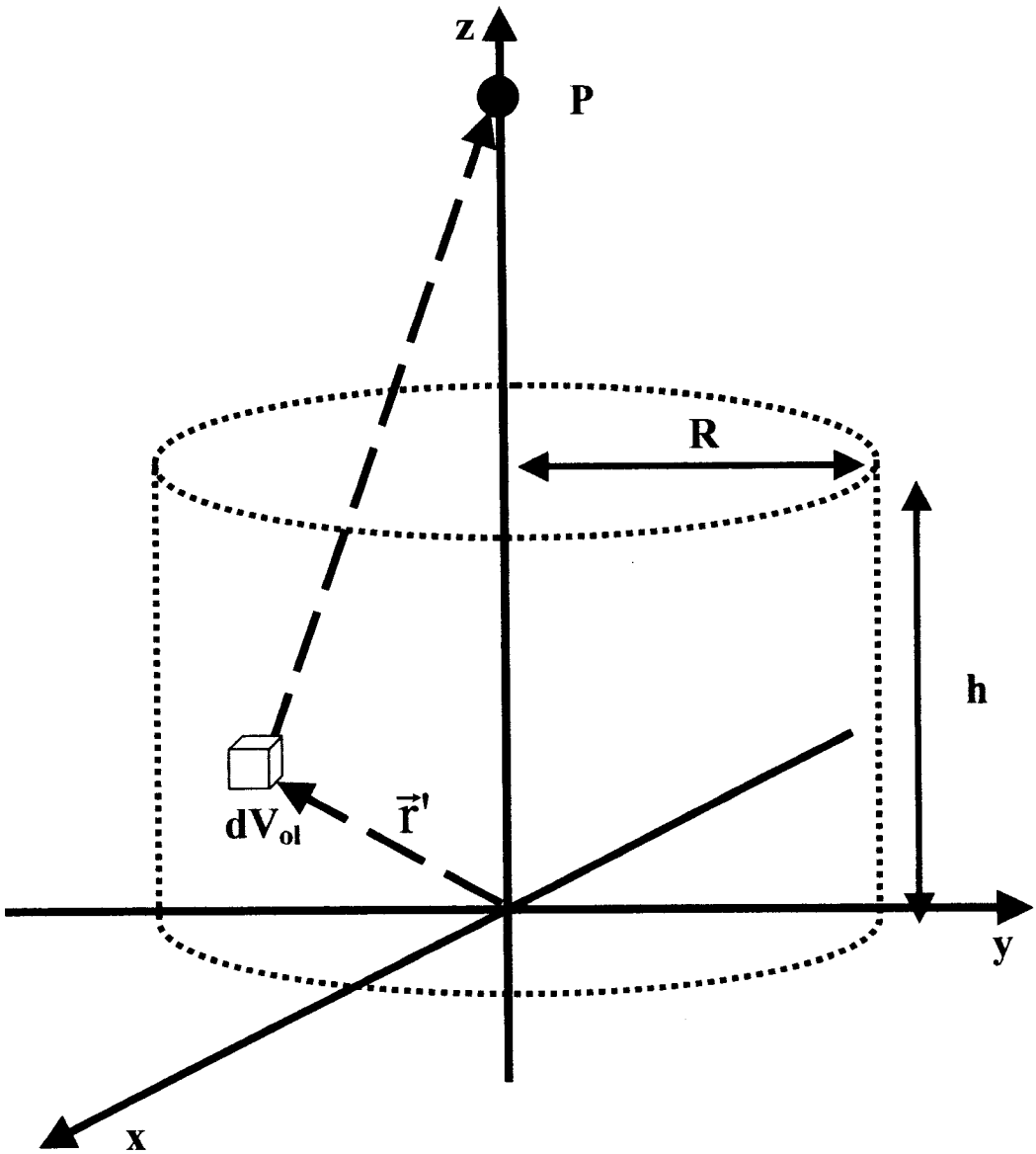

Figure E.1

References

Acuna et al., Magnetic field and plasma observations at Mars: Initial results of the Mars Global Surveyor mission, Science, 279, 1676-1680, 1998.

Arkani-Hamed J., Strength of Martian lithosphere beneath large volcanoes, Journal of Geophysical Research, 105, 26713-26732, 2000.

Arkani-Hamed J., A 50 degree spherical harmonic model of the magnetic field of Mars, Journal of Geophysical Research, 106, 23197-23208, 2001a.

Arkani-Hamed J., Paleomagnetic Pole Positions and Poles Reversals of Mars, Geophysical Research Letters, 28, 3409-3412, 2001b.

Arkani-Hamed J., Magnetization of the Martian crust, Journal of Geophysical Research, 107, doi:10.1029/2001JE001496, 2002.

Arkani-Hamed J. and Boutin D., Paleomagnetic poles of Mars: Revisited, Journal of Geophysical Research, 109, doi:10.1029/2003JE0029, 2004.

Butler R. F., Paleomagnetism; Magnetic Domains to Geologic Terranes, 319 pp., Blackwell Sci, Malden, Mass., 1992.

Cain J. C. et al., An n=90 internal potential function of the Martian crustal magnetic field,, Journal of Geophysical Research, 108, doi:10.1029/2000JE001487, 2003.

Connerney et al, Magnetic Lineations in the ancient crust of Mars, Science, 284, 794-798, 1999.

Defraigne P. et al. Mars rotation variations induced by atmosphere and ice caps, Journal of Geophysical Research, 105, 24563-24570, 2000.

Dunlop, D.J. and O. Ozdemir, Rock magnetism: Fundamentals and Frontiers, 573 pp., Cambridge Univ, Press, New York, 1997.

Dunlop D.J., Arkani-Hamed J., Mars Magnetic lithosphere: Candidate Minerals, Presentation at the 2004 Joint Assembly AGU conference in Montreal, Canada, 2004

Dyment J., Arkani-Hamed J., Equivalent source magnetic dipoles revisited, Geophysical Research Letter, 25 2003-2006, 1998.

Evans D., True polar wander and super continents, Tectonophysics, 362, 303-320, 2001.

Frey,H. et al. , A very large population of likely impact basins in the northern lowlands of Mars revealed by MOLA data, Lunar Planet. Sci. XXXII, abstract 1680, 2001.

Helbig, Klaus, Some integrals of magnetic anomalies and their relation to the parameters of the disturbing body: Zeitschrift fur Geophysik, 29, 83-96, 1963.

Hood L.L. and Zacharian A. Mapping and modeling of magnetic anomalies in the northern polar region of Mars. Journal of Geophysical Research, 106, 14601-14619, 2001.

Hood L.L., Young C. N., Modeling of major Martian magnetic anomalies: Further evidence for polar reorientation during the Noachian, Lunar and Planetary Science abstract #1108, 2004.

Hood, L.L., and N. Richmond, Mapping and modeling of major magnetic anomalies, LPSC XXXIII, Abstract 1128, LPI, Houston, 2002.

Hoolst T. V. et al, Chandler wobble and free core nutation of Mars, Planetary and Space Science, 48, 1145-1151, 2000.

Kirschvink J.L. et al. Evidence of a large-scale Early Cambrian reorganization of continental masses ny inertial interchange true polar wander, Science, 277, 541-544, 1997

Langlais B. et al, Crustal magnetic field of Mars, Journal of Geophysical Research, 108, doi:10.1029/2000JE002048, 2003.

Love A.E.H., A treatise on the mathematical theory of elasticity, Cambridge University Press, Fourth edition . ISBN 0-486-0174-9, 1927.

Mackenzie D. et al., The relationship between Martian gravity and topography, Earth and planetary Science letters, 195, 1-16, 2002.

Meert, J.G., Paleomagnetic analysis of Cambrian true polar wander, Earth and Planetary Science Letters, 168, 131-144, 1999.

Melosh H.J., Tectonic patterns on a reoriented planet: Mars, Icarus, 44, 745-751, 1980.

Mohit, P.S and J. Arkani-Hamed, Impact demagnetization of the Martian crust, Icarus, 168, 305-317, 2004

Mound J.E., Mitrovica J.X., Sea-level and true polar wander during the late Cretaceous, Geophysical Research Letter, 28, 2057 – 2060, 1998

Murray B.C. and Malin , M. C. Polar wandering on Mars, Science, 179, 997-1000, 1973

Nimmo F. and Gilmore M., Constraints on depth of magnetized crust on Mars from impact craters, Journal of Geophysical Research, 106, 12,315-13,323, 2001.

Parker R. L., Ideal bodies for Mars magnetics, Journal of Geophysical Research, 108, doi:10.1029/2001JE001760, 2003.

Phillips J. D. Martian magnetization vectors estimated from Helbig analysis support a reversing core dynamo, Poster presented at AGU meeting 2004.

Purucker,M. et al., An altitude normalized magnetic map of Mars and it's interpretation, Geophysical Research letters, 27, 2449 – 2452, 2000.

Ricard et al., Isostatic Deformations and Polar Wander Induced by Redistribution of Mass within the Earth, Journal of Geophysical Research, 97, 14223-14236, 1992.

Richmond N. C. and Hood L. L., Paleomagnetic pole positions of Mars. Abstract #1721 from the XXXIV Lunar and Planetary Science conference, 2003.

Schultz, P.H., and A.B. Lutz, Polar wandering of Mars, Icarus, 73, 91-141,1988.

Spada G. et al, True polar wander affects the Earth dynamic topography and favor a highly viscous mantle, Geophys. Res. Lett., 31, 137-140, 1994.

Spada G. et al. Long-term rotation and mantle dynamics of the Earth, Mars and Venus., Journal of Geophysical Research, 101, 2253-2266, 1996.

Spada G . et al., Spin and Inertia of Venus, Geophysical Research Letter, 23 (15), 1997-2000, 1996b

Spohn, T. et al. (2001) Geophysical constraints on the evolution of Mars, Space Sci. Rev., vol. 96, 231-262, 2001.

Sprenke K.F., Baker L.L., magnetization, Paleomagnetic Poles, and Polar Wander on Mars, Icarus, 147, 26-34.

SteifelHagen M., A Comparative Study Of Long-Term Polar Motion Of Terrestrial Bodies, Thesis report, TU Delft, 2002.

Talwani M., Computation with the help of digital computer of magnetic anomalies caused by bodies of arbitrary shape, Geophysics, 30, 797-817, 1965.

Vermeersen L.L.A., Sabadini R., Polar wander, sea-level variation and ice age cycles. Surv. Geophys., 20, 415, 440, 1999.

Whang, Y. C., Magnetospheric magnetic field of Mercury, Journal of Geophysical Research, 82, 1024, 1977.

Wieczorek M. A. and Zuber M. T., Thickness of the Martian crust : Improved constraints from geoid-to-topography ratios, Journal of Geophysical Research, 109, doi:1029/2003JE002153, 2004.

Willemann R. J. and Turcotte D. L., The role of lithospheric stress in the Support of the Tharsis Rise, Journal of Geophysical Research, 87, 9793-9801, 1982.

Willeman R.J., Reorientation of Planets with Elastic lithospheres, Icarus, 60, 701 – 709, 1984.

Zuber et al., Internal structure and early Thermal evolution of Mars from Mars Global Surveyor Topography and Gravity, Science, 287, 1788-1793, 2000.